Astronomy Reports, Vol. 45, No. 2, 2001, pp. 100–112. Translated from Astronomicheskiĭ Zhurnal, Vol. 78, No. 2, 2001, pp. 122–136.

Revised Magnesium Abundances in Galactic Halo and Disk Stars

N. N. Shimanskaya and L. I. Mashonkina

Kazan State University, ul. Lenina 18, Kazan, 420008 Tatarstan, Russia

Received March 6, 2000

Abstract—A differential analysis of the magnesium abundances in 61 F–K dwarfs and subgiants with metallicities –2.6 < [Fe/H] < +0.2 is performed based on published observational data. Fundamental parameters for 36 stars are determined: $T_{\rm eff}$ from *V–K* and *V–R*; $\log g$ from HIPPARCOS parallaxes, and [Fe/H] and ξ_t from Fe II lines. The computations allow for non-LTE effects in the formation of the Mg I lines. For most of the stars, the standard errors in the Mg abundances do not exceed 0.07 dex. The metallicity dependence of [Mg/Fe] is analyzed. Magnesium shows a constant overabundance relative to Fe of 0.46 ± 0.06 dex for metallicities –2.6 < [Fe/H] < –0.7 Mg. The Mg overabundance decreases abruptly to ~ +0.27 dex at [Fe/H] ≃ –0.7. At higher metallicities, the Mg abundance smoothly decreases to the solar value at [Fe/H] = 0.0. Halo stars with metallicities [Fe/H] < –1.0 exhibit lower Mg overabundances ($\overline{[{\rm Mg/Fe}]}$ = +0.22 dex) compared to the [Mg/Fe] values for other stars with similar [Fe/H]. © *2001 MAIK "Nauka/Interperiodica".*

1. INTRODUCTION

The chemical evolution of the Galaxy is one of the most interesting problems in modern astrophysics. Questions demanding study include mechanisms for the enrichment of heavy elements in the interstellar medium during various epochs of the Galaxy's lifetime, trends in the formation of the Galactic structure (from halo to bulge, from outermost to innermost regions), choice of chemical elements to be used as chronometers to measure the age of the Galaxy, and the age–metallicity relation. Starting with Hoyle's work [1], the iron abundance in the interstellar medium has been assumed to increase monotonically with time, so that [Fe/H] can be viewed as a stellar age indicator. Therefore, studies of Galactic chemical evolution have traditionally been based on analysis of the dependence of [X/Fe] (the abundance of some element relative to Fe) on [Fe/H].

The current paper focuses on magnesium—an element synthesized in the α process. According to the standard theory of Galactic chemical evolution, the main sources of magnesium enrichment in the interstellar medium are single, massive or intermediate-mass stars that explode as type II supernovae (Mg is synthesized in the burning of C and Ne), and single, intermediate-mass stars with mass outflows at the stage of hydrostatic C and Ne burning.

The role of these sources of enrichment in various epochs of the Galaxy's lifetime can be elucidated by analyzing the Mg abundances in stars of different ages. Extensive data have been published on the LTE magnesium abundances in dwarfs of the Galactic halo and disk. Analysis of the results of these studies leads to the identification of two groups of stars with different characteristic [Mg/Fe] values. The first consists of stars with metallicities –0.8 < [Fe/H] < +0.3; on average, their Mg abundances increase with [Fe/H]. The second group includes very metal-poor stars (–3.0 < [Fe/H] < –0.8), in which magnesium is overabundant by 0.2– ~0.5 dex relative to iron. We now give a brief review of some studies including large numbers of stars of these two groups.

The lowest [Mg/Fe] values (0.20–0.27 dex) for metal-poor stars ([Fe/H] < –0.8) have been measured by Steenbook [2] and Nissen and Shuster [3]. Francois [4] found a constant Mg overabundance of 0.35 dex. Similar [Mg/Fe] values were obtained by Laird [5], Gratton and Sneden [6], Edvardsson *et al.* [7], and Chen *et al.* [8] for a small group of dwarfs with [Fe/H] <–0.8. Constant Mg overabundances of about 0.4–0.5 dex were found by Magain [9], Nissen *et al.* [10], and Fuhrmann [11]. In all these analyses of the chemical compositions of metal-poor dwarfs and subgiants, the abundance accuracies are better than 0.1 dex. The only exceptions are the data of Laird *et al.* [5] and Edvardsson *et al.* [6], which have rms errors of δ = ±0.18 and 0.12 dex, respectively. As a rule, the scatter of [Mg/Fe] among stars of similar [Fe/H] does not exceed 0.25 dex. However, the corresponding scatter for the abundances of Laird *et al.* [5] and Edvardsson *et al.* [7] reaches 0.4 dex, preventing unambiguous interpretation of the observed [Mg/Fe]–[Fe/H] relation.

The [Mg/Fe]–[Fe/H] relation changes abruptly in the range from –1.0 to –0.4 dex. For example, Fuhrmann [11] points out a ~0.2-dex *steplike* change in the Mg abundance in the transition from the thick to the thin disk in the region of overlapping metallicities, and a decrease of the Mg overabundance to the solar value [Fe/H] = 0.0 with further decrease in the metallicity.

1063-7729/01/4502-0100$21.00

Francois [4], Lair [5], and Gratton and Sneden [6] indicate a *smooth* decrease of [Mg/Fe] at metallicities [Fe/H] > –1. The results of Chen *et al.* [8] also show a smooth decrease in the Mg overabundance at [Fe/H] > –0.7. In spite of the enormous number of stars studied by Edvardsson *et al.* [7], the considerable scatter of their abundances makes it impossible to unambiguously determine whether the Mg overabundance changes smoothly or abruptly at metallicities from –1 to 0.

As a rule, comparisons of theoretical models of Galactic chemical evolution with observations employ compilations of abundance determinations made during different studies of [Fe/H] for various samples of stars. The observed [X/Fe]–[Fe/H] dependences should cover the widest possible metallicity interval. Very metal-poor stars ([Fe/H] < –1) are usually members of the Galactic halo, and are located at considerable heliocentric distances. These stars are faint, and observed samples are biased in favor of high-luminosity objects. Unlike dwarfs, the primordial chemical compositions of these stars could change during their evolution, and studies using compiled data usually do not distinguish between results for dwarfs and giants. Furthermore, different chemical-composition analyses have often used different methods to determine the parameters of stellar atmospheres. All these factors can increase the scatter of [X/Fe] for a given metallicity, which, in turn, introduces uncertainties in the interpretation of the observed [X/Fe]–[Fe/H] relations. Note also that elemental abundances are determined relative to some adopted solar chemical composition, and different authors often use different solar abundances for the same element—a fact that must be taken into account if one wishes to correctly use heterogeneous samples of [X/Fe] values.

The work of Timmes *et al.* [12] is an example of such a compilation of results obtained for magnesium and used to draw certain evolutionary conclusions. In their Fig. 15, Timmes *et al.* [12] in the metallicity range –3 < [Fe/H] < +0.3 combine the results of Magain [9] and Edvardsson *et al.* [7] for halo and disk dwarfs with those of Gratton and Sneden [13] for halo giants. Whereas the Mg overabundance in metal-poor dwarfs ([Fe/H] < –1.3) is approximately constant according to Magain's [9] data, the Mg overabundance in giants with the same metallicities exhibits a small increasing trend with decreasing [Fe/H]. As noted above, the data of Edvardsson *et al.* [7] indicate a Mg overabundance increase in stars with [Fe/H] > –1. The resulting observational sequence has a [Mg/Fe] scatter of 0.2–0.4 dex, or even higher. Figure 15 in [12] shows theoretical [Mg/Fe]–[Fe/H] curves computed based on chemical evolution models. It is evident from this figure that current theories fail to adequately describe the observations. The plateau in the relation computed by Timmes *et al.* [12] is limited to metallicities –2 < [Fe/H] < –1, while the Mg overabundance smoothly decreases when [Fe/H] > –1. Furthermore, the theoretical computations underestimate the observed overabundances.

Another example of theoretical models for magnesium are those computed by Matteucci and Francois [14]. These show the Mg abundance to increase monotonically with decreasing [Fe/H], and imply a [Mg/Fe]–[Fe/H] relation that varies smoothly at metallicities [Fe/H] = –1 and –2. Thus, the theory of chemical evolution has not been able to fully explain the published observational relations and the metallicity dependence of the Mg abundance.

The aim of our own study is to redetermine the Mg abundances in F–K dwarfs and subgiants based on published data. Our analysis differs from those of previous studies in that we allow for departures from LTE in the formation of Mg I lines and refine the atmospheric parameters of the stars considered. Section 2 describes the observational data used. In Section 3, we determine the atmospheric parameters of the stars studied. In Section 4, we determine non-LTE Mg abundances in 61 stars covering a wide range of metallicities, and compare our [Mg/Fe]–[Fe/H] relation for Galactic halo and disk stars with those derived by other authors. Our conclusions are formulated in the last section.

2. OBSERVATIONAL MATERIAL

We adopted observational data of approximately uniform quality from [3, 7, 13, 15–18], based mainly on CCD observations, with the exception of three studies based on Reticon [16], (partially) Digicon [7], and photographic [17] observations. The derived Mg abundances for dwarfs and subgiants of the Galactic disk and halo were based on visible and infrared Mg I lines: λλ4167, 4571, 4702, 5528, 5711, 8213, 8712, and 8717 Å. The parameters of these lines are summarized in Table 1.

We used the following observational data.

(1) For 20 halo stars, equivalent widths of the Mg I λλ4167, 4571, 4702, 5528, and 5711 Å lines published by Zhao and Magain [15], based on observations with spectral resolution $\lambda/\Delta\lambda \simeq 20000$ and signal-to-noise ratio $S/N \simeq 100$.

(2) For 13 halo and disk stars, we used data for the Mg I λ5711 Å line of Nissen and Shuster [3] (spectral resolution $\lambda/\Delta\lambda \simeq 60000$ and $S/N \simeq 140$–180).

(3) We selected seven Galactic halo and disk stars from the large list of Gratton and Sneden [13, 16]. For these stars, data for the Mg I λλ5528, 5711, 8213, and 8717 Å lines with spectral resolution $\lambda/\Delta\lambda \simeq 20000$ and 80000 and $S/N > 100$ are available.

(4) We adopted the equivalent widths of Mg I λλ8712 and 8717 Å lines for 30 disk stars from Edvardsson *et al.* [7]. Six stars were observed with spectral resolution $\lambda/\Delta\lambda \simeq 60000$–80000 and $S/N \simeq 200$, and the remaining stars with $\lambda/\Delta\lambda \simeq 36000$ and $S/N = 200$–500.

(5) The equivalent widths of the Mg I λλ4571 and 4703 Å lines for two stars published by Carney and Peterson [17] were based on observations with spectral resolution $\lambda/\Delta\lambda \simeq 17000$.

Table 1. Atomic parameters of Mg I lines

λ, Å	E_i, eV	$\log g_i f_{ij}$	γ_R, 10^8	$\log C_6$ (Unsold)	$\Delta\log C_6$	$\Delta\log\varepsilon^{\odot}_{\mathrm{Mg}}$, [non-LTE], dex
4571.085	0.00	−7.645	1.47×10^{-4}	−32.42	1.72	0.00
4571.089		−7.043				
4571.091		−6.737				
4571.093		−6.737				
4571.096		−6.177				
4571.099		−6.039				
4167.271	4.34	−0.71	4.553	−30.27	0.76	0.02
4702.991	4.34	−0.52	4.632	−30.26	0.74	0.01
5172.684	2.71	−0.381	5.271	−31.41	0.74	0.00
5183.604	2.72	−0.158			0.72	0.00
5711.088	4.34	−1.72	4.547	−30.66	0.77	−0.01
5528.405	4.34	−0.49	4.726	−30.75	0.44	0.01
6318.716	5.11	−1.97	1.334	−30.08	1.39	0.03
8213.034	5.75	−0.51	0.422	−29.80	1.25	−0.04
8712.676	5.93	−1.67	0.223	−29.53		
8712.689		−1.26			1.03	−0.03
8717.803	5.93	−2.85	0.223	−29.53		
8717.816		−1.85				
8717.825		−0.97			1.11	−0.03

The corrections $\Delta\log C_6$ to the van der Waals broadening constant and $\Delta\log\varepsilon^{\odot}_{\mathrm{Mg}}$ to the standard Mg abundance $\log\varepsilon^{\odot}_{\mathrm{Mg}} = 7.58$ dex for individual lines derived using a non-LTE approach were computed for the newKur model solar atmosphere.

(6) For Procyon, we used the Mg I λλ4571, 4702, 5172, 5183, and 6318 Å lines. We determined the equivalent widths of these lines using the Procyon atlas [18], which has a spectral resolution of $\lambda/\Delta\lambda = 150000$.

We determined the atmospheric Mg abundances of the stars studied using Mg I lines with equivalent widths greater than 7 mÅ. As a result, we determined non-LTE Mg I abundances in 61 dwarfs and subgiants. The list of stars considered is given in Table 2.

To identify possible systematic discrepancies between the observations of different authors and estimate random errors, we compared the equivalent widths of lines of various elements for stars in common to different studies (Fig. 1). We found no systematic differences between the data of Nissen and Shuster [3], Edvardsson *et al.* [7], and Zhao and Magain [15], and the corresponding scatter in the equivalent widths does not exceed 3.5 mÅ. The equations relating these data have the form

$$W_\lambda([7]) = (0.99\pm0.01)W_\lambda([3]) + (0.7\pm0.3)$$

for four stars and

$$W_\lambda([15]) = (1.03\pm0.02)W_\lambda([3]) + (0.0\pm0.9)$$

for two stars.

The lists of Gratton and Sneden [16] and Nissen and Shuster [3] have only one star in common: HD 76932. A comparison showed that the equivalent widths of [16] were systematically larger than those of [3] (see Fig. 1). The dispersion is 4 mÅ and the relation between the two sets of values for HD 76932 has the form

$$W_\lambda([16]) = (1.04\pm0.05)W_\lambda([3]) + (2.6\pm1.8).$$

As a result, abundances derived from the observations of [16] would be somewhat underestimated compared to those based on the data of [3] and of other studies. It follows from the results reported in Section 4 that these discrepancies do not exceed 0.08 dex, which is within the abundance errors.

3. PARAMETERS OF THE MODEL ATMOSPHERES

The accuracy of the elemental abundances depends not only on the observational errors and the adopted theory for the formation of the lines in the stellar atmospheres, but also on the accuracy of the fundamental stellar parameters. Therefore, when possible, we refined the atmospheric parameters of the stars as follows. We determined T_{eff} and/or $\log g$ and [Fe/H] for

36 stars. For the remaining stars, we adopted the atmospheric parameters from [11], since we could not determine parameters such as [Fe/H] and ξ_t using the methods described below.

3.1. Effective Temperatures

We determined the effective temperatures of 14 stars using the $(V–K)$–$T_{\rm eff}$ calibrations of Alonso *et al.* [19], which are based on $T_{\rm eff}$ values derived using the infrared-flux method [20]. We used $V–K$ because it is very sensitive to temperature and depends only slightly on surface gravity and blending. We adopted the V and K magnitudes from [21, 22] and reduced the K magnitudes to the system of Johnson [23] as described in [21]. We determined $T_{\rm eff}$ for CD –29° 2277 using the $(R–I)$–$T_{\rm eff}$ and $(V–R)$–$T_{\rm eff}$ calibration relations of [19]. The $R–I$ and $V–R$ color indices are given in [17].

We adopted the effective temperatures $T_{\rm eff}$ of 15 stars from Bikmaev [24], who computed them based on $V–K$ and $V–R$, and the infrared-flux temperatures $T_{\rm eff}$ of five stars from Alonso *et al.* [20]. For the remaining stars, we adopted the effective temperatures of Fuhrmann [11], based on Balmer-line profiles.

To reveal possible discrepancies between the $T_{\rm eff}$ values obtained using different color indices or different techniques, we performed the following comparisons. For 58 stars from [21, 22] we compared the temperatures derived using the infrared-flux method T_{IRFM} [20] with those derived using $V–K$, $V–R$, and $R–I$ (T_{VK}, T_{VR}, and T_{RI}). Figure 2 compares T_{IRFM} with T_{VR} and T_{RI}. $|T_{IRFM}–T_{VR}| < 100$ K for 88% of the stars, whereas $|T_{IRFM}–T_{RI}| < 100$ K for only 59% of the stars, with T_{RI} usually lower than the infrared-flux temperatures of Alonso *et al.* [20]. T_{IRFM} and T_{VK} differ insignificantly (by less than 50 K) for most of the stars (86%) used for the temperature comparison. $V–K$ is clearly a better temperature indicator than other color indices. However, we can easily see that temperatures derived from $V–R$ are closer to T_{IRFM} and T_{VK} than those derived from $R–I$. This leads us to conclude that the errors of our photometric effective temperatures T_{VK} and T_{VR} for 15 stars do not exceed 100 K.

For the 22 stars in common to our sample and the sample of Fuhrmann [11], we compared the temperatures derived from Balmer-line profiles [11] and from $V–K$ and $V–R$ (Fig. 3). It is evident from the figure that the spectroscopic temperatures are higher than the photometric estimates at low $T_{\rm eff}$. However, the difference does not exceed 100 K for 20 stars out of the 22, which is within the temperature errors.

It follows that our use of temperatures obtained using different color indices ($V–K$ and $V–R$) or different methods (photometric and spectroscopic) should not appreciably bias the resulting Mg abundances.

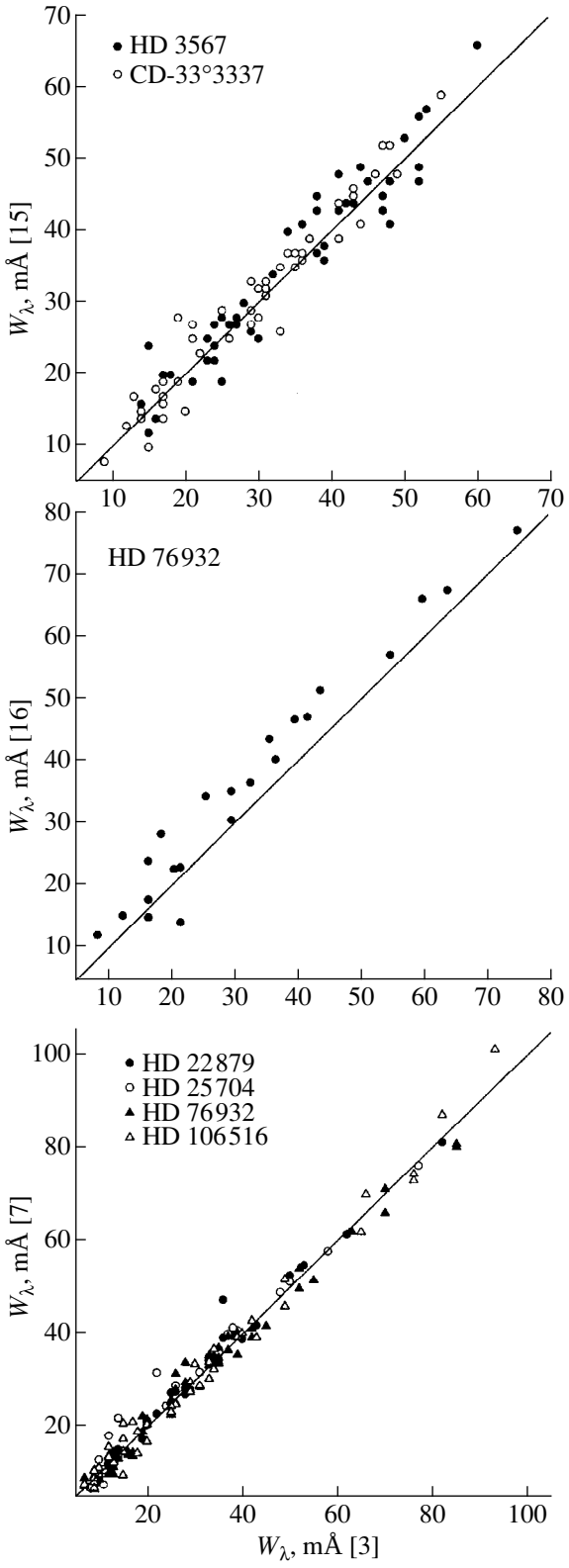

Fig. 1. Comparison of line equivalent widths for various elements for stars common to different studies.

Table 2. Atmospheric parameters, non-LTE Mg abundances from individual lines, and the mean Mg abundance

HD/BD	$T_{\rm eff}$, K	log g	[Fe/H]	ξ_t, km/s	[Mg/Fe], dex					$\overline{[{\rm Mg/Fe}]}$, dex	$\sigma_{(n)}$
Observations by Zhao and Magain [15]											
					4167 Å	4571 Å	4702 Å	5528 Å	5711 Å		
3567	6025	4.15	–1.19	1.5	0.34	0.32	0.22	0.33	0.19	0.28	0.06
16031	6110	4.28	–1.67	1.5	0.44	0.45	0.42	–	0.28	0.40	0.07
19445	5980	4.42	–1.95	1.3	–	0.56	0.39	0.52	0.39	0.46	0.07
34328	5830[B]	4.47	–1.70	1.5	0.42	0.56	–	0.39	0.44	0.45	0.06
59392	5980[B]	4.00	–1.58	1.3	0.42	0.39	–	0.44	–	0.42	0.02
74000	6220	4.12	–2.04	1.4	0.55	0.48	–	0.57	0.56	0.54	0.03
84937	6320	4.08	–2.14	1.5	0.49	–	–	0.57	–	0.53	0.04
116064	5790[B]	4.29	–2.02	1.5	0.44	0.34	–	–	0.50	0.43	0.07
122196	5830[B]	3.88	–1.85	2.1	0.25	0.10	–	0.25	0.25	0.21	0.06
140283	5660	3.65	–2.30	1.5	0.28	–	–	0.26	–	0.27	0.01
160617	5960[B]	3.82	–1.89	2.0	0.39	0.46	–	0.46	0.49	0.45	0.04
166913	6040[B]	4.17	–1.61	1.4	0.55	0.42	–	0.51	0.50	0.49	0.05
181743	5920[B]	4.39	–1.84	1.4	0.47	–	0.45	0.46	0.45	0.46	0.01
194598	5970	4.31	–1.21	1.4	0.39	0.49	0.38	0.36	0.39	0.40	0.04
213657	6090[B]	3.86	–2.00	2.1	0.58	–	–	0.52	0.48	0.53	0.04
–10°0388	5940[B]	3.62	–2.46	2.2	0.54	–	0.57	0.54	–	0.55	0.01
+02°3375	5860	4.24	–2.28	1.5	0.50	0.44	–	0.39	0.57	0.47	0.06
+03°0740	6160	4.20	–2.60	2.0	0.29	–	–	0.37	–	0.33	0.04
+17°4708	5960	4.10	–1.61	1.5	0.38	0.32	0.40	0.36	0.36	0.36	0.03
CD-33°3337	5920[B]	4.01	–1.35	1.4	0.44	0.48	0.35	0.46	0.31	0.41	0.06
Observations by Nissen and Schuster [3]											
										5711 Å	
3567	6025	4.13	–1.19	1.5						0.25	
17820	5850[B]	4.17	–0.72	1.0						0.47	
22879	5830[B]	4.32	–0.93	1.0						0.50	
25704	5710[B]	4.18	–1.00	1.2						0.40	
60319	5930[B]	4.23	–0.89	1.2						0.43	
76932	5855[A]	4.10	–1.00	1.3						0.55	
106038	5950	4.40	–1.35	1.3						0.48	
106516	6200	4.32	–0.78	1.5						0.55	
126681	5540[A]	4.53	–1.22	1.1						0.39	
241253	5853[A]	4.29	–1.18	1.3						0.48	
G046-031	5866[A]	3.94	–1.05	1.3						0.45	
G102-020	5254[A]	4.50	–1.19	0.9						0.26	
CD-33°3337	5920[B]	4.01	–1.35	1.4						0.45	
Observations by Gratton and Sneden [13, 16]											
					5528 Å	5711 Å	8213 Å	8717 Å			
6582	5390[F]	4.52	–0.83	0.90	–	0.42	–	0.36		0.39	0.03
19445	5980	4.42	–1.95	1.30	–	0.65	0.56	–		0.60	0.04
76932	5855[A]	4.10	–1.00	1.30	–	0.60	0.37	0.48			
					–	–	0.44	–		0.47	0.09
102870[F]	6085	4.04	+0.14	1.38	–	–0.05	–	–		–0.05	
103095	5110[F]	4.67	–1.36	0.90	–	–	–	0.44		0.44	
106516	6200	4.32	–0.78	1.50	–	–	–	0.48		0.48	
140283	5660	3.65	–2.30	1.50	0.19	–	–	–		0.19	

Table 2. (Contd.)

HD/BD	$T_{\rm eff}$, K	log$g$	[Fe/H]	ξ_t, km/s	[Mg/Fe], dex					$\overline{[Mg/Fe]}$, dex	$\sigma_{(n)}$
Observations by Edvardsson *et al.* [7]											
					8712 Å	8717 Å					
400[F]	6149	4.06	−0.25	1.31	0.05	0.18				0.11	0.06
6920[F]	5838	3.48	−0.05	1.35	–	0.13				0.13	
9826[F]	6107	4.01	+0.09	1.40	–	0.17				0.17	
16895[F]	6248	4.20	−0.01	1.42	0.05	0.05				0.05	0.00
22879	5830[B]	4.32	−0.93	1.00	0.54	0.50				0.52	0.02
25704	5710[B]	4.18	−1.00	1.20	0.51	0.40				0.45	0.05
61421[F]	6470	4.01	−0.01	1.91	−0.06	0.07					
					–	0.10				0.04	0.07
76932	5855[A]	4.10	−1.00	1.30	0.46	0.51					
					0.53	0.54				0.51	0.03
95128[F]	5892	4.27	0.00	1.01	0.02	0.04				0.03	0.01
102870[F]	6085	4.04	+0.14	1.38	−0.07	0.02					
					−0.02	0.04				−0.01	0.04
106516	6200	4.32	−0.78	1.50	–	0.44					
					–	0.52				0.48	0.04
109358[F]	5863	4.36	−0.21	1.12	0.06	0.06				0.06	0.00
114762[F]	5934	4.11	−0.71	1.14	0.28	0.26				0.27	0.01
137052[F]	6283	3.94	−0.03	1.89	–	0.03				0.03	
141004[F]	5864	4.09	−0.03	1.05	0.07	0.13				0.10	0.03
142860[F]	6254	4.02	−0.19	1.36	–	0.17				0.17	
143761[F]	5821	4.12	−0.24	1.10	0.13	0.21				0.17	0.04
153597[F]	6275	4.36	−0.11	1.48	–	0.06				0.06	
157214[F]	5735	4.24	−0.34	1.00	0.26	0.26				0.26	0.00
163989[F]	6116	3.62	−0.14	1.61	0.10	0.16				0.13	0.03
165908[F]	5994	4.01	−0.61	1.25	0.15	0.23				0.19	0.04
168151[F]	6357	4.02	−0.33	1.68	–	0.12				0.12	
184499[F]	5828	4.13	−0.51	1.17	0.28	0.30				0.29	0.01
187691[F]	6088	4.07	+0.07	1.35	–	0.12				0.12	
201891	5900[B]	4.30	−1.05	1.20	0.28	0.42				0.35	0.07
207978[F]	6313	3.94	−0.52	1.57	0.11	0.16				0.13	0.02
210855[F]	6176	3.81	+0.21	1.61	–	0.10				0.10	
217014[F]	5793	4.33	+0.20	0.95	−0.07	0.04				−0.01	0.05
218470[F]	6407	4.07	−0.12	1.85	–	0.13				0.13	
222368[F]	6157	3.95	−0.19	1.51	0.16	0.19				0.17	0.01
Observations by Carney and Peterson [17]											
					4571 Å	4703 Å					
134439	5010	4.66	−1.57	1.4	−0.02	0.00	–	–	–	−0.01	0.01
CD-29°2277	5620	4.65	−1.73	1.4	0.22	0.08	–	–	–	0.15	0.07
This paper (observations by R. Griffin and E. Griffin [18])											
					4571 Å	4703 Å	5172 Å	5183 Å	6318 Å		
61421[F] (Procyon)	6470	4.01	−0.01	1.91	0.11	–	0.05	0.06	0.08	0.07	0.02

The superscripts in the $T_{\rm eff}$ column indicate: "B"—data of Bikmaev [24]; "A"—data of Alonso *et al.* [20]. An "F" superscript to the parameters were adopted from Fuhrmann [11]. $\sigma_{(n)}$ is the rms error in the Mg abundance; $\log\varepsilon^{\odot}_{\rm Mg} = 7.58$, and $\log\varepsilon^{\odot}_{\rm Fe} = 7.51$.

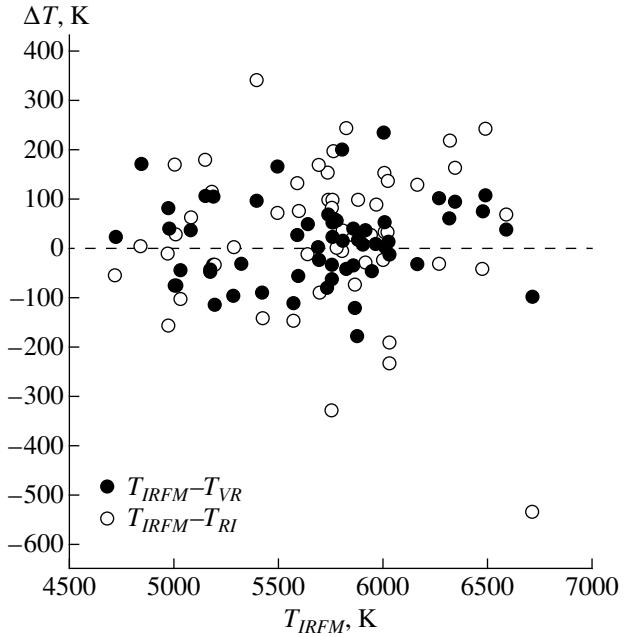

Fig. 2. Comparison of stellar temperatures T_{IRFM} based on the infrared-flux method [20] and T_{VR} and T_{RI} based on the *V–R* and *R–I* color indices.

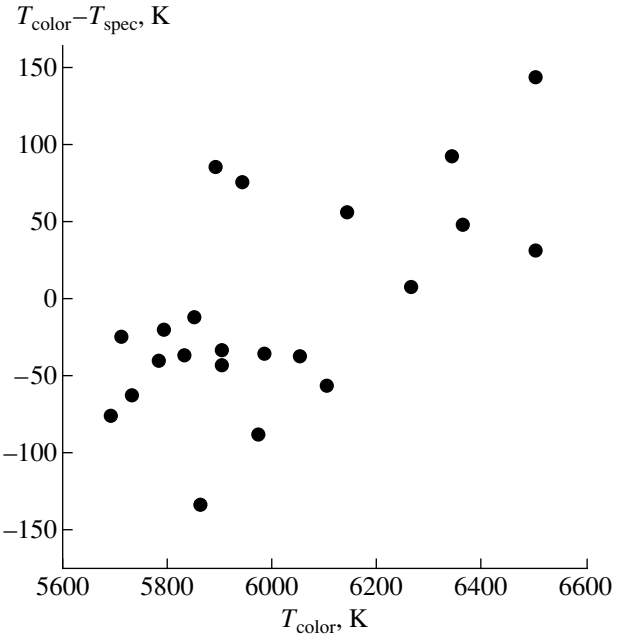

Fig. 3. A comparison of stellar temperatures based on the *V–K* and *V–R* color indices (T_{color}) on temperatures derived from Balmer-line profiles by Fuhrmann [11] (T_{spec}).

3.2. log g

For 36 stars, we determined $\log g$ from the relation

$$\log\frac{g}{g_\odot} = \log\frac{M}{M_\odot} + 4\log\frac{T_{\rm eff}}{T_{\rm eff\odot}} + 0.4V_0 + 0.4{\rm BC} + 2\log\pi + 0.12$$

using the parallaxes π from the HIPPARCOS catalog [25]. We adopted the bolometric corrections BC from [26]. The masses M of halo stars were obtained from theoretical evolutionary tracks [26]. According to [27], to obtain the best fit between the unevolved stars and the corresponding section of the 12–14 Gyr isochrones, the latter must be shifted by a constant amount $\Delta\log T_{\rm eff} = -0.022\ldots-0.012$. The assumed isochrone shift is $\Delta\log T_{\rm eff} = -0.017$. Figure 4 shows the isochrones and positions of our stars. It is clear that most of the stars are on or near the main sequence. The surface gravities $\log g$ are restricted to the rather narrow interval $3.5 < \log g < 4.7$. The error in $\log g$ is determined by the uncertainties in π, $T_{\rm eff}$, and M, and does not exceed 0.1 dex.

We adopted $\log g$ values for the remaining stars determined from the wings of the Mg Ib triplet [11] using an LTE approximation. Fuhrmann [11] estimates the accuracy of his method to be 0.1 dex. Fuhrmann's [11] comparison of $\log g$ values derived from line profiles with those determined from Eq. (1) yielded the small systematic difference $\Delta\log g \sim 0.03$ dex with an rms error of 0.05 dex. A similar comparison of our own $\log g$ values with those obtained by Fuhrmann [11] showed the discrepancy to be from 0.01 to 0.07 dex, which is within the errors in $\log g$.

Therefore, our use of $\log g$ values determined using different methods should not lead to appreciable systematic differences in the inferred Mg abundances.

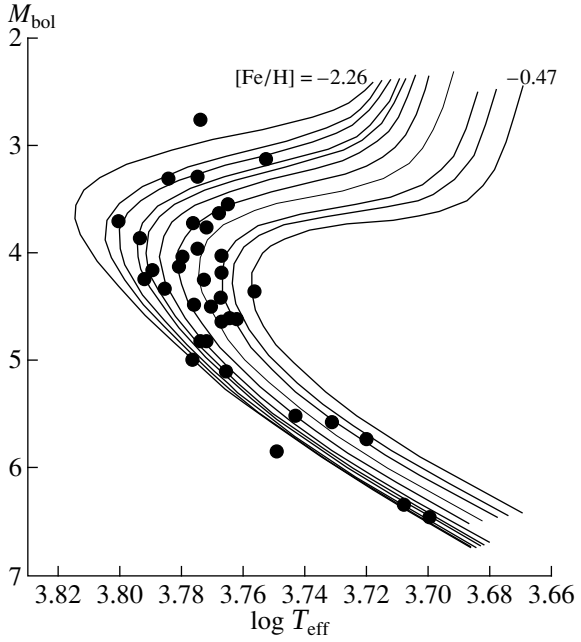

Fig. 4. Isochrones [26] corresponding to ages of 12–14 Gyr and the loci of the stars studied.

3.3. Iron Abundance and Microturbulence Velocity

The iron abundances ([Fe/H]) and microturbulence velocities ξ_t for 36 stars were determined from Fe II lines. The analysis of the statistical equilibrium of the Fe II ion of Thevenin and Idiart [28] showed departures from LTE for Fe II lines to be insignificant in the atmospheres of F–K dwarfs and subgiants. Therefore, we gave preference to ionized iron lines when determining iron abundances and microturbulence velocities. We first fitted the solar profiles of 21 Fe II lines in order to refine $f_{ij}\varepsilon_{\rm Fe}^{\odot}$ and the van der Waals broadening constants C_6. Fixing the iron abundance in the solar atmosphere ($\log\varepsilon_{\rm Fe}^{\odot} = 7.51$ on a logarithmic scale where the hydrogen abundance is $\log\varepsilon_{\rm H} = 12.0$ [29]), we determined f_{ij} for the Fe II lines used in our study. Table 3 gives the parameters of these lines, empirically refined oscillator strengths, and correction factors to $C_6(\Delta\log C_6)$. The computations were performed using a model solar atmosphere from Kurucz's [35] LTE grid (hereafter newKur); our choice of this model was based on the fact that we have used the models of [35] in various studies of individual stars. We adopted a microturbulence velocity for the solar atmosphere of 0.8 km/s, and estimate the accuracy of the ξ_t values for the stars studied to be 0.3 km/s.

For 13 Fe II lines, we compared our $\log g_i f_{ij}$ values with those published in [30–33]. The discrepancies for 11 lines range from 0.01 to 0.08 dex, and reach ~0.5 dex for two Fe II lines—λλ5325.56 and 6369.46 Å. The solar profiles of these two lines cannot be reconciled with experimental oscillator strengths. Moreover, our $\log g_i f_{ij}$ values are in good agreement with the oscillator strengths of the VALD database [34] for all the Fe II lines we have used. The discrepancies typically do not exceed 0.09 dex, and reach 0.14 dex for only two Fe II lines.

We adopted the iron abundances [Fe/H] and microturbulence velocities ξ_t for the remaining stars from Fuhrmann [11], who determined his atmospheric parameters in the same way we did—from Fe II lines—but based on line-profile analyses.

We estimated the errors in the Mg abundances due to uncertainties in the stellar atmospheric parameters using numerical computations. Changes of 100 K, 0.1, and 0.3 km/s in $T_{\rm eff}$, $\log g$, and ξ_t translate into the following changes in the Mg abundance throughout the entire range of temperatures, $\log g$, and metallicities under consideration:

$$\Delta T_{\rm eff} = +100\ {\rm K} \longrightarrow \Delta\log\varepsilon_{\rm Mg} = 0.08\ {\rm dex};$$

$$\Delta\log g = +0.1 \longrightarrow \Delta\log\varepsilon_{\rm Mg} = -0.01\ {\rm dex};$$

$$\Delta\xi_t = +0.3\ {\rm km/s} \longrightarrow \Delta\log\varepsilon_{\rm Mg} = -0.02\ {\rm dex}.$$

The total error in the Mg abundance is 0.08 dex.

Table 3. Atomic parameters of Fe II lines used to determine metallicities and microturbulence velocities

λ, Å	E_i, eV	$\log g_i f_{ij}$	$\Delta\log C_6$
4416.82	2.78	−2.54	0.26
4491.40	2.85	−2.70	0.22
4508.28	2.85	−2.29	0.31
4515.34	2.84	−2.42	0.34
4520.23	2.81	−2.54	0.38
4576.33	2.84	−2.83	0.38
4620.52	2.83	−3.17	0.26
4923.93	2.89	−1.18	0.34
5100.66	2.81	−4.12	0.26
5132.67	2.81	−3.96	0.26
5136.80	2.84	−4.30	0.17
5197.57	3.23	−2.18	0.22
5234.63	3.22	−2.19	0.76
5256.93	2.89	−4.10	0.12
5325.56	3.22	−3.11	0.22
5425.26	3.20	−3.16	0.31
6149.25	3.89	−2.67	0.12
6247.56	3.89	−2.24	0.22
6369.46	2.89	−4.09	0.22
6383.72	5.55	−2.15	0.26
6432.68	2.89	−3.53	0.26

$\log g_i f_{ij}$ and $\Delta\log C_6$ are based on analysis of line profiles in the solar spectrum using the newKur model atmosphere.

Table 2 gives the atmospheric parameters of the stars studied. Parameters adopted from the papers noted above are indicated by superscripts. A superscript to a star's number indicates that we adopted all parameters—$T_{\rm eff}$, $\log g$, [Fe/H], and ξ_t—from the corresponding paper. Absence of a superscript means that the corresponding parameters were determined by us.

4. RESULTS

4.1. Non-LTE Magnesium Abundances

A detailed description of the model for the Mg atom and the technique used to compute the non-LTE Mg I atomic level populations can be found in [36, 37]. In the current study, we performed a differential analysis of the Mg abundances in 61 stars. We adopted the Sun as our reference star, and used the solar-spectrum atlas [38] based on flux observations to refine the non-LTE Mg abundances $\log\varepsilon_{\rm Mg}^{\odot}$ and atomic parameters of 18 Mg I lines in the interval λλ4570–12440 Å. We performed our analysis using the newKur model solar atmosphere [37]. The corresponding values for the Mg I lines used

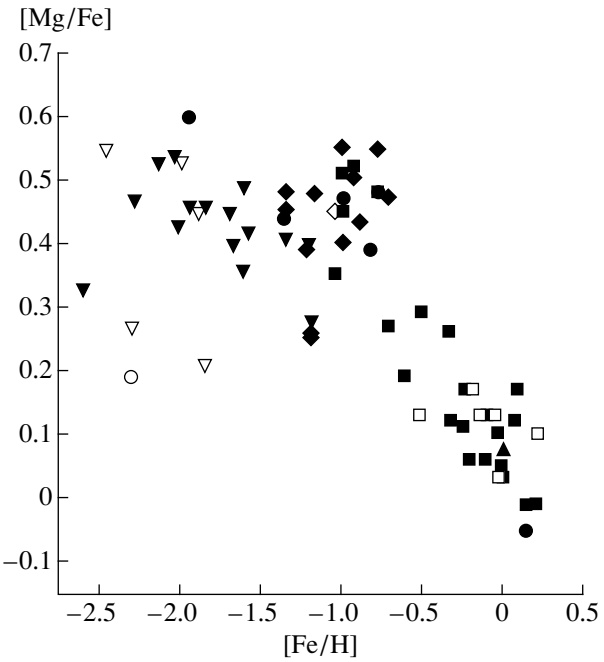

Fig. 5. The dependence of the Mg [Mg/Fe] abundance on metallicity [Fe/H]. The filled and open symbols show data for dwarfs and subgiants, respectively. The equivalent widths W_λ were adopted from [15] (downward triangles); [3] (diamonds); [13, 16] (squares); [7] (circles), and the Procyon atlas [18] (upward triangle).

here are summarized in Table 1, where $\Delta\log\varepsilon^{\odot}_{\rm Mg}$ are the individual non-LTE corrections to the standard Mg abundance (i.e., $\log\varepsilon^{\odot}_{\rm Mg}$ (non-LTE) = $\log\varepsilon^{\odot}_{\rm Mg}$ + $\Delta\log\varepsilon^{\odot}_{\rm Mg}$), and $\Delta\log C_6$ are corrections to the van der Waals broadening constant C_6. The mean non-LTE Mg abundance in the solar atmosphere derived in [37] based on all 18 lines is $\log\varepsilon^{\odot}_{\rm Mg} = 7.58 \pm 0.02$ dex. Note that this result is in agreement with the meteorite abundance of Grevesse *et al.* [29].

We performed the computations for the stars in our sample using Kurucz's [35] blanketed non-LTE model atmospheres. When necessary, we interpolated the model atmospheres in $T_{\rm eff}$ and $\log g$ using code kindly provided by Pimenov, Suleĭmanov, and Shimanskiĭ.

It is evident from Table 2 that the atmospheric parameters of the stars studied lie in the intervals 5000 K < $T_{\rm eff}$ < 6500 K, 3.5 < $\log g$ < 4.7, and –2.6 < [Fe/H] < +0.2. Mg I is not the main ionization stage in the atmospheres of such stars, and the character of non-LTE departures for the Mg I lines is determined by the depopulation of lower atomic levels compared to the LTE case. The neutral magnesium lines we use here form in a region where the depopulation of the lower level is greater than that of the upper level for the corresponding transition. Non-LTE Mg I line strengths are weaker compared to those for LTE analyses, implying positive non-LTE corrections to the Mg abundances. The departures from LTE for the stars studied are small, and non-LTE corrections $\Delta_{\text{non-LTE}} = \log\varepsilon^{\text{non-LTE}}_{\rm Mg} - \log\varepsilon^{\rm LTE}_{\rm Mg}$ lie in the range 0.04–0.15 dex.

Table 2 gives the non-LTE Mg abundances [Mg/Fe] derived from individual lines and the mean $\overline{[\text{Mg/Fe}]} \pm \sigma_{(n)}$ for various sources of equivalent widths. As a rule, the dispersion does not exceed 0.07 dex.

Our comparison of W_λ values in Section 2 revealed no systematic differences between the observations of [15], [3], and [7]. The data of [13, 16] are somewhat overestimated relative to the equivalent widths of [3]. However, the discrepancies between the equivalent widths of magnesium lines published in [16] and [3] are insignificant, implying that there should be no appreciable differences between abundances derived using these data. Indeed, the Mg abundances derived for a particular star from the W_λ values obtained in different studies and using different lines in a single spectral region differ by only 0.03–0.08 dex (Table 2). Only for HD 19445 does the difference between the [Mg/Fe] values for the data of Zhao and Magain [15] and of Gratton and Sneden [16] reach 0.19 dex.

As a rule, using Mg I lines from different spectral regions does not result in systematic differences between the inferred Mg abundances. For example, Mg I lines in the spectra of eight stars have been observed both in the visible [3, 15, 16, 18] and infrared [7, 16, 18]. The discrepancies between the Mg abundances for data obtained by a single set of authors range from –0.01 to +0.09 dex. Discrepancies between the Mg abundances of individual stars derived from equivalent widths measured by different authors range from –0.10 to +0.07 dex. The only exception is HD 76932, where the corresponding differences reach 0.17 and 0.12 dex when comparing results based on observations from a single study [16] and different studies [3, 16]. The Mg abundances derived using infrared lines can be both higher and lower than those determined from lines in the visible spectrum.

Thus, the use of Mg I equivalent widths measured in different studies or of lines from different spectral regions does not lead to any systematic differences between the inferred Mg abundances. We now analyze our results.

4.2. The [Mg/Fe]–[Fe/H] Relation

We analyzed the metallicity dependence of the Mg abundances averaged over all lines for all the stars studied (Fig. 5). The different symbols in Fig. 5 indicate different sources of the equivalent widths W_λ. The filled and open symbols show data for dwarfs and subgiants, respectively. Our results and conclusions remain unchanged if we determine the Mg abundances using a single line (e.g., λ5711 Å) for all stars for which such observations are available. It is evident from Fig. 5 that both dwarfs and subgiants exhibit the same [Mg/Fe]–

[Fe/H] dependence in the metallicity interval –2.6 < [Fe/H] < +0.2. Nissen and Schuster [3] and Nissen *et al.* [11] point out that [Mg/Fe] correlates with the kinematic parameters of stars. Therefore, we analyze the relations derived here taking into account the Galactic populations to which the corresponding stars belong.

At metallicities –2.6 < [Fe/H] < –0.7, magnesium exhibits a constant overabundance of 0.46 ± 0.06 dex relative to the Sun. The scatter of [Mg/Fe] for stars of similar metallicities ranges from 0.06 to 0.2 dex. The overabundance of magnesium relative to iron in old (i.e., metal-poor) stars indicates that the enrichment of the interstellar medium in α-process elements in the early stages of the Galaxy's evolution was primarily due to massive and short-lived stars exploding as type II supernovae. The corresponding epoch of Galactic evolution is identified as the period of formation of stars of the Galactic halo and *thick-disk*, whose ages do not exceed 12 Gyr [11].

We can also identify a group of stars that has lower Mg overabundances (+0.26 ± 0.04 dex on average) at metallicities [Fe/H] < –1.0 compared to the [Mg/Fe] values for other stars with similar [Fe/H]. For these stars, even non-LTE corrections to the Mg abundances failed to increase the [Mg/Fe] values. This group contains both dwarfs and subgiants, which do not differ from the other stars in their atmospheric parameters. We will now analyze the data for these stars.

The Mg abundances for HD 3567 and HD 122196 were derived from five and four lines, respectively, [15], and the rms errors do not exceed 0.06 dex. Moreover, we obtained similar [Mg/Fe] for HD 3567 values by analyzing the data of Nissen and Schuster [3]. One more star from the list of [3]—G102-020—has a relatively low Mg overabundance based on a single Mg I line. The Mg overabundances of other stars from [3], albeit derived from only one Mg I line at λ5711 Å, are typical of metal-poor stars. The equivalent width of this line in the spectrum of G102-020 is 67 mÅ. To reconcile the [Mg/Fe] inferred for this star with the mean [Mg/Fe] for halo stars, W_λ must be changed by 30%, which is much greater than the corresponding error. We therefore consider the Mg underabundance in the three stars noted above to be real.

The [Mg/Fe] values for the two halo stars HD 140283 and BD+3°0740 with metallicities [Fe/H] < –2.0 were determined from two lines measured by Zhao and Magain [15] and one line measured by Gratton and Sneden [13] (for HD 140283 only). These are highly metal-poor stars, and these lines are weak (their equivalent widths range from 14 to 45 mÅ). To bring the Mg abundances for these stars in line with those for other halo stars, W_λ must be changed by 15–20%, which is close to the rms errors in the equivalent widths of such weak lines when determined from observational data of the quality indicated above (see Section 2). Therefore, the inferred Mg underabundances in these two stars relative to other stars of similar metallicity could be due to the observational errors.

When analyzing the dependence of the abundances of α-process elements on metallicity [Fe/H], Nissen and Schuster [3] also point out differences between the overabundances of magnesium (and other elements—O, Si, Ca, Ti) for Galactic halo stars. A small group of stars exhibits Mg overabundances that are, on average, 0.17 dex lower than those of other metal-poor stars of the Galactic disk and halo. According to [3], these differences cannot be attributed to systematic errors in the inferred elemental abundances. Analysis of the [Mg/Fe]–[Fe/H] relation given by Fuhrmann *et al.* [39] also reveals a group of stars with [Fe/H] < –1.0. For these stars, Fuhrmann *et al.* [39] derived [Mg/Fe] values that are, on average, +0.18 dex lower than the overabundances for other stars with similar [Fe/H] ([Mg/Fe] ~ +0.31 dex).

The existence of halo stars with lower Mg abundances can be interpreted as follows. Fuhrmann [11] concludes that the degree of mixing is low in regions in the Galaxy where these stars formed. Nissen and Schuster [3] suggest that the rate of chemical evolution in the Galactic halo is lower than in the outer parts of the Galactic disk, and conclude that the chemical evolution of the Galaxy at low metallicities is more complex than assumed in many theoretical models. Thus, according to [3], even during early stages of the Galaxy's lifetime, iron enrichment in the interstellar medium due to stars exploding as type Ia supernova could have been much more important than usually believed. The low [Mg/Fe] values are due to an Fe overabundance rather than a magnesium deficiency. Therefore, stars with low Mg overabundances can be considered iron-rich. The authors of several recent papers concerning determinations of stellar chemical compositions (see, e.g., [3, 11]) discuss the possibility that such stars could have been acquired from other dwarf galaxies. Chemical-evolution models for such galaxies predict rather low [α/Fe] values at metallicities [Fe/H] ~ –1 [40, 41]. A number of authors [42, 43] have proposed that differences in [Mg/Fe] for metal-poor stars are due to the non-uniform nature of the Galactic halo: halo stars with small overabundances of magnesium (and other α-process elements) are members of the outer-halo population, which consists of stars acquired from dwarf galaxies, whereas halo stars with high [Mg/Fe] belong to the inner halo.

The Mg overabundance decreases abruptly at [Fe/H] ≃ –0.7: it changes from +0.46 dex, which is typical of very metal-poor stars, to ~+0.27 dex. With further increase in metallicity, the Mg abundance decreases smoothly to the solar value at [Fe/H] = 0.0.

At metallicities [Fe/H] > 0, there are three stars highly overabundant in Mg ([Mg/Fe] = +0.10…+0.17 dex): HD 9826, HD 187691, and HD 210855. Only one line—λ8717 Å—has been measured in the spectra of these stars [7]; changing its equivalent width by 6–13% could reduce the Mg abundances to the solar value. We therefore believe that the apparent Mg overabundance for

these stars is not real, and is due to the observational errors.

The abrupt change in the behavior of the [Mg/Fe]–[Fe/H] dependence at [Fe/H] = –0.7 indicates an epoch in the Galaxy's evolution when the rate of iron synthesis became higher than the rate of Mg synthesis. Fuhrmann [11] refers to this as the onset of the formation of the *thick disk*, whose age is 8–9 Gyr.

We also determined the Mg abundances in two halo stars from [17]: HD 134439 and CD –29°2277. In the case of CD –29°2277, the $T_{\rm eff}$ value derived from *R–I* was 360 K higher than that for *V–R*, corresponding to two different positions relative to the isochrones. If we adopt T_{RI}, the star does not lie on the corresponding isochrone in the $T_{\rm eff}$–$M_{\rm bol}$ diagram, determination of the star's mass becomes problematic, and the mass can only be estimated. On the other hand, if we adopt *V–R*, the star lies on the corresponding isochrone. The differences between the resulting $\log g$ values are small (0.15). It follows from the estimated Mg-abundance errors due to uncertainties in the atmospheric parameters (see Section 3) that this $\log g$ difference does not translate into substantial differences in [Mg/Fe]. However, the temperatures T_{RI} and T_{VR} for CD –29°2277 differ appreciably. This temperature difference leads to substantial differences in the Mg abundances: [Mg/Fe] is +0.38 ± 0.17 and +0.15 ± 0.07 dex for T_{RI} and T_{VR}, respectively. A comparison of the temperatures determined using different methods (see Section 3) together with the star's position on the $T_{\rm eff}$–$M_{\rm bol}$ diagram lead us to adopt the $T_{\rm eff}$ value derived from *V–R* for CD –29°2277. Note that the resulting Mg abundance has the lowest rms error in this case.

We obtained rather low [Mg/Fe] values for these two stars: –0.01 and +0.15 dex, respectively. In the spectrum of HD 134439, both Mg I lines are strong (W_λ = 100 and 200 mÅ), whereas the equivalent widths of these lines in the spectrum of CD –29°2277 do not exceed 100 mÅ. To reconcile the [Mg/Fe] values for these two stars with the mean value for halo stars, W_λ must be changed by 30–50%, which exceeds the corresponding rms errors. We thus conclude that the small Mg overabundances in HD 134439 and CD –29°2277 are real. Carney and Peterson [17] selected these stars based on their high (>400 km/s) spatial velocities. According to their kinematic parameters, both stars belong to the outer halo, possibly supporting the hypothesis that the outer and inner halos had different origins. Firmer conclusions can be drawn only after a detailed analysis of a larger sample of such stars.

4.3. Comparisons with Other Studies

We compared the metallicity dependences for our Mg abundances with the results obtained in other studies. It has been firmly established that a plateau should be observed in the [Mg/Fe]–[Fe/H] relation for halo and thick-disk dwarfs. The decrease of the Mg overabundance with increasing [Fe/H] is characteristic of slightly metal-poor stars of the Galactic thin disk.

In his analysis of a large sample of halo dwarfs (–3.0 < [Fe/H] < –1.3), Magain [9] found all stars in the metallicity interval considered to have an approximately constant Mg overabundance of 0.47 ± 0.09 dex. We also analyzed the stars from this sample (observations by Zhao and Magain [15]), and our conclusions coincide with those of Magain [9]. However, our redetermination of the atmospheric parameters of the stars shifted them toward higher metallicities (–2.3 < [Fe/H] < –1.2).

The chemical composition of a sample of halo and disk stars was analyzed by Nissen and Schuster [3], who found that both halo and disk stars exhibit a constant [Mg/Fe] value of ~+0.27 dex at metallicities [Fe/H] < –0.6, lower than the value we obtained. These discrepancies in the Mg overabundances are due, first, to the neglect of non-LTE effects in [3], and second, to the different model atmosphere parameters adopted. Note that our refinement of $T_{\rm eff}$, $\log g$, and [Fe/H] for the stars from [3] shifted them toward lower metallicities, thereby increasing [Mg/Fe]; the new temperatures differ from the old ones by 40–180 K. The differences in $\log g$ do not exceed 0.5 dex, resulting in insignificant changes in the resulting Mg abundances. Nissen and Schuster [3] note that the Mg overabundance decreases to the solar value at [Fe/H] > –0.6, and point out a small group of eight halo stars with real, albeit low, Mg overabundances of +0.10 dex. We also note a group of metal-poor stars ([Fe/H] < –1) with [Mg/Fe] values that are, on average, 0.2 dex lower than the overabundances for other stars with similar metallicities.

Fuhrmann [11] studied stars belonging to the halo, thick disk, and thin disk of the Galaxy in a wide metallicity interval (–2.0 < [Fe/H] < +0.4), and analyzed the results taking into account the membership of the stars in various Galactic subsystems. Fuhrmann [11] found that the [Mg/Fe]–[Fe/H] relations for the halo and thick-disk stars differ from that for thin-disk stars. On the whole, our relations agree with those of [11]. Fuhrmann [11] obtained a constant Mg overabundance of +0.4 dex for halo and thick-disk stars with [Fe/H] < –0.3, which is 0.06 dex lower than our value. This discrepancy can be explained by Fuhrmann's [11] neglect of departures from LTE. According to [11], the Mg overabundance in thin-disk stars with metallicities [Fe/H] > –0.5 decreases with increasing iron abundance. We found our [Mg/Fe]–[Fe/H] relation to exhibit a similar trend when [Fe/H] > –0.7. Fuhrmann's [11] [Mg/Fe] values for thick-disk and thin-disk stars differ by 0.2 dex in the region where their metallicities overlap. We found the Mg overabundance to decrease abruptly by the same value at [Fe/H] = –0.7, which could be a manifestation of the fact that these stars belong to different Galactic subsystems.

5. CONCLUSIONS

We have redetermined the Mg abundances for 61 F–K dwarfs and subgiants based on published observations of Mg I lines in the visible and infrared, allowing for departures from LTE in the Mg I lines. The non-LTE corrections to the Mg abundances of the stars studied do not exceed +0.15 dex. When possible, we refined the atmospheric parameters of the stars.

In our analysis of the [Mg/Fe]–[Fe/H] relation in the metallicity interval $-2.6 < [Fe/H] < +0.2$, we found metal-poor stars ($[Fe/H] < -0.7$) to exhibit a constant Mg overabundance of +0.46 dex relative to the Sun. The overabundance of magnesium in old stars compared to the Sun suggests a dominant contribution of type II supernovae to the enrichment of the interstellar medium in α-process elements at early stages of Galactic evolution. The Mg overabundance decreases abruptly to +0.27 dex at $[Fe/H] = -0.7$. The Mg abundance decreases smoothly with further increase of the metallicity, to the solar value at $[Fe/H] = 0.0$. This qualitative change in the behavior of the [Mg/Fe]–[Fe/H] relation indicates that, beginning with this epoch ($[Fe/H] < -0.7$), type Ia supernovae dominated over type II supernovae as a source of enrichment of the interstellar medium. We an identify a group of stars with lower Mg overabundances (+0.26 dex) at $[Fe/H] < -1.0$. These differences in the Mg abundances of metal-poor stars cannot be attributed to observational errors or errors in the adopted stellar atmospheric parameters.

Thus far, theoretical models of Galactic chemical evolution have failed to describe observed [Mg/Fe]–[Fe/H] relations both quantitatively (the theoretical Mg overabundances are lower than the observed overabundances in metal-poor—i.e., halo and thick-disk—stars), and qualitatively (the absence of a plateau and jump in the overabundance in the transition to thin-disk stars). It is desirable to take into account these observational facts in subsequent modeling.

Note that [Fe/H] is traditionally considered to be a function of time, forming a basis for the "age–metallicity" relation for Galactic stars. The existence of stars with similar metallicities but different overabundances of magnesium (and other α-process elements, according to [3]) may indicate that [X/Fe] values (i.e., elemental abundances relative to that of iron) are not functions of [Fe/H] alone. It appears necessary to take into account the Galactic subsystems to which stars belong.

ACKNOWLEDGMENTS

We are sincerely grateful to N.A. Sakhibullin for discussions of the results reported here. This work was partially supported by the Russian Foundation for Basic Research (project code no. 99-02-17488-a).

REFERENCES

1. A. Hoyle, Astrophys. J., Suppl. Ser. **1**, 121 (1954).
2. W. Steenbook, Astron. Astrophys. **126**, 325 (1983).
3. P. E. Nissen and W. J. Schuster, Astron. Astrophys. **326**, 751 (1997).
4. P. Francois, Astron. Astrophys. **160**, 264 (1986).
5. J. B. Laird, Astrophys. J. **303**, 718 (1986).
6. R. G. Gratton and C. Sneden, Astron. Astrophys. **178**, 179 (1987).
7. B. Edvardsson, J. Andersen, B. Gustafsson, *et al.*, Astron. Astrophys. **275**, 101 (1993).
8. Y. Q. Chen, P. E. Nissen, G. Zhao, *et al.*, Astron. Astrophys., Suppl. Ser. **141**, 491 (2000).
9. P. Magain, Astron. Astrophys. **209**, 211 (1989).
10. P. E. Nissen, B. Gustafsson, B. Edvardsson, and G. Gilmore, Astron. Astrophys. **285**, 440 (1994).
11. K. Fuhrmann, Astron. Astrophys. **338**, 161 (1998).
12. F. X. Timmes, S. E. Woosley, and T. A. Weaver, Astron. Astrophys., Suppl. Ser. **98**, 617 (1995).
13. R. G. Gratton and C. Sneden, Astron. Astrophys. **204**, 193 (1988).
14. F. Matteucci and P. Francois, Mon. Not. R. Astron. Soc. **239**, 885 (1989).
15. G. Zhao and P. Magain, Astron. Astrophys., Suppl. Ser. **86**, 85 (1990).
16. R. G. Gratton and C. Sneden, Astron. Astrophys., Suppl. Ser. **68**, 193 (1987).
17. B. W. Carney and R. C. Peterson, Astrophys. J. **245**, 238 (1981).
18. R. Griffin and E. Griffin, *A Photometric Atlas of the Spectrum of Procyon* (Cambridge Univ. Press, Cambridge, 1979).
19. A. Alonso, S. Arribas, and C. Martínez-Roger, Astron. Astrophys. **313**, 873 (1996).
20. A. Alonso, S. Arribas, and C. Martínez-Roger, Astron. Astrophys., Suppl. Ser. **117**, 227 (1996).
21. B. W. Carney, Astron. J. **88**, 610 (1983).
22. B. W. Carney, Astron. J. **88**, 623 (1983).
23. H. L. Johnson, Ann. Rev. Astron. Astrophys. **4**, 193 (1966).
24. I. F. Bikmaev, Candidate's Dissertation in Mathematical Physics (Nizhniĭ Arkhyz, 1991).
25. *ESA 1997, The Hipparcos and Tycho Catalogues*, ESA SP-1200.
26. P. A. Bergbusch and D. A. VanderBerg, Astrophys. J., Suppl. Ser. **81**, 163 (1992).
27. P. E. Nissen, E. Hog, and W. L. Schuster, in *Hipparcos, Venice'97*, Ed. by B. Battrick (ESA, Noordwijk, 1997), ESA SP-402.
28. F. Thevenin and T. P. Idiart, Astrophys. J. **521**, 753 (1999).

29. N. Grevesse, A. Noels, and A. J. Sauval, Astron. Soc. Pac. Conf. Ser. **99**, 117 (1996).

30. R. Schnabel, M. Kock, and H. Holweger, Astron. Astrophys. **342**, 610 (1999).

31. C. Hiese and M. Kock, Astron. Astrophys. **230**, 244 (1990).

32. S. Kroll and M. Kock, Astron. Astrophys., Suppl. Ser. **67**, 225 (1987).

33. J. Moity, Astron. Astrophys., Suppl. Ser. **52**, 37 (1983).

34. F. Kupka, N. Piskunov, T. A. Ryabchikova, *et al.*, Astron. Astrophys., Suppl. Ser. **138**, 119 (1999).

35. R. L. Kurucz, CD-ROM No. 13, 1994.

36. L. I. Mashonkina, N. N. Shimanskaya, and N. A. Sakhibullin, Astron. Zh. **73**, 212 (1996) [Astron. Rep. **40**, 187 (1996)].

37. N. N. Shimanskaya, L. I. Mashonkina, and N. A. Sakhibullin, Astron. Zh. **77**, 893 (2000) [Astron. Rep. **44**, 530 (2000)].

38. R. L. Kurucz, I. Furenlid, J. Brault, and L. Testerman, *Solar Atlas from 296 to 1300 nm* (National Solar Observatory, Sunspot, New Mexico, 1984).

39. K. Fuhrmann, M. Axer, and T. Gehren, Astron. Astrophys. **301**, 492 (1995).

40. G. Gilmore and R. F. G. Wyse, Astrophys. J. Lett. **367**, L55 (1991).

41. T. Tsujimoto, K. Nomoto, Y. Yoshii, *et al.*, Mon. Not. R. Astron. Soc. **277**, 945 (1995).

42. R. Zinn, Astron. Soc. Pac. Conf. Ser. **48**, 38 (1993).

43. A. Márquez and W. J. Schuster, Astron. Astrophys., Suppl. Ser. **108**, 341 (1994).

Translated by A. Dambis

Astronomy Reports, Vol. 45, No. 2, 2001, pp. 113–119. Translated from Astronomicheskiĭ Zhurnal, Vol. 78, No. 2, 2001, pp. 137–144.

The Maser Source S140–H_2O as a Protoplanetary Disk

E. E. Lekht[1, 2] and R. L. Sorochenko[3]

[1]*Sternberg Astronomical Institute, Universitetskiĭ pr. 13, Moscow, 119899 Russia*

[2]*National Institute of Astrophysics, Physics, and Electronics, Tonanzintla, México*

[3]*Pushchino Radio Astronomy Observatory, Astro Space Center, Lebedev Physical Institute, Pushchino, Moscow oblast, Russia*

Received January 17, 2000

Abstract—We present the observations of the H_2O maser in S140 with the 22-m radio telescope of the Pushchino Radio Astronomy Observatory in 1992–1999. The H_2O maser emission is mainly concentrated in three symmetrically placed narrow radial-velocity intervals. In contrast to our earlier observations (1981–1991), we did not detect emission simultaneously in all three intervals; instead, the emission appeared successively in each. We discuss possible origins for this behavior. To explain the flux variability and radial-velocity drift of the main components, we propose a model with Keplerian orbital motion of clumps (protoplanets) and calculate their orbital parameters. © *2001 MAIK "Nauka/Interperiodica".*

1. INTRODUCTION

Long-term monitoring of H_2O maser sources in star-forming regions enables the study of the evolution of individual emission features in the spectrum over extended time intervals. In addition to the intensity of a component, its radial velocity and temporal variations are important parameters. In the selection of optimal models for a source, VLA maps showing the distributions of maser spots at specific epochs are of considerable importance, as is the variability of the radial velocity and fluxes of the most persistent components.

Torelles *et al.* [1, 2] report the detection of fairly compact groups of maser spots, which they identified with Keplerian (protoplanetary) disks (NGC 2071 and W75N). Lekht [3] also presents results for the H_2O maser in W75N. Studies of the variability of the W75N H_2O maser have been carried out for 15 years. A radial-velocity drift over six years was detected for a persistent component at 12.5 km/s. This drift strongly resembles the behavior of the –12.2 km/s component in S140, for which a Keplerian-disk model has been suggested [4]. In addition, short-period radial-velocity variations within 0.2 km/s were detected for these two components in W75N and S140 [5]. Such variations could be the result of small-scale turbulence in a Keplerian disk. The lack of detailed VLA maps of the W75N region hindered the selection of a preferred specific model for the source. However some more or less realistic suggestions were presented in [3], including the existence of a Keplerian disk.

S140 provides an excellent example of maser sources in star-forming regions that can be identified with Keplerian disks. The maser S140–H_2O is in the dark molecular cloud L1204, which has been mapped in CO [6, 7] and NH_3 [8]. The most accurate determination of the velocity of the cloud (core) was based on the NH_3 line (–7 km/s). This means that the radial component of the peculiar velocity of S140–H_2O is about +4 km/s, and does not exceed the gas turbulent-velocity dispersion derived from CO observations [7]. In the L1204 cloud, there are several IR sources [9] and supercompact H II regions [10]. The supercompact H II region G106.797+5.312 coincides with the brightest IR source (IRS 1) [11], in the same direction as the H_2O maser.

S140–H_2O was discovered in 1975 by White and Little [12]. The maser's spectrum maintains a certain regularity over long times. At some epochs, stable emission has been observed in three radial-velocity intervals separated by approximately equal gaps [4, 12]. The disappearance of a component in the H_2O spectrum could be due to an anticorrelation of the intensities of the components [4], which can be explained by models with competing spatial emission modes in a partially saturated disk maser with anisotropic pumping [4, 13].

The current paper continues our studies of the evolution of the H_2O maser emission in S140.

2. OBSERVATIONS AND DATA

We present the results of observations of the H_2O maser emission in the 1.35-cm line toward S140 carried out on the 22-m radio telescope in Pushchino in 1992–1999. The mean interval between observations was about two months. The system has a front-end cooled transistor amplifier, providing a noise temperature of 150–200 K. We used a 128-channel filter spectrum ana-

1063-7729/01/4502-0113$21.00

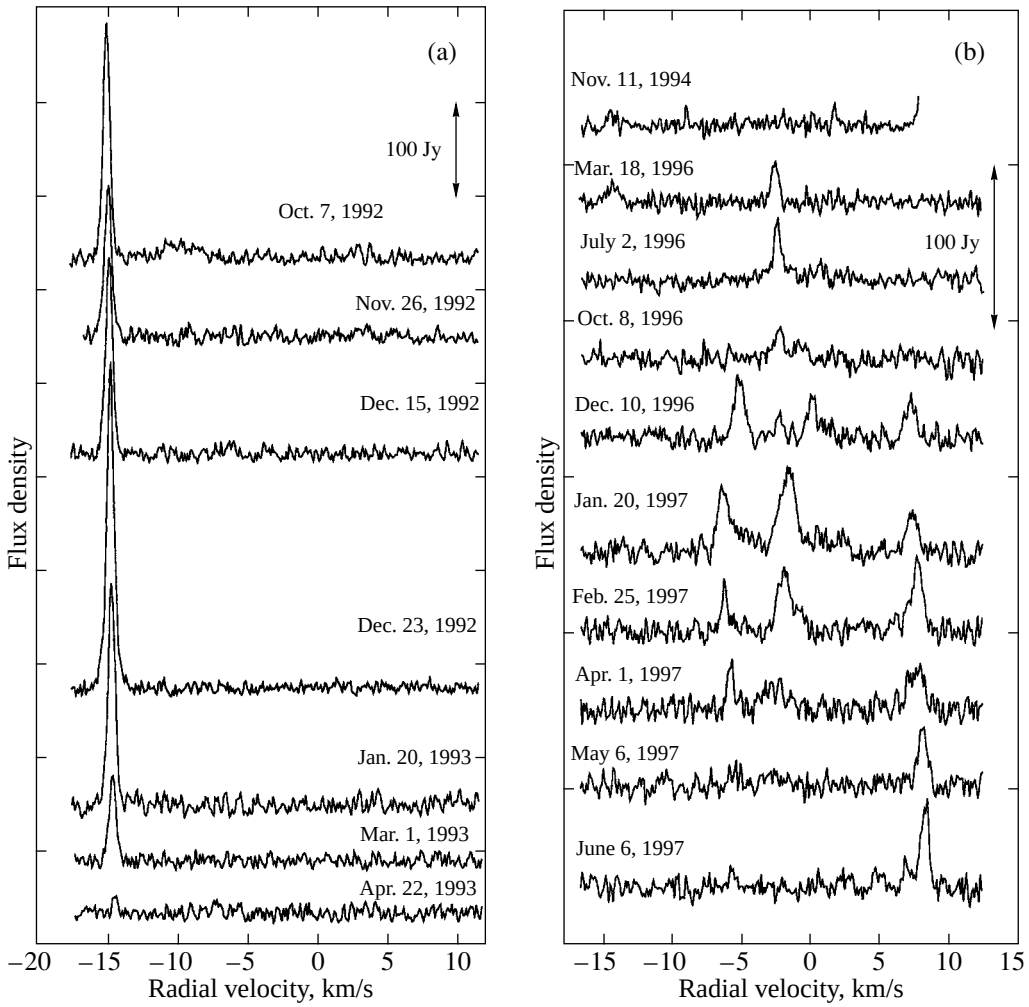

Fig. 1. The maser emission spectra of the H_2O source in S140 obtained in 1992–1999. The vertical line with arrows indicates the distance between major ticks in Jy.

lyzer with 7.5-kHz resolution (0.101 km/s in radial velocity for the 1.35 cm line).

Figure 1 presents our results for the period from October 1992 until September 1999. We plot the flux density in Jy as a function of the radial velocity relative to the LSR in km/s (the scale in Jy is indicated by the vertical arrow). For convenience, all the spectra are plotted on the same scale. The spectra in Fig. 1a cover the final evolution of the "blue" component with a radial velocity of about –15 km/s. The flux and radial-velocity variations during this stage (Fig. 2) are consistent with the predictions of the model with a clump of masing material moving along a Keplerian orbit suggested by us earlier [4]. From 1993 until January 1996, we detected maser emission in S140 only once, on November 11, 1994. On other dates in this period, we did not detect any emission with flux above 3–5 Jy. These spectra are not displayed in Fig. 1.

Subsequently, over more than three years starting in early 1996, we observed emission at velocities from –15 to +10 km/s. The blue component appeared only for a very short time, in the beginning of 1996. The red emission (at positive velocities) was the most persistent. In general, the maser emission during this time interval was considerably weaker than in 1980–1992. In addition, there is no clear triplet structure in any of the 1992–1999 spectra.

Rather interesting results emerged in the analysis of the spectra for specific time intervals. We subdivided the period from 1992 to 1999 into five intervals (Fig. 3). The large time gap between the first and second intervals is due to the lack of detection of maser emission from June 1993 until January 1996. In each of these five time intervals, one, or at most two, groups of features dominate. For example, a central group and "red" group (at positive radial velocities) were observed in 1997. We obtained mean spectra for each of the intervals, shown in

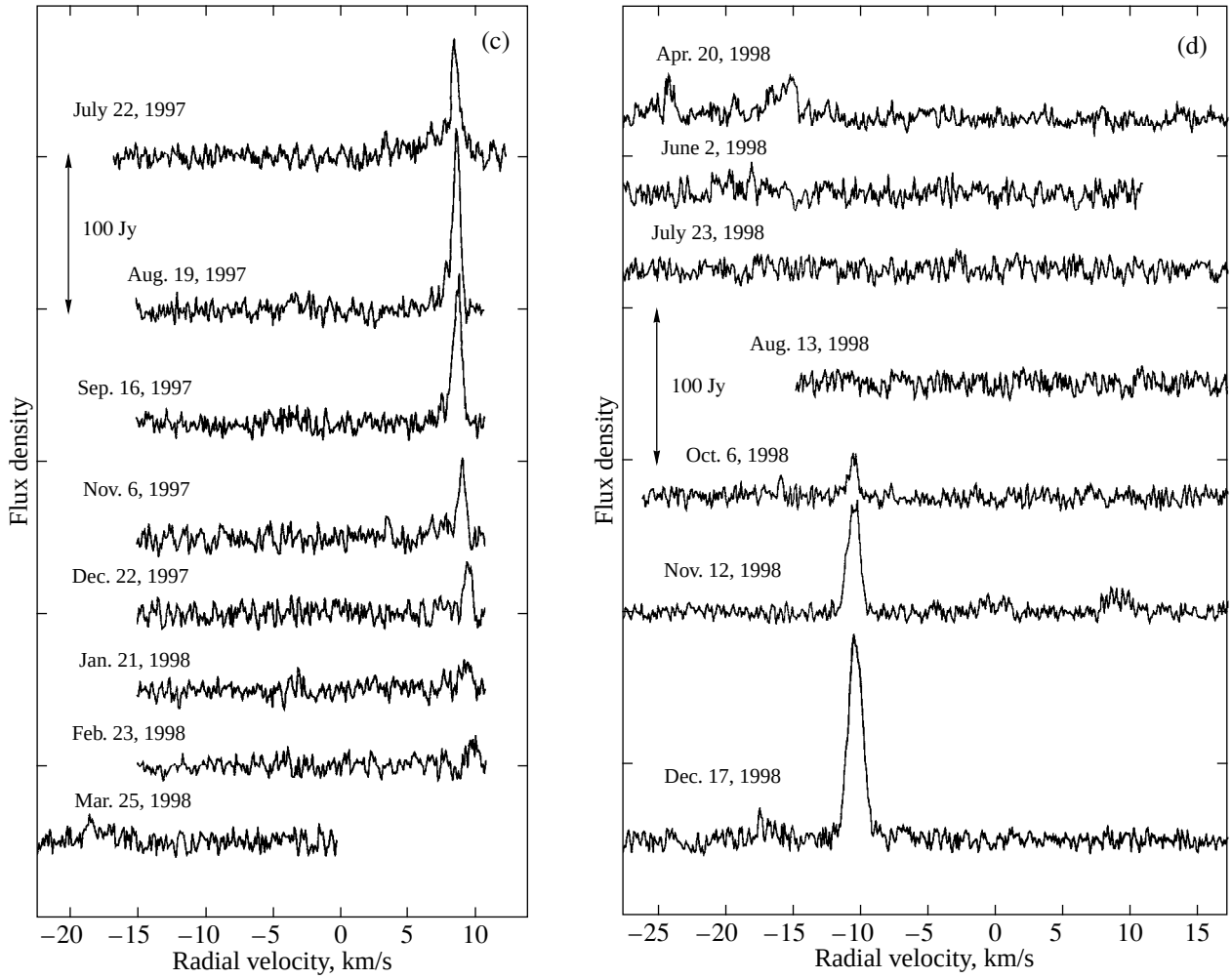

Fig. 1. (Contd.)

Fig. 3, with the boundaries for the adopted time intervals also indicated. We can clearly see that the emission from the three groups of features—blue, central, and red—appear in turn. In addition, weak emission emerges briefly at intermediate velocities. We observed similar emission earlier [4].

We determined the properties of individual components via Gaussian fitting. Both the side groups and the central group usually contained from one to three features, so this was not difficult unless a component had low intensities.

From February 1997 until April 1998, there was a significant radial-velocity drift of the component at ~9 km/s (Fig. 4), of 2.8 km/s in 14 months. Weaker velocity drifts were observed for other components as well (Fig. 5), but their lifetimes in the active phase were much shorter, from three months to one year.

Figure 6 illustrates the flux and radial-velocity variability of components with radial velocities from –11.5 to –7.5 km/s during 1998–1999. We first detected emission at these velocities in 1981, with the exception of weak emission detected in October 1992. The radial-velocity variations for these components were small.

3. DISCUSSION

3.1. The Triplet Structure

During our 1992–1999 observations of S140–H_2O, we never detected the triplet spectral structure characteristic of H_2O masers associated with Keplerian disks. However, emission appeared in turn in the blue (in the final stage of evolution), central, red, and again blue region of the H_2O spectrum (Fig. 3). The duration of the emission in each of these spectral regions was from 7 to 15 months. Note that the seven-month duration for the blue component refers only to the final stage of its evolution, whereas its total lifetime was 6.5 years.

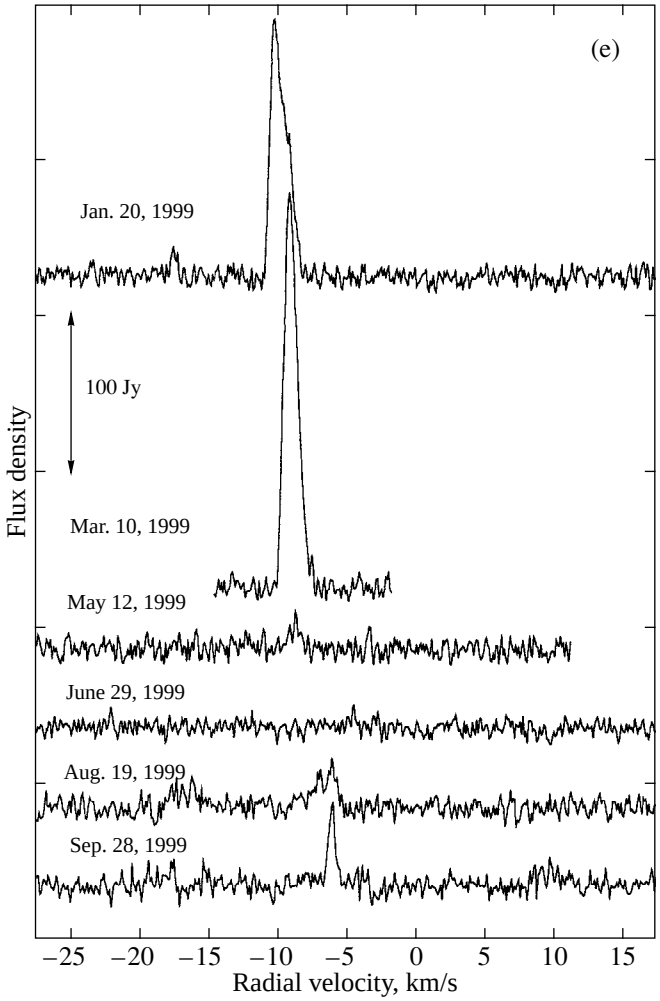

Fig. 1. (Contd.)

The successive appearance of emission in the two side components and central component could have various origins. One possible origin is an anticorrelation of the fluxes of the side and central components, or the fluxes of the two side components. This can occur in an at least partially saturated maser. The degree of saturation of the maser can be estimated if there is a functional relation between variations in the intensity and line width. However, there being no isolated features in the spectra, we were not able to follow the variability in the line widths of individual components sufficiently accurately to detect such a relation.

Note that, thus far, the state of the central star has not been analyzed for masers associated with Keplerian disks. A star in the process of forming can have activity maxima and minima. During an activity minimum, the maser could be partially saturated, with the emission weaker than it was before 1992. In this case, models with competing spatial emission modes in a partially saturated disk could also operate, with the central or side components suppressed as a consequence.

Nonuniformity of the physical parameters (density, temperature, density of active molecules, etc.) in the disk leads to differences in the amplification coefficients for the chord modes responsible for the side components, possibly resulting in an anticorrelation of their intensities.

It is also possible that the explanation of Fig. 3 lies in the structure of the protoplanetary disk and the presence of large-scale inhomogeneities in it.

3.2. The Blue Component

Starting in 1992, we observed the final stage in the evolution of the most persistent component in S140. Its flux and velocity variations were in agreement with the model [4] suggested earlier for the S140 maser. Figure 7 shows the positions of this component (clump) at various epochs starting with 1987 (data prior to 1992 are

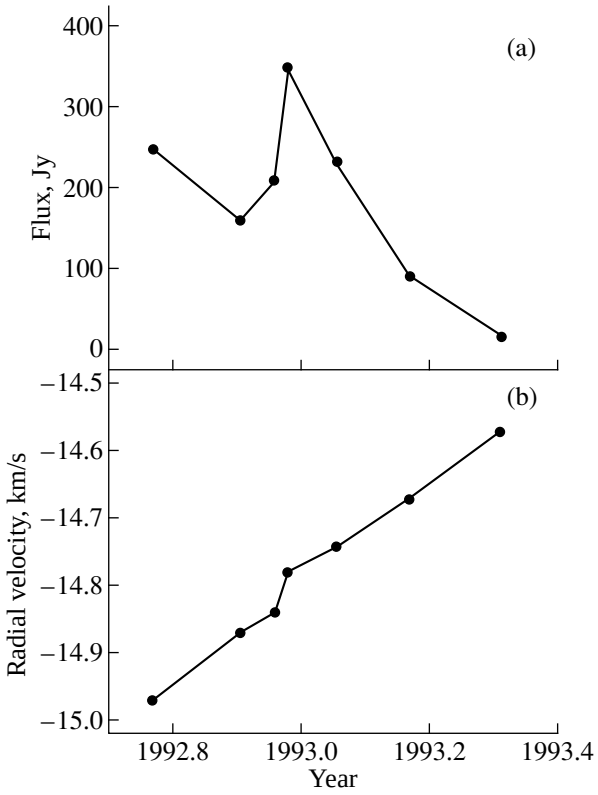

Fig. 2. Variability of the "blue" component's flux and radial velocity during the final stage of its evolution.

from [4]). The full lifetime of the component was 6.5 years. In this model, the gradual decrease of the emission and its complete disappearance by the end of 1992 indicate that the component has left the amplification "corridor" of the Keplerian disk. The radial-velocity changes from mid-1986 to late 1992 were nearly sinusoidal, corresponding to Keplerian motion in the field of the central star.

3.3. The Red Component

The most significant radial-velocity drift was observed for the component with V_{mean} = 9 km/s in 1997–1998: 2.8 km/s in 14 months, with the rate of change in the radial velocity equal to 2.4 km/s per year. This component's velocity relative to the velocity of the star, which we adopted to be –3 km/s [4], is +12 km/s. This velocity is not orbital: its rate of change is too high, and it is probable that $V_{orbit} > 12$ km/s. In this case, the clump responsible for the emission at this velocity is closer to the star than the blue component, and the observed velocity is the projection of the orbital velocity. Figure 7 shows the most probable position of the maser emission region with V_{mean} = 9 km/s according to our earlier model.

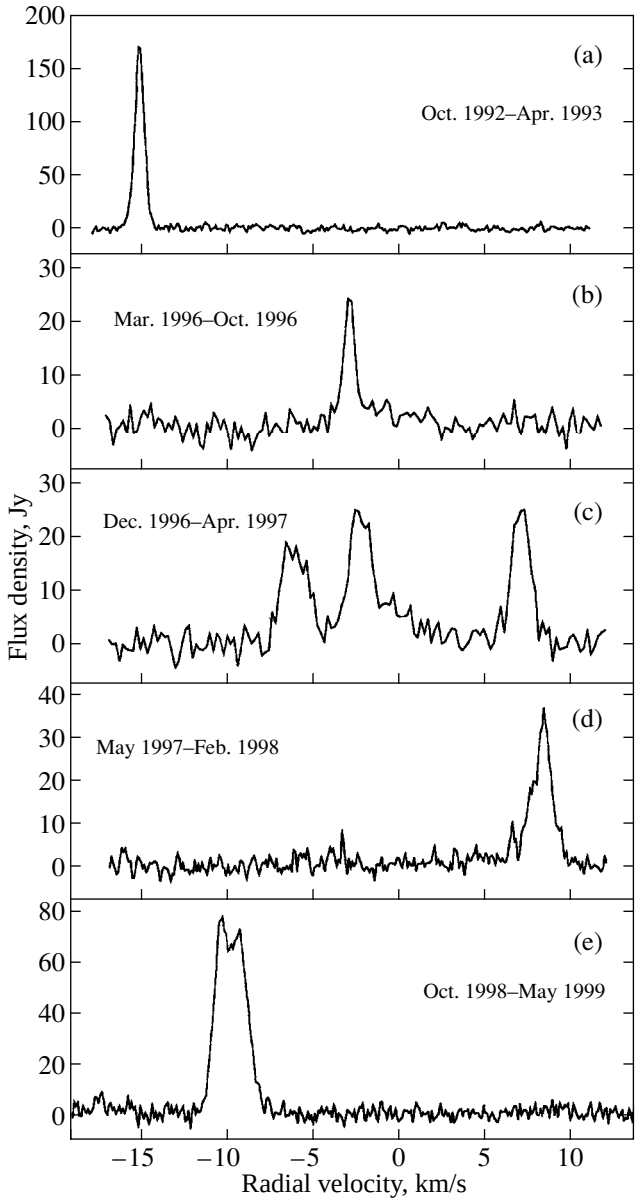

Fig. 3. Mean H_2O spectra for S140 in various time intervals.

The radial velocity of a maser condensation varies as

$$V_1(\varphi) = V_1 \cos\varphi, \quad (1)$$

where V_1 is the condensation's orbital velocity and φ is the angle between the radius vector and the plane of the sky. Differentiating Eq. (1), we find a relation between the rate of change of the radial velocity and the angular velocity:

$$\frac{dV_1}{dt} = -V_1 \sin\varphi \frac{d\varphi}{dt}. \quad (2)$$

After minor manipulations, using Eq. (1), we obtain

$$\frac{dV_1}{dt} = -V_1(\varphi)\tan\varphi\frac{d\varphi}{dt} = -V_1(\varphi)\tan\varphi\frac{2\pi}{T_1}, \quad (3)$$

where T_1 is the condensation's orbital period.

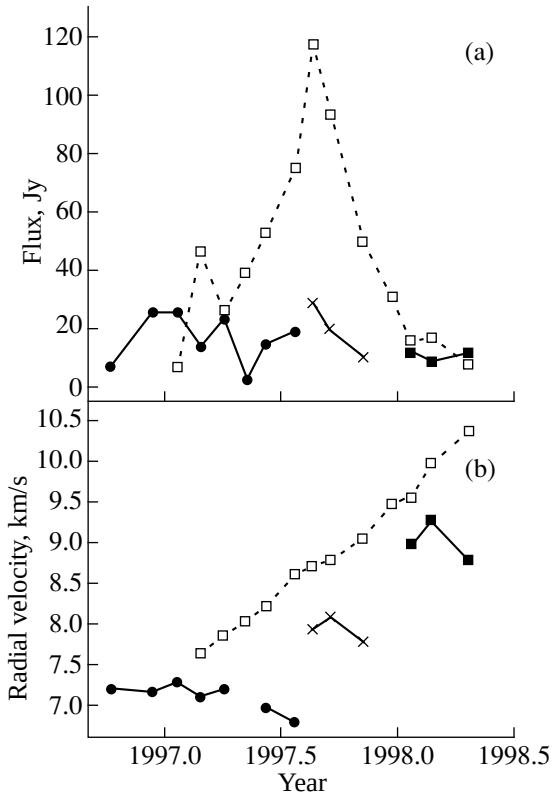

Fig. 4. Same as Fig. 2 for the "red" component.

We will also use the orbital velocity, distance, and period (V_0 = 12.5 km/s, R_0 = 30 AU, and T_0 = 70 yr) found for the blue component in [4]. The orbital parameters for the two components are related by the expressions

$$\frac{R_1}{R_0} = \left(\frac{V_0}{V_1}\right)^2, \quad (4)$$

$$\left(\frac{R_1}{R_0}\right)^3 = \left(\frac{T_1}{T_0}\right)^2. \quad (5)$$

We now substitute into Eq. (3) dV_1/dt = 2.4 km s^{-1} yr^{-1} and $V_1(\varphi)$ = 12 km/s. The system of Eqs. (3)–(5) has a solution for φ = 40°–45°. Thus, the observed rate of change of the radial velocity, 2.4 km s^{-1} yr^{-1}, corresponds to an angular velocity $d\varphi/dt \approx 11.5°$/yr. The corresponding orbital period is $T_1 \approx 29$ yr. The resulting distance to the central star is 17 AU, and the orbital velocity is ≈16.5 km/s.

Of course we cannot exclude other origins for the observed radial-velocity drift of the emission. For example, in the presence of a velocity gradient, a spatial shift of the region of maser emission could lead to the observed shift in the H_2O spectrum. There could exist ordered fragments, such as chains of small clumps of matter. In this case, however, successive excitation of the chain's elements should result in observable veloc-

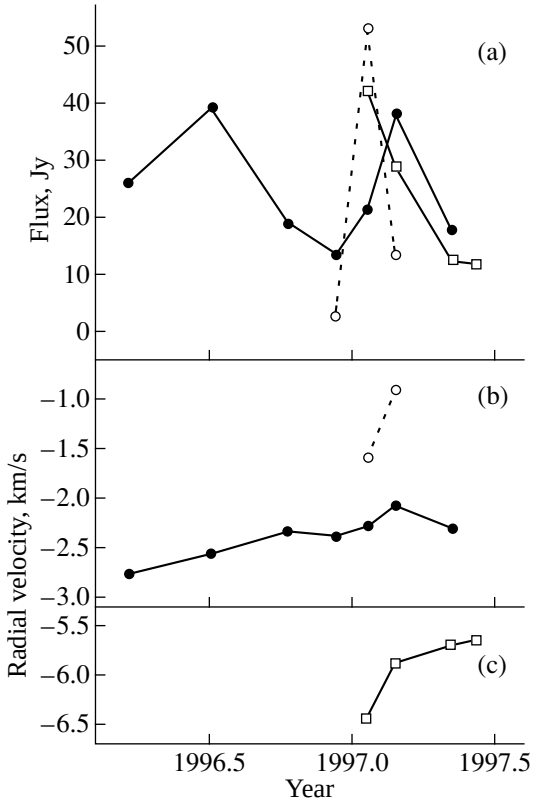

Fig. 5. Same as Fig. 2 for the central group.

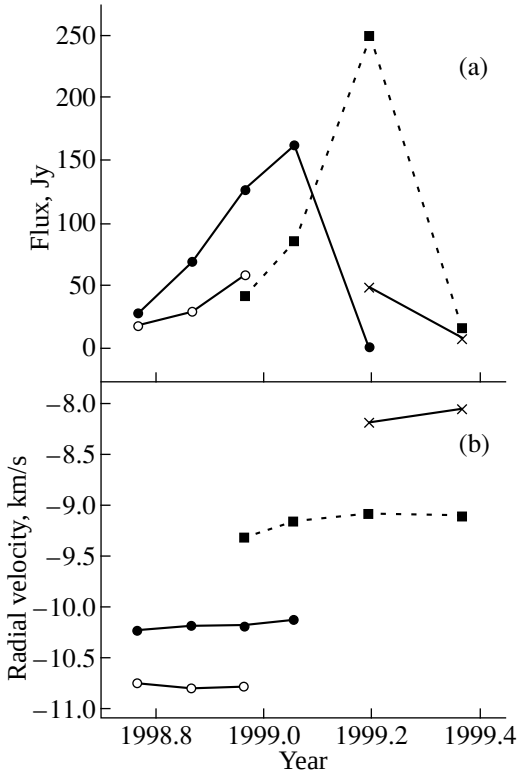

Fig. 6. Same as Fig. 2 for the components with radial velocities from –11 to –8 km/s.

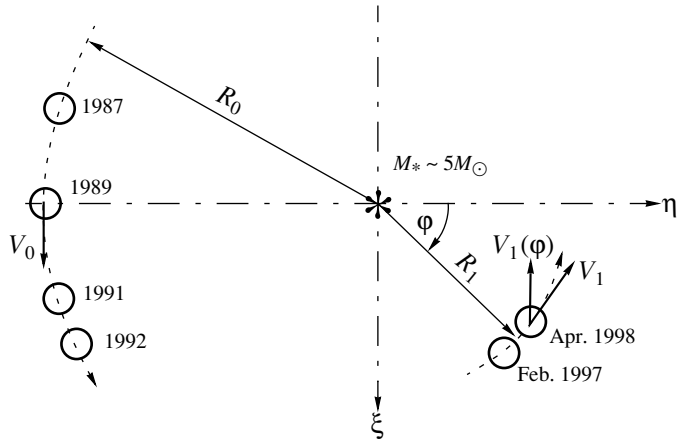

Fig. 7. Model for the "blue" and "red" components of the water-vapor maser in S140. The ξ axis points toward the observer. The dashed lines show the trajectories of two dense condensations. V_0, V_1, R_0, and R_1 are their orbital velocities and distances from the star. The circles show the positions of the condensations in their trajectories for the indicated dates.

ity jumps and flux variations, which are not observed. Thus, we prefer the model of a condensation in a Keplerian orbit for this component.

4. CONCLUSIONS

We have presented the results of our observations of the H_2O maser in S140 in 1992–1999. We have identified individual components in the spectrum and followed the evolution of their principal parameters: flux density and radial velocity. Using the Keplerian-disk model introduced earlier in [4], we calculated the parameters of the motion of the "red" component in the field of the central star ($R \approx 17$ AU, $V_{\rm orbit} \approx 16.5$ km/s, and $T \approx 29$ yr). We confirm that the motion of the "blue" component in 1992 followed the same nearly sinusoidal trajectory as it had earlier.

We observed the appearance of emission in turn in the blue (in the final stage of evolution), central, red, and again blue regions of the H_2O spectrum. The emission phase in each region lasted from 7 to 15 months. The seven-month duration for the blue component refers only to the final stage of its evolution, and its total lifetime was 6.5 yr. The successive appearance of emission in the side components and central component could result from competition for pumping among different spatial emission modes, or simply from the geometric peculiarities of a Keplerian disk containing large-scale inhomogeneities.

Of course our model of clumps (protoplanetary formations) moving in a Keplerian disk must be confirmed by VLBI observations.

ACKNOWLEDGMENTS

This study was made possible by support for the RT-22 (Reg. no. 01-10) radio telescope in Pushchino from the State Committee for Science and Technology of the Russian Federation. Our work was also supported by the Russian Foundation for Basic Research (project code 99-02-16293). We thank the staff of the Pushchino Radio Astronomy Observatory for their valuable assistance during the observations.

REFERENCES

1. J. M. Torrelles, J. F. Gómez, L. F. Rodríguez, *et al.*, Astrophys. J. **489**, 744 (1997).
2. J. M. Torrelles, J. F. Gómez, L. F. Rodríguez, *et al.*, Astrophys. J. **505**, 756 (1998).
3. E. E. Lekht, Astron. Zh. **72**, 31 (1995) [Astron. Rep. **39**, 27 (1995)].
4. E. E. Lekht, S. F. Likhachev, R. L. Sorochenko, and V. S. Strel'nitskiĭ, Astron. Zh. **70**, 731 (1993) [Astron. Rep. **37**, 367 (1993)].
5. R. L. Sorochenko, E. E. Lekht, and J. E. Mendoza-Torres, Astron. Zh. **75**, 674 (1998) [Astron. Rep. **42**, 592 (1998)].
6. G. N. Blair, N. J. Evans, P. A. van der Bout, and W. L. Peters, Astrophys. J. **219**, 896 (1978).
7. W. Gilmore, Astron. J. **85**, 623 (1980).
8. H. Ungerechts, C. M. Walmsley, and G. Winnewisser, Astron. Astrophys. **157**, 207 (1986).
9. C. A. Beichman, E. E. Becklin, and C. G. Wynn-Williams, Astrophys. J. Lett. **232**, L47 (1978).
10. M. Simon, M. Felli, L. Cassar, *et al.*, Astrophys. J. **266**, 623 (1983).
11. S. Kurtz, E. Churchwell, and D. O. S. Wood, Astrophys. J., Suppl. Ser. **91**, 659 (1994).
12. G. J. White and L. T. Little, Astrophys. J. **16**, 151 (1975).
13. R. Cesaroni, Astron. Astrophys. **233**, 513 (1990).

Translated by N. Samus'

Astronomy Reports, Vol. 45, No. 2, 2001, pp. 120–137. Translated from Astronomicheskiĭ Zhurnal, Vol. 78, No. 2, 2001, pp. 145–164.

Wolf–Rayet Stars and Relativistic Objects: Distinctions between the Mass Distributions in Close Binary Systems

A. M. Cherepashchuk

Sternberg Astronomical Institute, Universitetskiĭ pr. 13, Moscow, 119899 Russia

Received March 27, 2000

Abstract—The observed properties of Wolf–Rayet stars and relativistic objects in close binary systems are analyzed. The final masses $M_{\rm CO}^f$ for the carbon–oxygen cores of WR stars in WR + O binaries are calculated taking into account the radial loss of matter via stellar wind, which depends on the mass of the star. The analysis includes new data on the clumpy structure of WR winds, which appreciably decreases the required mass-loss rates $\dot{M}_{\rm WR}$ for the WR stars. The masses $M_{\rm CO}^f$ lie in the range (1–2)$M_\odot$–(20–44)$M_\odot$ and have a continuous distribution. The masses of the relativistic objects M_x are 1–20$M_\odot$ and have a bimodal distribution: the mean masses for neutron stars and black holes are $1.35 \pm 0.15 M_\odot$ and 8–10$M_\odot$, respectively, with a gap from 2–4$M_\odot$ in which no neutron stars or black holes are observed in close binaries. The mean final CO-core mass is $\overline{M}_{\rm CO}^f$ = 7.4–10.3$M_\odot$, close to the mean mass for the black holes. This suggests that it is not only the mass of the progenitor that determines the nature of the relativistic object, but other parameters as well—rotation, magnetic field, etc. One SB1R Wolf–Rayet binary and 11 suspected WR + C binaries that may have low-mass companions (main-sequence or subgiant M–A stars) are identified; these could be the progenitors of low-mass X-ray binaries with neutron stars and black holes. © *2001 MAIK "Nauka/Interperiodica".*

1. INTRODUCTION

Population-I Wolf–Rayet (WR) stars are believed to be the exposed cores of massive stars that have lost their hydrogen envelopes as a result of either mass transfer in a close binary system (CBS) [1] or intense outflow in the form of a stellar wind [2]. The picture of a WR star as a hot, massive, non-degenerate, primarily helium object in a late stage of its evolution that will be followed by collapse and the formation of a relativistic object is based on observations over a wide range of wavelengths (from radio to X-rays), and also on studies of O–B and WR stars in many galaxies with various metallicities (see the proceedings of recent conferences on WR stars [3–5] and references therein). The masses, radii, and effective temperatures of the "cores" of WR stars derived from observations of CBSs support the idea that WR stars are the helium remnants of initially massive stars (see the review [6] and references therein).

One important result of recent years is the discovery of a clumpy structure in the stellar winds of WR stars [7–9]. There is reason to believe [10] that up to 80% of the wind material is contained in small (~0.1–1$R_\odot$), dense (with densities up to 30–100 times higher than that of the surrounding medium) gas clouds moving together with the intercloud medium of the wind [9]. Since, as first noted in [11], the intensity of the thermal radio and infrared emission depends on the square of the density, allowing for the clumpiness of WR winds when interpreting radio and IR observations (which are the main source of information about the stellar mass-loss rate $\dot{M}$) appreciably decreases the required values of $\dot{M}_{\rm WR}$ for WR stars compared to models with continuous winds. The application of clumpy-wind models in the interpretation of the emission-line spectra of WR stars implies a similar decrease in $\dot{M}_{\rm WR}$ compared to continuous-wind models [12–14].

There are a number of observational confirmations of these ideas. Long-term observations of the increase in the orbital period of the eclipsing binary V444 Cyg (WN5 + O6, $P \cong 4^{\rm d}.2$) [15, 16] yield a value of $\dot{M}_{\rm WR}$ based on dynamics, which does not depend on the structure of the WR wind (or its clumpiness), of 0.7×10^{-5} $M_\odot$/yr. This is a factor of three–four smaller than the $\dot{M}_{\rm WR}$ found for V444 Cyg based on radio observations [17]. It is natural to associate this difference with clumpiness of the WR wind.

Intensive observations of the optical linear polarizations of ten WR + O binary systems carried out by Moffat and collaborators (see, for example, [17–19]) have also been used to derive values of $\dot{M}_{\rm WR}$ for many WR stars, including the WN5 star in the V444 Cyg system.

1063-7729/01/4502-0120$21.00

Analysis of the polarization variations for V444 Cyg yields $\dot{M}_{WR} = 0.75 \times 10^{-5} M_\odot$/yr, in excellent agreement with the $\dot{M}_{WR}$ inferred from the increase in the orbital period of the system. Note that, since the optical linear polarization is determined by the first power of the electron density in the wind, the corresponding value of $\dot{M}_{WR}$ does not depend on the clumpiness of the WR wind. It is striking that the $\dot{M}_{WR}$ values indicated by polarization observations of WR + O systems are nearly an order of magnitude lower than the values derived from radio and IR observations (see, for example, [17, 20]). This difference can also be explained in a natural way as a consequence of clumpiness in the WR winds. Evidence supporting the existence of such a clumpy structure is summarized in [14].

It is currently believed (see, for example, the proceedings of the recent symposium on the structure of stellar winds [21]) that the mass-loss rates of WR stars derived from radio and IR fluxes are overestimated by factors of 2–4 [22]. For example, new data suggest that the influence of radial mass loss via the stellar wind on the decrease in the mass of the WR star over its core-evolution time is not as important as was thought earlier (see, for example, [23]). This enables a meaningful comparison between the masses of WR stars with carbon–oxygen cores and the masses of relativistic objects in CBSs. This was first pointed out in [24], where it was shown that, in contrast to the mass distributions for neutron stars and black holes, the mass distribution for WR stars was continuous rather than bimodal; crude estimates of the mean mass of the carbon–oxygen cores of WR stars were close to the mean mass of the black holes in X-ray binary systems.

Currently, masses of 23 WR stars in WR + O binary systems have been measured [25, 26], as well as those of 13 black holes and 17 neutron stars in binaries (see the review [27] and references therein). Polarization-variability analyses for WR + O binaries have yielded mass-loss rates that are independent of wind clumpiness for many WR stars. An empirical dependence $\dot{M}_{WR}$ on the mass of the WR star M_{WR} has been found:

$$\dot{M}_{WR} \sim M_{WR}^{\alpha}, \quad (1)$$

where α = 1–2 for WR stars [17–19], rather than 2.5–2.6, as was thought earlier based on theoretical computations [28, 29]. Relation (1) can be calibrated using the most trustworthy data that are independent of WR-wind clumpiness, derived from the increase in the orbital period of the eclipsing WR + O binary V444 Cyg [16]: $\dot{M}_{WR} = 7 \times 10^{-6} M_\odot$/yr for $M_{WR} \cong 10 M_\odot$.

The goal of the current paper is a quantitative comparison of the masses of WR stars, taking into account the mass decrease due to the outflowing stellar wind, and the masses of relativistic objects in CBSs. In addition, we conduct a search for WR binary systems containing low-mass A–M companions, which could be the progenitors of low-mass, transient X-ray binary systems—X-ray novae.

2. THE EVOLUTIONARY CONNECTION BETWEEN WR STARS AND RELATIVISTIC OBJECTS IN CLOSE BINARIES

The progenitors of relativistic objects can be not only WR stars, but also other objects, such as red and blue supergiants. For example, it is known that supernova 1987A in the Large Magellanic Cloud was the result of core collapse in a B3I supergiant (see, for example, [30]). However, it is appropriate to compare the masses of WR stars and those of relativistic objects in CBSs, since the more massive component will rapidly lose its hydrogen envelope due to mass transfer in the CBS. Therefore, in the vast majority of cases, the progenitors of the relativistic objects in CBSs are actually WR stars. Current evolutionary scenarios for CBSs (see, for example, [31–42]) predict the formation of relativistic objects from WR stars both in massive X-ray binaries (in which the companion is an O–B star) and in low-mass X-ray binaries (in which the companion is an A–M star).

In the case of quasi-steady-state, massive X-ray binaries such as Cyg X-1 and Cen X-3, it is believed that the initial mass ratio for the components of the O + O system is close to unity. In this case, the thermal relaxation times for the stars are comparable, and is it probable that the mass transfer is nearly conservative, so that the total mass and angular momentum of the system are approximately constant. The more massive component is the first to fill its Roche lobe and lose most of its hydrogen envelope via mass transfer, transforming it into a WR star. Further, the WR star collapses, leading to the formation of a relativistic object. The system is not disrupted, since it is the less massive star that collapses. Known WR + O binary systems (see the catalogs [25, 26]) can be viewed as the progenitors of massive X-ray binaries [31].

The role of mass loss by massive stars via stellar wind and the effects of collisions between the stellar winds in evolving CBSs have recently been discussed (see, for example, [17, 25, 41, 45]). Moffat [17] has proposed that the formation and evolution of WR stars in massive CBSs occurs exclusively due to radial mass loss by the massive star via its stellar wind, without the filling of its Roche lobe and outflow of matter through the inner Lagrange point. In this scenario, the binarity plays virtually no role in the formation of the WR star, which forms in accordance with the old scenario of Conti [2], which can be portrayed as follows in the framework of our current understanding (see, for example, [46, 47]): O $\longrightarrow$ Of $\longrightarrow$ WNL $\longrightarrow$ WN6–7 $\longrightarrow$ WNE $\longrightarrow$ WC $\longrightarrow$ SN if the initial mass of the O star is $M_i \geq 60 M_\odot$, and O $\longrightarrow$ LBV $\longleftrightarrow$ WN9–11 $\longrightarrow$ WN8 $\longrightarrow$ WNE $\longrightarrow$ WC $\longrightarrow$ SN if $40 M_\odot \leq M_i \leq 60 M_\odot$, where LBV denotes the short-lived, blue, variable super-

giant stage with intense mass loss (to 10^{-2} $M_\odot$/yr; see, for example, [25]).

According to [17, 48], the main arguments against mass transfer in massive CBSs are the following.

(1) There is no anti-correlation between the masses of the WR and O stars in WR + O systems.

(2) WR + O systems with large orbital periods include systems with elliptical orbits (see also [49]).

As shown in [50, 51], in semi-detached CBSs with subgiants in which there undoubtedly is mass transfer, there is likewise no anti-correlation between the masses of the subgiants and their companions. Moreover, for detached systems with subgiants, a statistically significant correlation is observed between the masses of the subgiants and of their companions. This is apparently due to the large scatter in the initial masses of the semi-detached systems and the fact that the initial mass ratios for the components of these CBSs are, on average, close to unity [50]. Therefore, the lack of an anti-correlation between the masses of the WR and O stars in WR + O systems cannot be considered an argument against the presence of mass transfer in massive CBSs.

The fact that ten WR + O binaries of the 40 such systems known have non-zero orbital eccentricities, likewise, cannot be taken as an argument against mass transfer without a special theoretical treatment of the problem. As noted by De Greve [52], in contrast to CBSs with subgiants, the time scale for mass transfer in massive CBSs is very brief, and can be shorter than the time required for orbital circularization via mass transfer. De Greve [52] and Vanbeveren [53] have argued that most OB + OB systems pass through a stage of mass transfer that leads to the formation of a WR star.

Such massive CBSs as RY Sct (which is probably a progenitor of a WR + O system [54]), SS433 (in which intensive secondary mass change is observed [55]), and Cyg X-3 (which passed through a common-envelope stage [56]) testify to the presence of mass transfer through the inner Lagrange point. In all these cases, the stellar winds of massive stars do not hinder the filling of their Roche lobes and outflow of matter to the other component through the inner Lagrange point. Thus, it appears that mass transfer through the inner Lagrange point is characteristic of massive CBSs.

In the case of low-mass X-ray binaries such as V404 Cyg, it is supposed that the initial mass ratios for the components of O + (A–M) binaries strongly differ from unity, and that mass transfer is non-conservative: the more massive O star is the first to fill its Roche lobe and intensively send matter through the inner Lagrange point, leading to the formation of a common envelope and to a loss of mass and angular momentum from the system. The size of the orbit is severely reduced, the O star's hydrogen envelope is lost, and the system can be transformed into a WR + (A–M) binary, containing a Wolf–Rayet star and a low-mass A–M companion. The subsequent collapse of the WR star results in the formation of a relativistic object bound with the A–M star, and further to a low-mass X-ray binary. Since the more massive WR star collapses in this case, the probability of disruption of the system is high. In certain specific cases of asymmetry of the supernova explosion or in the case of non-explosive collapse (which is possible for compact helium WR stars), the binary may remain gravitationally bound. Note that common-envelope models have also been applied to certain massive X-ray binaries, such as LMCX-3 [33]. Triple-system models in which the relativistic object is a progenitor of the WR stage are sometimes invoked to explain the formation of low-mass X-ray binaries [38, 41, 42].

Theory (see, for example, [38]) predicts that radio pulsars in binaries with elliptical orbits and comparatively high-mass companions (neutron stars, B stars, massive white dwarfs) also come about via the formation and subsequent collapse of a WR star. Radio pulsars in binaries with circular orbits and comparatively low-mass companions (low-mass white dwarfs) probably form without passing through a WR stage, via the collapse of a white dwarf whose mass has grown beyond the Chandrasekhar limit due to the accretion of matter from its companion, a non-degenerate low-mass star.

Thus, our current understanding is that all neutron stars and black holes in X-ray binaries and a large fraction of radio pulsars in binaries pass through a stage with a WR star, which subsequently collapses. Thus far, there is no direct evidence that the collapse of a WR star leads to a supernova explosion. There is only the hypothesis that type Ib and Ic supernovae and their remnants are associated with WR stars. Analysis of new observational data led Conti [57] to conclude that WR stars do not explode as supernovae, and probably undergo a non-explosive collapse at the end of their evolution. Recently, Izraellan *et al.* [58] detected enhanced abundances of silicon, carbon, and other heavy elements in the atmosphere of the optical F5IV star in the low-mass X-ray binary GRO J1655–40, which contains a black hole. Brandt *et al.* [59] found a large peculiar velocity for the center of mass of this X-ray binary system (–114 km/s), which may also provide evidence that the WR star exploded as a supernova. Brandt *et al.* [59] propose a two-stage collapse for this system: first, the core of the WR star collapses into a neutron star, after which it collapses into a black hole, due to the infall of matter from the supernova envelope onto the neutron star.

In this way, the latest data provide evidence that, at least for some WR stars, collapse at the end of their evolution leads to a supernova explosion (probably of type Ib or Ic).

3. INFLUENCE OF THE STELLAR WIND ON THE WR MASS AT THE END OF ITS EVOLUTION

Calculations of the evolution of WR stars taking into account mass loss via the stellar wind, which depends on the mass of the star, were first carried out by Langer

[28]. He derived a formula relating the mass-loss rate and mass of the $\dot{M}_{\rm WR}$ WR star:

$$\dot{M}_{\rm WR} = -(0.6\text{–}1.0)\times 10^{-7}(M_{\rm WR}/M_\odot)^{2.5}, \qquad (2)$$

where a coefficient of 0.6 corresponds to early subclasses (WNE) of WR stars, and a coefficient of 1.0 corresponds to WC and WO stars. For WR stars with mass $10M_\odot$, this formula yields a mass-loss rate (in absolute value) of $\dot{M}_{\rm WR} = (2\text{–}3)\times 10^{-5}\ M_\odot$/yr. This is a factor of three to four higher than the value $\dot{M}_{\rm WR} = 0.7\times 10^{-5}\ M_\odot$/yr obtained for the WN5 star ($\dot{M}_{\rm WR} = 9.3\text{–}10M_\odot$) in the eclipsing binary system V444 Cyg [16] based on the observed increase in its orbital period. This large discrepancy is probably due to the fact that the quantity $\dot{M}_{\rm WR}$ in Eq. (2) is systematically overestimated due to the lack of allowance for the clumpiness of the WR-star wind.

Because of the overestimated coefficient in Eq. (2) and the large power-law index ($\alpha = 2.5$), calculations of the evolution of stars with different masses taking into account mass loss via the stellar wind lead to the so-called convergence effect: virtually independent of the initial mass of the massive star, the mass of the corresponding helium star (WR star) at the end of its evolution is roughly constant and equal to several solar masses. For example, according to the computations of Woosley *et al.* [29], allowing for mass loss via the stellar wind using the relation $\dot{M}_{\rm WR} = -5\times 10^{-8}(M_{\rm WR}/M_\odot)^{2.6}$ results in the formation of comparatively low-mass helium stars with masses of about $4M_\odot$ at the end of their evolution from stars with initial masses from 35 to $85M_\odot$.

In light of the above, we will use the dependence of $\dot{M}_{\rm WR}$ on $M_{\rm WR}$ derived empirically from variations of the linear polarization of the optical emission of WR + O binaries [17–19]:

$$\dot{M}_{\rm WR} = kM^{\alpha}, \qquad (3)$$

where $\alpha = 1\text{–}2$ (the value $\alpha \cong 1$ is more appropriate for WR stars [17]) and the coefficient k can be determined from the condition that $\dot{M}_{\rm WR} = 7\times 10^{-6}\ M_\odot$/yr when $M_{\rm WR} = 10M_\odot$ (as is indicated by the increase in the orbital period of the V444 Cyg system and by linear-polarization measurements for WR + O systems). Since an accurate value for α is not known, we will consider the two limiting cases, $\alpha = 1$ and $\alpha = 2$.

Thus, using Eq. (3) and the adopted calibration, we have for the mass-loss rate of a WR star

$$\frac{dM_{\rm WR}}{dt} = -7\times 10^{-7}\frac{M_{\rm WR}}{M_\odot}\ M_\odot/{\rm yr}, \quad \alpha = 1, \qquad (4)$$

$$\frac{dM_{\rm WR}}{dt} = -7\times 10^{-8}\left(\frac{M_{\rm WR}}{M_\odot}\right)^2 M_\odot/{\rm yr}, \quad \alpha = 2. \qquad (5)$$

The differential equations (4) and (5) can readily be solved. As a result, we obtain the following formulas determining the mass of the WR star as a function of time in its evolution:

$$M_{\rm WR}(t) = M^i_{\rm WR}\exp(-7\times 10^7 t), \quad \alpha = 1, \qquad (6)$$

$$M_{\rm WR}(t) = \frac{M^i_{\rm WR}}{1 + 7\times 10^{-8}M^i_{\rm WR}t}, \quad \alpha = 2, \qquad (7)$$

where t is time in years and $M_{\rm WR}(t)$, $M^i_{\rm WR}$ is the mass of the WR star in solar units ($M^i_{\rm WR}$ is its initial mass). Using Eqs. (6) and (7) together with the method for evolutionary computations of models for WR stars over small time intervals Δt developed in [28], we can calculate the final masses of WR stars $M^f_{\rm WR}$ and the masses of their carbon-oxygen cores $M^f_{\rm CO}$ at the end of their evolution.

To achieve our more limited goal of comparing the masses of WR stars at the end of their evolution with the masses of relativistic objects, we will apply a simplified computation method. We will use the known approximation formula for the mass of the CO core of a WR star [60, 61]:

$$\frac{M_{\rm CO}}{M_\odot} \approx 0.45\left(\frac{M_{\rm He}}{M_\odot}\right)^{1.2}, \qquad (8)$$

and the theoretical "mass–luminosity" relation for WR stars: $L_{\rm WR} \sim M^{1.73}_{\rm WR}$ [62]. Then, the nuclear-evolution time T of a WR star can be estimated to be

$$T \sim \frac{M_{\rm CO}}{L_{\rm WR}} \sim M^{-0.53}_{\rm WR} \sim \frac{1}{\sqrt{M_{\rm WR}}}. \qquad (9)$$

Since the lifetime of a helium star is (see, for example, [33]) $T = 3\times 10^5$ yr for $M_{\rm He} = 25M_\odot$ and $T = 4.5\times 10^5$ yr for $M_{\rm He} = 15M_\odot$, we obtain the following estimate for the nuclear-evolution time for a WR star of a given mass:

$$T \approx \frac{1.74\times 10^6}{\sqrt{M/M_\odot}}{\rm yr}. \qquad (10)$$

Formulas (6), (7), and (10) enable approximate calculation of the mass of a WR star at the end of its evolution, while Eq. (8) can be used to estimate the mass of the corresponding CO core, which probably determines the mass of the progenitor of the relativistic object (see, for example, [23, 29, 36]).

As noted in [28], because of the decrease in the mass of the WR star due to the stellar wind, the characteristic time for its nuclear evolution T grows compared to the constant-mass case. Therefore, calculations using Eqs. (6), (7), and (10) require an iterative approach: for a specified initial mass $M^i_{\rm WR}$ for the WR star, we first

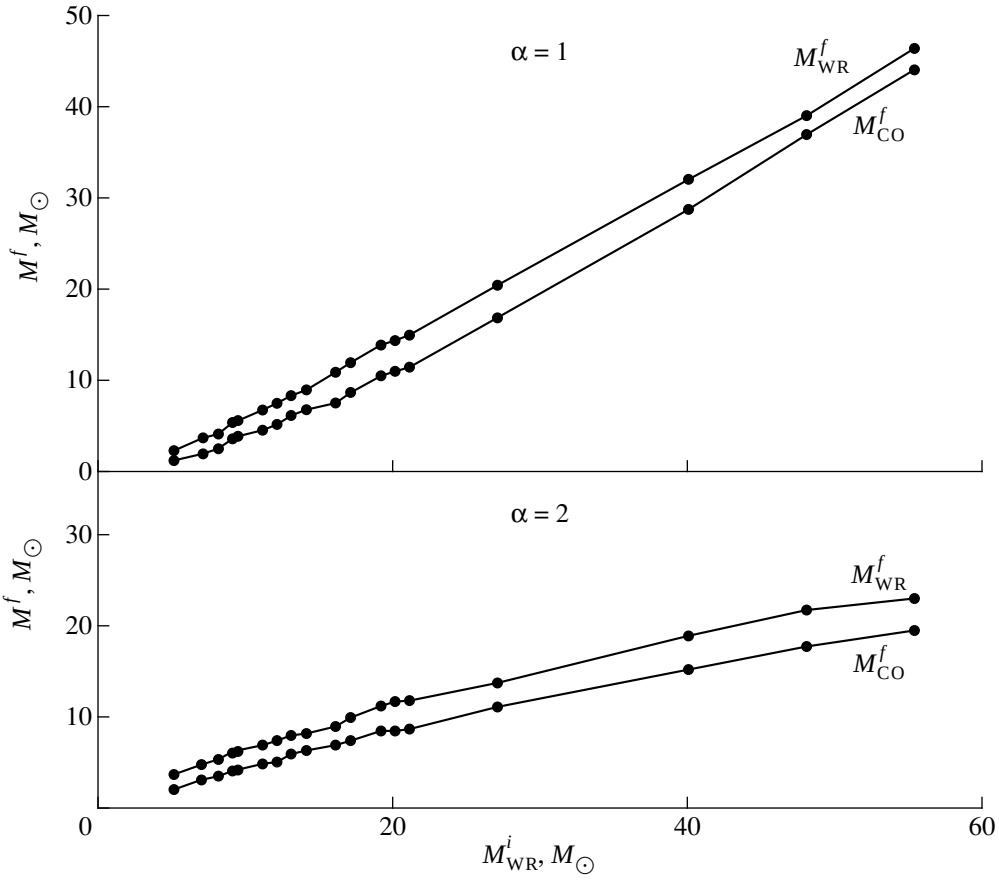

Fig. 1. Dependence of the final masses of WR stars M^f_{WR} and their CO cores M^f_{CO} on the initial masses M^i_{WR} for $\alpha = 1$ (upper) and $\alpha = 2$ (lower).

find the corresponding nuclear-evolution time T_1 from Eq. (10), then use this with Eqs. (6) and (7) to determine a first approximation for the mass $M^f_{WR}(T_1)$. Further, using the values $M^f_{WR}(T_1)$ and T_2, we can determine a second approximation for the mass M^i_{WR} using (6) and (7), etc. Computations have shown that this iterative process converges rapidly, and it is possible to obtain final values for the WR-star mass at the end of its evolution T_2 after three or four iterations, after which the final mass $M^f_{WR}(T_2)$ M^f_{WR} for the CO core M^f_{CO} can be determined using Eq. (8). The nuclear-evolution times T, computed in this way, increase when mass loss is taken into account. The corresponding growths in $\Delta T/T_1$ for $M^i_{WR} = 5$, 10, 20, 40, and $60M_\odot$ are 46, 27, 18, 11, and 10% for $\alpha = 1$ and 14, 22, 30, 43, and 59% for $\alpha = 2$. The final mass M^f_{WR} decreases compared to the first approximation $M^f_{WR}(T_1)$. For $M^i_{WR} = 5$, 10, 20, 40, and $60M_\odot$, these decreases in $\Delta M_{WR}/M^f_{WR}(T_1)$ are equal to 21, 10, 5, 2, and 1% for $\alpha = 1$ and 3, 6, 9, 16, and 22% or $\alpha = 2$.

The computation results are presented in Fig. 1 and Table 1, which give values of M^f_{WR} and M^f_{CO} or $\alpha = 1$ and $\alpha = 2$ for 23 WR stars in WR + O binary systems with measured masses, which we adopted for the initial masses of M^i_{WR}. We can see that, in contrast to the results of [23, 29], we observe no convergence effect. The masses of the CO cores M^f_{CO} monotonically grow with the initial mass of the WR star M^i_{WR}: as M^i_{WR} is increased from 5 to $60M_\odot$, M^f_{CO} increases from 1.2 to $49.6M_\odot$ for $\alpha = 1$ and from 2.2 to $20.7M_\odot$ for $\alpha = 2$.

The absence of the convergence of the masses of WR stars at the end of their evolution to a single modest value indicates that the distribution of observed WR-star masses M^i_{WR} and the distributions of the corresponding values of M^f_{WR} and M^f_{CO} (Figs. 2 and 3) are qualitatively similar. This enables the correct compari-

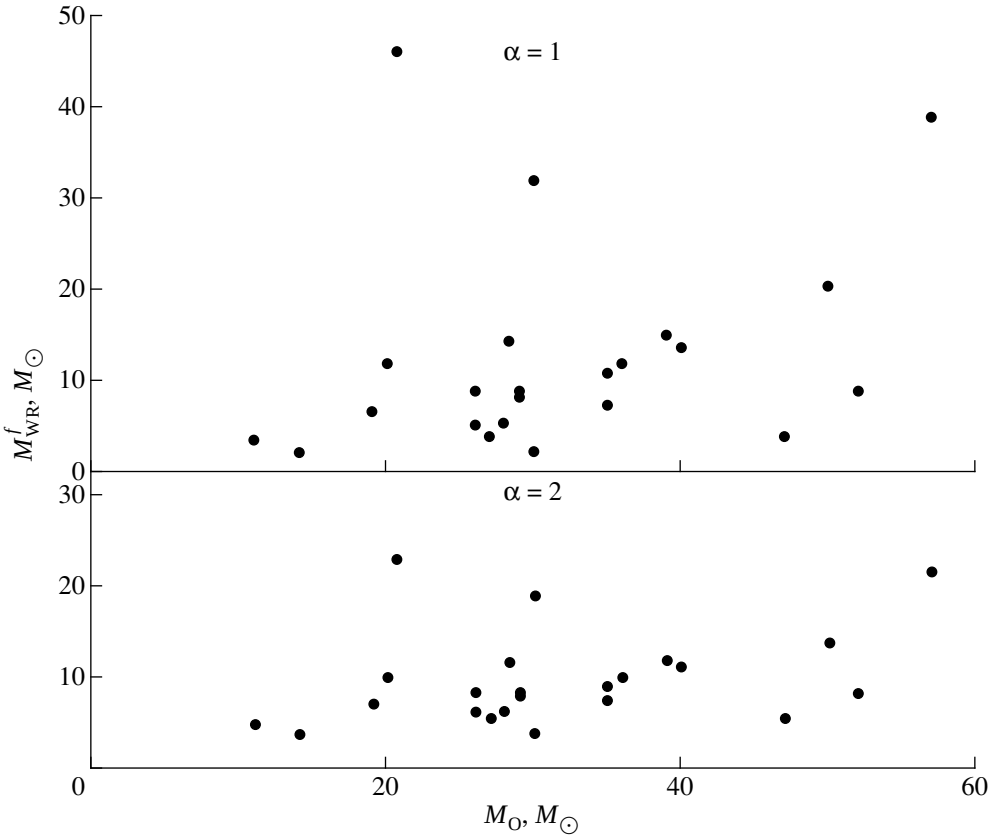

Fig. 2. Dependence of the final masses M^f_{WR} of WR stars on the masses of the O components in WR + O binaries for $\alpha = 1$ (upper) and $\alpha = 2$ (lower).

son of these distributions with the distribution of the masses of relativistic objects in CBSs.

4. CHARACTERISTICS OF WR STARS IN CLOSE BINARY SYSTEMS

There are 201 known WR stars in the Galaxy, 114 in the Large Magellanic Cloud (LMC), nine in the Small Magellanic Cloud (SMC), about 100 in M33, about 50 in M31, four in IC 10, four in NGC 6822, and one in IC 1613 [46]. According to [46], of the 201 known WR stars in the Galaxy, 112 have spectral class WN, 79 have class WC, three have class WO, and seven have the combined class WN/WC (spectra containing emission lines of nitrogen and carbon with roughly equal intensities).

The fraction of binaries among WR stars in the Galaxy (mean metallicity $z \cong 0.02$) estimated in the most trustworthy way (based on the periodicity of the radial-velocity and brightness variability) is 42%. The fraction of binaries for the LMC (metallicity $z \cong 0.006$) is 42% of all WNL stars (late subtypes) and ~13% of WC/WO stars [17, 63]. The fraction of binaries for the SMC (metallicity $z \cong 0.002$) is ~62% for all WR subtypes [17] and apparently approaches 100% [46]. According to [17], the difference in the fraction of binaries among WR stars in the LMC and SMC cannot be considered significant in view of the small number of WR stars in the SMC. Note that these estimates for the fractions of binaries among WR stars should be considered lower limits, since orbital variations of the radial velocities and brightnesses of the components of binary systems will be difficult to detect in the case of small orbital inclinations $i \ll 90°$. A method for detecting binaries among WR stars based on their enhanced X-ray emission due to the colliding stellar winds of the components, whose efficiency does not depend on i, is proposed in [64]. This method has enabled the discovery of a number of new binaries with WR stars [65, 66].

WR + O binaries in the Galaxy are distributed close to the Galactic plane, with a mean height $|z| = 60$ pc. In the Galactic plane, there is an increase in the fraction of binary WR stars with increasing Galactocentric distance. The spectral types of WR stars in WR + O binaries are from WN3–7 to WC4–8, and even WO4. The O stars in WR + O binaries are massive, hot stars of spectral types O4–9 and luminosity classes from V to I. The orbital periods of known WR + O binaries lie from $1^d.6$

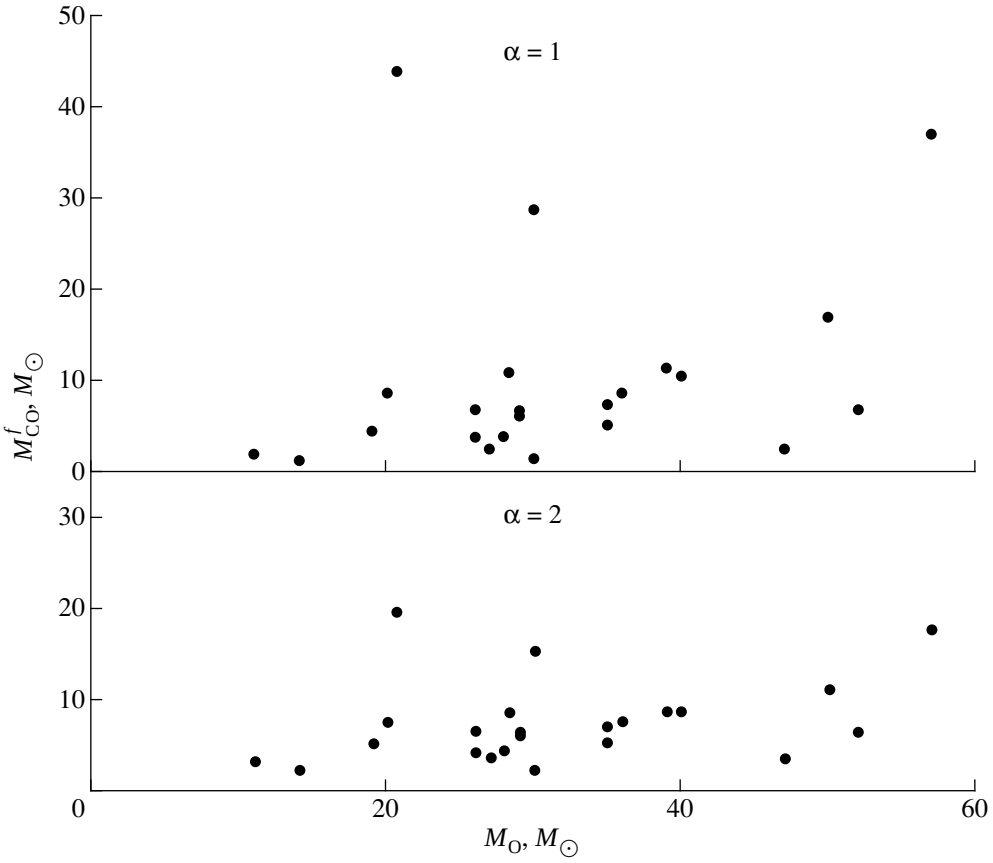

Fig. 3. Dependence of the final masses M^f_{CO} for the carbon–oxygen cores of WR stars on the masses of the O components in WR + O systems for $\alpha = 1$ (upper) and $\alpha = 2$ (lower).

(CQ Cep) to 2886^d (HD 193793) and even 5680^d (HD 192641). The orbital eccentricities for WR + O binaries with periods $P \geq 70^d$ differ from zero, $e = 0.1$–0.8. All systems with periods $P \leq 14^d$ have circular orbits ($e = 0$). In the interval $14^d < P < 70^d$, both circular and elliptical orbits are found ($e \cong 0$–0.5).

A reliable estimation of the masses of WR stars in binaries requires knowledge of the orbital inclinations i along with the radial-velocity curves. Earlier, values of i were known only for a small number of eclipsing WR binaries: V444 Cyg, CQ Cep, CX Cep, CV Ser, and HD 211853. Recently, thanks to progress in polarimetric studies, orbital inclinations have been estimated for roughly two dozen WR spectral binary systems (see the studies of Moffat [17–19, 67]). At present, the masses of 23 WR stars in WR + O binaries have been measured [25, 26]. Table 2 presents data on the masses of the WR stars and the orbital parameters for 23 WR + O systems taken from [25] together with the latest results of spectroscopic studies.

The uncertainty in the WR masses is determined by the accuracy of the corresponding spectroscopic observations, the correctness with which the radial-velocity curves are interpreted (due to the large size of the emission-line formation region and the effects of the colliding stellar winds, the photometric center of a line may not accurately reflect the orbital motion of the WR star), and the accuracy of the orbital inclination i (which is ~1° for analyses of eclipses and 5°–10° for polarimetric studies). In the best cases (e.g. the eclipsing system V444 Cyg), the accuracy in the mass reaches 10%, but in some cases, the masses of a particular WR star in a binary determined by different authors can differ by factors of 1.5–2. For example, the mass of the massive WN7 star in the HD 92740 system determined in [68] is $\sim 80 M_\odot$, while the more recent data of [69] yield a mass of $55.3 M_\odot$. In some cases, different half-amplitudes for the radial-velocity curves for the WR star in a WR + O binary are derived from observations of emission lines for different ions. For example, the mass ratio $q = M_{WR}/M_O$ in the WC5 + O7 binary HD 63099 varies from $q = 0.28$ for a C III–IV emission line to $q = 0.63$ for an O VI line [70]. It is natural to suppose that the most trustworthy information about the masses of WR stars is derived from analyses of radial-velocity curves measured from emission lines with high ionization potentials.

Table 1. Final masses for WR stars and their CO cores, including mass loss for $\alpha = 1$ and $\alpha = 2$

(WR + O)-system	$M_{WR}, M_\odot$	$M_O, M_\odot$	$\alpha = 1$		$\alpha = 2$	
			$M^f_{WR}, M_\odot$	$M^f_{CO}, M_\odot$	$M^f_{WR}, M_\odot$	$M^f_{CO}, M_\odot$
HD 63099	7	11	3.7	2	4.8	3.2
γ^2 Vel	21	39	15	11.4	11.8	8.7
HD 90657	17	36	12	8.7	10	7.5
HD 92740	55.3	20.6	46.2	44	23	19.5
HD 94305	19	40	13.8	10.5	11.2	8.6
HD 94546	9	26	5.3	3.7	6.2	4.2
HD 97152	11	19	6.8	4.5	7	5
HDE 311884	48	57	39	37	21.7	17.7
HD 152270	5	14	2.3	1.2	3.8	2.2
CV Ser	14	29	9	6.8	8.3	6.5
HD 186943	16	35	11	7.5	9	7
HD 190918	13	29	8.3	6.2	8	6.1
V444 Cyg	9.3	27.9	5.5	3.8	6.3	4.3
HD 193793	27:	50:	20.5	17	13.8	11.2
CX Cep	20	28.3	14.4	11	11.7	8.6
HD 211853	14:	26:	9	6.8	8.3	6.5
CO Cep	17	20	12	8.7	10	7.5
B22	12:	35:	7.5	5.2	7.5	5.2
B32	5	30	2.3	1.2	3.8	2.2
AB8	14	52	9	6.8	8.3	6.5
HD 5980	8:	27:	4	2.5	5.5	3.6
AB6	8	47	4	2.5	5.5	3.6
HD 193928	40	30	32	28.8	18.9	15.3
Mean	17.8	31.7	12.7	10.3	9.8	7.4

Detailed CCD spectroscopy of a number of WR + O binaries and analyses of emission- and absorption-line profiles and the effects of colliding stellar winds have been carried out by Marchenko *et al.* [71, 72] and Lewis *et al.* [73]. A theory for the formation of emission lines in WR stars in WR + O binaries taking into account the effects of the colliding stellar winds was proposed in [74]. The further development of this theory enables verification of the reliability of the mass determinations for WR stars in WR + O binaries. The influence of the closeness of the components should weaken as the orbital period of the binary increases. Note in this connection that no correlation between the component mass ratio q and the orbital period of WR + O binaries has been observed [14]. This suggests that the WR-star masses in Table 2 are not strongly distorted by the effects of the colliding stellar winds, additional ionization of the WR-star wind by ultraviolet radiation from the wind-collision zone and from the O star, or other effects associated with the closeness of the components.

The catalog [25] also presents data for 15 SB1 Wolf–Rayet systems, which are spectroscopic binaries with visible lines for a single WR component in their spectra, and for 17 so-called WR + C binaries, which are thought to contain a relativistic companion (the existence of WR + C systems is predicted by the theory of the evolution of CBSs with mass transfer [31, 32]). Since the absorption lines expected for an O component are not visible in the spectra of SB1 and WR + C Wolf–Rayet binaries, in the case of a low mass function, this suggests the presence in these systems of low-mass A–M companions. Therefore, we should pay special attention to SB1 and WR + C Wolf–Rayet binaries when searching for the progenitors of low-mass X-ray binaries [24]. Tables 3 and 4 present data on the 15 SB1 systems and 17 proposed WR + C taken from [25].

The data in Table 2 indicate that the mean mass ratio for the components in known WR + O binaries is $q = M_{WR}/M_O = 0.53$, with q lying in the range from 0.17 to 2.7. The q values in WR + O systems depend on the spectral subtype of the WR star: q monotonically

Table 2. Masses and orbital characteristics of WR and O stars in WR + O systems

(WR + O)-system	M_{WR}, $M_\odot$	M_O, $M_\odot$	Sp	P	e	i	References
HD 63099	$7M_\odot$	$11M_\odot$	WC5 + O7	$14^d.305$	0	64°	25, 70
γ^2 Vel	21	39	WC8 + O9I	78.5002	0.40	70	25
HD 90657	17	36	WN4 + O5	8.255	0	57	25
HD 92740	55.3	20.6	WN7 + O6.5–8.5	80.34	0.56	70	25, 68, 69
HD 94305	19	40	WC6 + O6–8V	18.82	0	70:	25
HD 94546	9	26	WN4 + O7	4.9	0	74	25
HD 97152	11	19	WC7 + O7V	7.886	0	43	25
HDE 311884	48	57	WN6 + O5V	6.34	0	70	25
HD 152270	5	14	WC7 + O5	8.893	0	45	25
CV Ser	14	29	WC8 + O8–9V–III	29.707	0	67	25
HD 186943	16	35	WN4 + O9V	9.5550	0	56	25
HD 190918	13	29	WN5 + O9.5I	112.8	0.48	15	25
V444 Cyg	9.3	27.9	WN5 + O6	4.212424	0	78.7	25, 71
HD 193793	27:	50:	WC7 + O4V	2900	0.84	44:	25
CX Cep	20	28.3	WN5 + O5V	2.1267	0	74	25, 73
HD 211853	14:	26:	WN6 + O + ?	6.6884	0	78	25
CQ Cep	17	20	WN6–7 + O9II–Ib	1.641246	0	78	25, 72
B22	12:	35:	WC6 + O5–6V–III:	14.926	0.17	71:	25
B32	5	30	WC4 + O6V–III:	1.91674	0	29	25
AB8	14	52	WO4 + O4V	16.644	0.19	41	25
HD 5980	8:	27:	WN4 + O7I	19.266	0.49	89	25
AB6	8	47	WN3 + O7	6.681	0	68	25
HD 193928	40	30	WN6 + O	21.64	0.02	68	96

When the catalog of close binary systems in late stages of evolution [25] is cited, see also references therein.

Table 3. Parameters of SB1 Wolf–Rayet binaries [25]

Name	Note to name	Spectrum	P	$f_{WR}(M)$, $M_\odot$	e	i
HD 62910	–	WN6 + WC4	$85^d.37$	0.20	0.4	–
HD 93131	–	WN7 + abs.	–	–	–	–
HD 93162	–	WN7 + abs.	–	–	–	0°
HD 151932	–	WN7 + ?	22.7	–	–	–
HD 192641	V1679 Cyg	WN7 + abs.	–	–	–	–
HD 193077	–	WN7 + abs. + ?	1538.0	4.13	0.3	–
HD 193928	–	WN6 + ?	21.64	4.9	0	–
AS422	–	WN + WC + ?	22.0	7.7:	0	–
B26	in LMC	WN7 + ?	1.9075	2.4	0	68
B65	in LMC	WN7 + ?	3.0032	4.2	0	–
B72	in LMC	WN6 + B1Ia	4.3092	3.8	0	–
B82	in LMC	WN6 + O5	4.377	0.02	0	–
B86	in LMC	WNL/Of	52.7:	1.6:	0	–
B87*	in LMC	WN6 + ?	2.7596	0.10	0	–
B90	in LMC	WN7 + ?	25.17:	1.4:	0	75

* This SB1 Wolf–Rayet binary can be considered a progenitor of a low-mass X-ray binary with an A–M companion.

decreases in the transition from late to early WR subtypes. For example, for WN stars, q decreases from 2.7 for WN7 stars to 0.17 for WN3 stars. For WC stars, q decreases from 0.5 for WC8 stars to ~0.2 for hot (WC4–WO4) stars. These dependences were proposed by Moffat [17] based on the evolutionary scenario for massive CBSs without mass transfer discussed above. Since there is little doubt that there is mass transfer in massive CBSs, we must consider other possible explanations for the dependences of q on WR subtype. At the moment, this question remains open.

The mass distribution of the WR stars (Table 2) appears not to be Gaussian (Fig. 4). Allowing for the appreciable uncertainties in the masses of many of the WR stars in Table 2, we calculate the mean masses for WR stars of various types. The mean mass for all the WR stars in Table 2 (23 WR stars in WR + O binaries) is $\overline{M}_{\mathrm{WN+WC+WO}} = 17.8M_\odot$ (given the large uncertainties in the errors for many of the masses, we limited our consideration to an arithmetic unweighted mean). The masses of individual WR stars lie within very broad limits, from $5M_\odot$ (HD 152270, WC7 and B32, WC4) to $48M_\odot$ (HDE 331884, WN6), and even $55.3M_\odot$ (HD 92740, WN7). The mean mass for the 13 WN stars is $\overline{M}_{\mathrm{WN}} = 21.1M_\odot$. The mean mass for the nine WC stars is $\overline{M}_{\mathrm{WC}} = 13.4M_\odot$. The mass of the WO4 star is $M_{\mathrm{WO4}} = 14M_\odot$, and is close to $\overline{M}_{\mathrm{WC}}$.

The difference in the mean masses for the WN and WC stars is due to the three most massive WN stars in the sample of 13: the WN7–WN6 stars in the HD 92740 ($M_{\mathrm{WN7}} = 55.3M_\odot$), HDE 311884 ($M_{\mathrm{WN6}} = 48M_\odot$), and HD 193928 ($M_{\mathrm{WN6}} = 40M_\odot$) systems. The mean mass for the remaining WN7–WN6 stars without these three

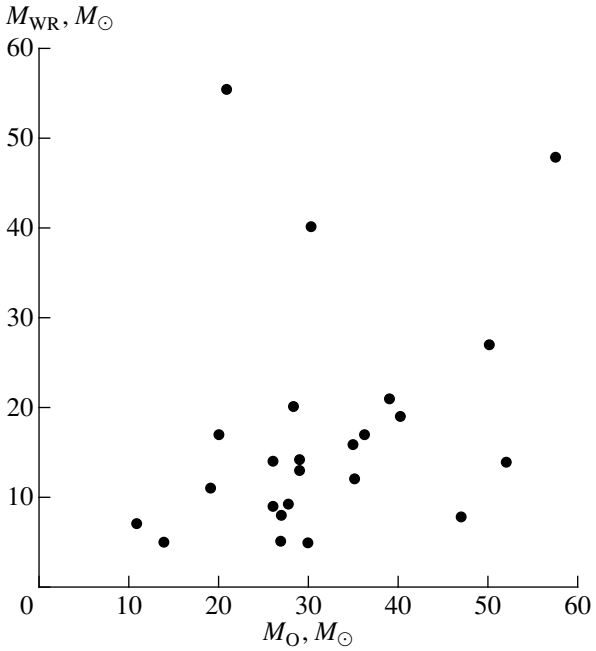

Fig. 4. Dependence of the masses of WR stars in WR + O binaries on the masses of the O components.

Table 4. Parameters of proposed WR + C binaries [25]

Name	Note to name	Spectrum	P	K_{WR}, km/s	$f_{\mathrm{WR}}(M)$, $M_\leqslant$	z, pc	d, kpc
HD 9974	–	WN7 + abs. + ?	$46\overset{\mathrm{d}}{.}85$	33	0.200	–581	8.05
HD 16523*	–	WC5	2.4096	35	0.012	–229	4.41
HD 38268*	–	WN6 + (OB) + ?	4.377	43	0.036	–	53
HD 50896*	EZ CMa	WN5	3.7650	40	0.025	–356	2.03
CD-45°4482	–	WN7	23.9	130	5.500	–282	8.20
HD 86161	V396 Car	WN8	10.73	6	0.00025	–181	4.08
HD 96548*	V385 Car	WN8	4.762	10	0.0005	–342	4.07
HD 97950*	–	WN6 + abs. + ?	3.8	54	0.060	–68	7.50
HD 143414	–	WN6	7.690	21	0.0074	–744	5.62
HD 164270*	V4072 Sgr	WC9	1.75404	20	0.0015	–228	2.67
HD 177230	–	WN8	237:	22	0.0026	–824	9.95
WR 124*	QR Sge	WN8	2.73	13	0.0005	264	4.58
HD 187282*	QR Sge	WN4	3.83	30	0.011	366	5.54
HD 191765	V1769 Cyg	WN6	7.44	30	0.020	44	1.63
HD 192163*	V1770 Cyg	WN6	4.57	20	0.004	53	1.25
HD 193077*	–	WN5 + abs. + ?	2.3238	16	0.001	29	1.50
HD 197406*	V1696 Cyg	WN7	4.31364	80	0.280	799	7.09

* These WR + C binaries can be considered a progenitor of low-mass X-ray binaries with A–M companions.

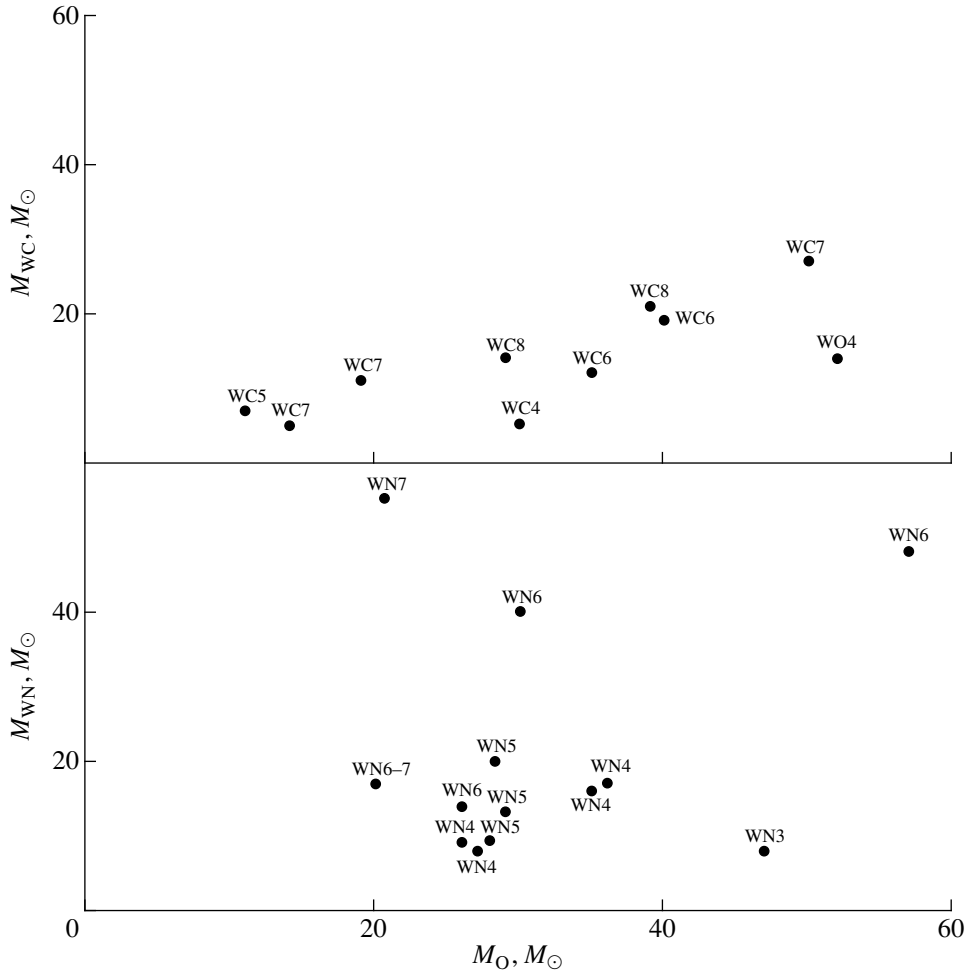

Fig. 5. Dependence of the masses of WC (upper) and WN (lower) stars on the masses of the O components in WR + O binaries.

is $13.1M_\odot$, which is close to the mean mass for the WC stars and the WO4 star.

On average, the masses of the WR stars grow with the mass ratio q for the components in the WR + O binaries.

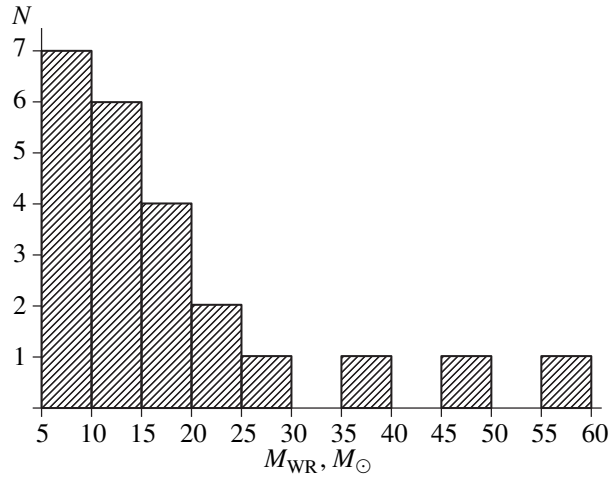

Fig. 6. Mass distribution for WR stars in WR + O systems.

At the same time, there is no correlation between the masses of the O stars in the WR + O systems and q. The masses of the O components lie in the range from $11M_\odot$ to $57M_\odot$, with an average mass $\bar{M}_\odot = 31.7M_\odot$. The average of the total masses for the WN + O binaries is $52.7M_\odot$, while that for the NC + O binaries is $43.1M_\odot$.

As we can see from the mass distributions for the 23 WR stars and for the WN and WC/WO stars (Figs. 4, 5), there is a correlation between the masses of the WR and O stars in WR + O binaries. This correlation can be traced most clearly for WC/WO stars: the mass of the WR star grows with the mass of the O component. As noted above, this correlation probably reflects the large scatter in the initial masses for the O + O binaries that are the progenitors of WR + O systems, and the fact that the mean initial mass ratio in these O + O binaries is close to unity [50, 51].

We can see in Fig. 6 that the observed mass distribution for all subtypes of WR stars (WN, WC, and WO) has a maximum near $5–10M_\odot$ and monotonically falls off toward higher masses, though it has an extended tail

Table 5. Parameters of binaries with black holes [27]

System	Spectrum of the optical star	P	$f_V(M), M_\odot$	$M_x, M_\odot$	$M_V, M_\odot$	V_{pec}, km/s	Type of source
Cyg X-1 (V 1357 Cyg)	O9.7Iab	$5^d.6$	0.24 ± 0.01	16 ± 5	33 ± 9	2.4 ± 1.2	Constant
LMC X-3	B3III–V	1.7	2.3 ± 0.3	9 ± 2	6 ± 2	–	Constant
LMC X-1	O(7–9)III	4.2	0.14 ± 0.05	7 ± 3	22 ± 4	–	Constant
Cyg X-3	WN 3–7	0.2	~ 2.3	7–40	5–20	–	Constant
A0 620-00 (V 616 Mon)	K4V	0.3	2.91 ± 0.08	10 ± 5	0.6 ± 0.1	-15 ± 5	Transient
GS 2023 + 338 (V 404 Cyg)	K0 IV	6.5	6.08 ± 0.06	12 ± 2	0.7 ± 0.1	8.5 ± 2.2	Transient
GRS 1124-68 (GU Mus)	K2 V	0.4	3.01 ± 0.15	$6(+5, -2)$	0.8 ± 0.1	26 ± 5	Transient
GS 2000 + 25 (QZVul)	K5 V	0.3	4.97 ± 0.10	10 ± 4	0.5 ± 0.1	–	Transient
GRO J0422 + 32 (V 518 Per)	M2 V	0.2	1.13 ± 0.09	10 ± 5	0.4 ± 0.1	–	Transient
GRO J1655-40 (XN Sco 1994)	F5 IV	2.6	2.73 ± 0.09	7 ± 1	2.5 ± 0.8	-114 ± 19	Transient
H 1705-250 (V2107 Oph)	K5 V	0.5	4.86 ± 0.13	6 ± 1	0.4 ± 0.1	38 ± 20	Transient
4U 1543-47 (HL Lup)	A2 V	1.1	0.22 ± 0.02	5 ± 2.5	~2.5	–	Transient
GRS 1009-45 (MM Vel)	(K6–M0)V	0.3	3.17 ± 0.12	3.6–4.7	0.5–0.7	–	Transient

Peculiar radial velocities for the centers of mass of the binary systems V_{pec} are taken from Brandt *et al.* [59].

in the interval $30–60M_\odot$ due to the three most massive WN7–WN6 stars in the sample. The relatively small number of WR stars with known masses hinders a detailed separate analysis of the mass distributions for WN and WC stars (Figs. 5, 7). If we consider only the masses of all the WR stars together (WN, WC, and WO), we conclude that this distribution is continuous between $5M_\odot$ and $55M_\odot$, with a concentration of masses near $\sim 10M_\odot$.

5. CHARACTERISTICS OF RELATIVISTIC OBJECTS IN BINARY SYSTEMS

Currently, the masses of 30 relativistic objects in binary systems have been measured. Among these, 13 are black holes (four in massive and four in low-mass X-ray binaries) and 17 are neutron stars (six X-ray pulsars in massive X-ray binaries and 11 radio pulsars in binaries with neutron-star, white-dwarf, and B-star companions). It follows from the discussion above that there are weighty arguments that all 13 black holes, the six X-ray pulsars, and a large fraction of the radio pulsars formed as a result of core collapse in WR stars that formed from the initially more massive stars in close binary systems undergoing mass transfer.

Recent data on black holes in binary systems have been presented in a number of reviews [27, 75–77]. Table 5 presents the characteristics of X-ray binaries with black holes taken from [27]. Data on the masses of X-ray and radio pulsars are published in [23, 78]. Figure 8 shows the masses of neutron stars and black holes in binary systems as a function of the component masses. We can see that, in contrast to WR binaries, there is no correlation between the masses of relativistic objects and the masses of their companions in close binary systems. Black holes in binary systems can have both massive (O–B or WR) and low-mass (A–M) companions. The same is true of neutron stars in binaries. An evolutionary consideration of the origin of black holes in binaries is presented in [59, 76, 79].

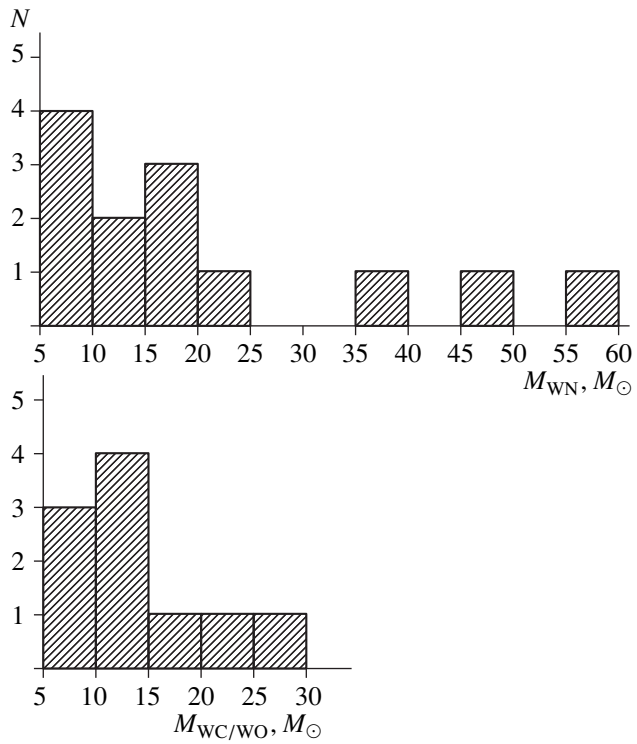

Fig. 7. Mass distribution for WN (upper) and WC (lower) stars in WR + O systems.

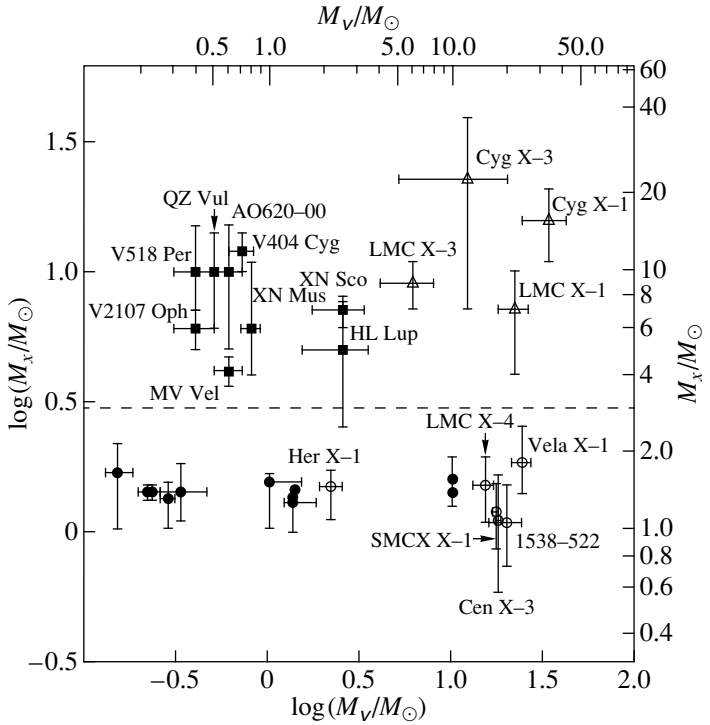

Fig. 8. Dependence of the masses M_x of neutron stars (circles) and black holes (triangles and squares) on the masses of the M_V companions in close binary systems. The dark circles correspond to radio pulsars and the dark squares to black holes in X-ray novae.

As noted in [24, 80], the mass distribution for relativistic objects is bimodal (Fig. 8): there are two clearly expressed maxima, corresponding to neutron stars and black holes, without a continuous mass transition between them. The masses of the neutron stars lie in the narrow interval from 1 to $2M_\odot$. The mean mass of radio pulsars in binaries is $1.35 \pm 0.04M_\odot$ [78], and there is no significant difference between the masses of radio pulsars formed from WR stars and from white dwarfs in CBSs. The mean mass of all known pulsars (X-ray and radio) in binaries is $1.35 \pm 0.15M_\odot$ [81]. It is striking that no radio or X-ray pulsars are observed to have masses in the range $2–3M_\odot$.

The masses of the 13 black holes are concentrated toward the values $8–10M_\odot$, and lie in the range $4–16M_\odot$ (Table 5 and Fig. 8). The mean mass of all 13 black holes is $9.6M_\odot$. If we do not include the Cyg X-3 system, which has the least promising black hole candidate, the mean mass of the remaining 12 black holes is $8.5M_\odot$. We limit our analysis to arithmetic averages, since the errors in the black-hole masses, and accordingly the appropriate weights for the mass estimates, are known very uncertainly. The examination of Table 5 and Fig. 8 enables us to draw a more cautious conclusion than in the neutron-star case: it appears that no black holes with masses less than $4M_\odot$ are observed. Further accumulation of observational information about black holes in binary systems and the application of new methods for estimating the masses of black holes based on analyses of orbital variations in absorption-line profiles in the spectra of the optical stars in X-ray binaries [82, 83] will enable the verification of this tentative conclusion.

Thus, the mass distribution for relativistic objects in close binary systems is bimodal: the mean masses for neutron stars and black holes are $1.35 \pm 0.15M_\odot$ and $8–10M_\odot$; no neutron stars or black holes in close binary systems are observed to have masses in the range from 2 to $4M_\odot$. As emphasized in [80], the conclusion that the mass distribution for relativistic objects is bimodal does not depend on observational selection effects. It was stressed in [27, 84] that it is difficult to explain large black-hole masses as a consequence of mass increase via accretion from the companion in the X-ray binary system. The black-holes must be massive right from the onset, from the moment of their birth.

6. COMPARISON OF THE OBSERVED DISTRIBUTIONS OF THE FINAL MASSES OF WOLF–RAYET CO CORES AND OF RELATIVISTIC OBJECTS

Let us consider the influence of observational selection effects on the distribution of the final masses $M_{\rm CO}^f$ of the CO cores of WR stars and of relativistic objects. WR stars have intense and broad line emission, which can be used to construct the radial-velocity curves for the WR stars in WR + O systems for a wide range of

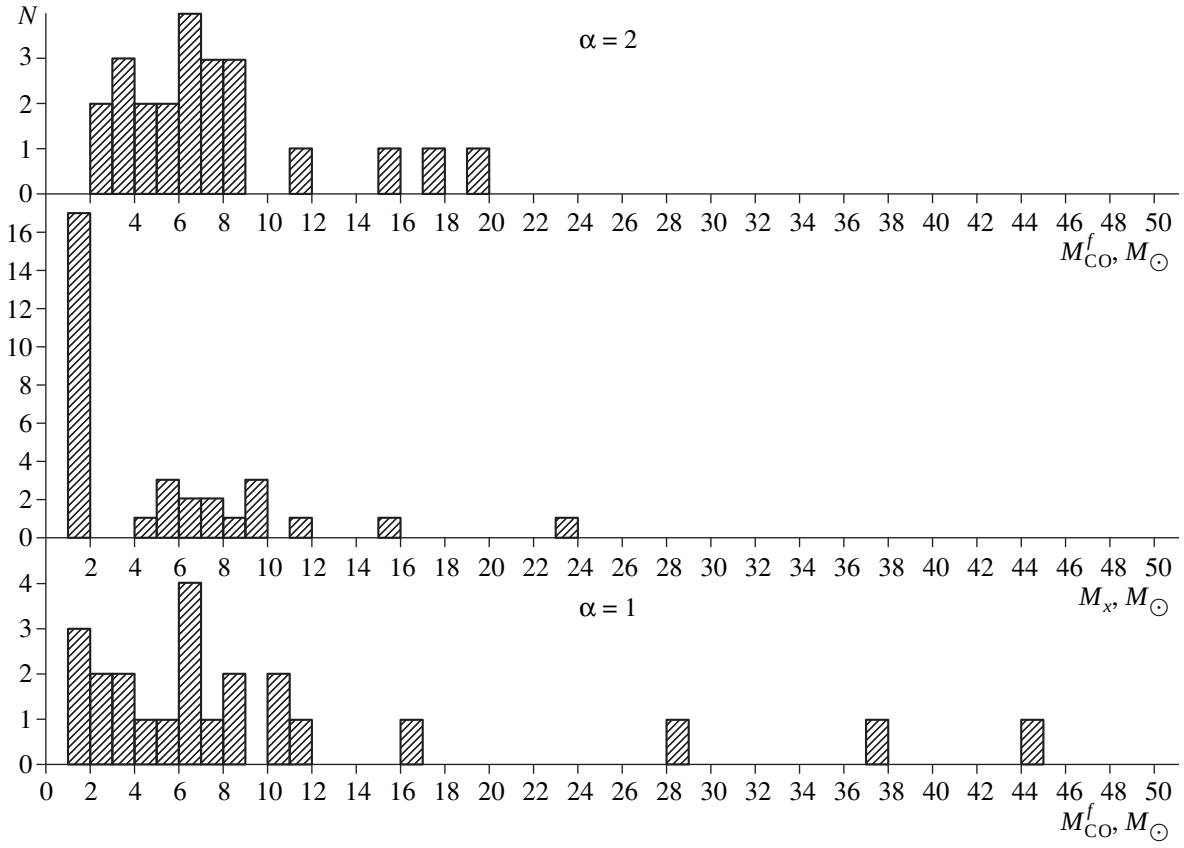

Fig. 9. Distribution of the final mass of the carbon-oxygen cores M^f_{CO} of WR stars for α = 1 (upper) and α = 2 (lower) and of the mass M_x for relativistic objects (middle) in close binary systems. The distribution of M^f_{CO} is continuous, while the distribution of M_x is bimodal, with a gap at masses $M_x = 2–4M_\odot$.

masses and luminosities for the WR and O components, as long as the orbital inclination i is not too small. At the same time, the radial-velocity curve can be reliable constructed from the narrow absorption lines of the O component only when the luminosity, and accordingly the mass, of the WR star is not too large compared to that of the O component. Since WR stars, as helium objects, are appreciably overluminous for their masses, it is difficult to distinguish and measure weak absorption lines of the O component against the background of the massive and bright WR star. Therefore, observational selection effects are weak for low- and moderate-mass WR stars with $M_{WR} = 5–20M_\odot$ (corresponding to final CO-core masses $M^f_{CO} = (1–2)–(9–11)M_\odot$, Fig. 1), and can be substantial for more massive WR stars with $M_{WR} > 20M_\odot$ (with $M^f_{CO} > 9–11M_\odot$). Thus, we expect a dip in the number of WR stars with measured masses in the range $M_{WR} > 20M_\odot$. Since quantitative estimation of the influence of observational selection effects is hindered by the need to take many factors into account, we restrict our treatment to such qualitative arguments. It is important that the influence of selection effects on the distribution of M^f_{CO} is probably small in the mass interval of interest to us, $M_{WR} = 5–20M_\odot$ and $M^f_{CO} = (1–2)–(9–11)M_\odot$.

As shown in [80], the influence of selection effects on the mass distribution for relativistic objects in CBSs is also insignificant. Since most black-hole mass estimates have been made for low-mass X-ray binaries—X-ray nova during their quiescent state (Table 5)—and these systems form from WR + (A–M) binaries in which the more massive WR star explodes as a supernova, we should consider the possible disruption of WR + (A–M) binaries in the case of low-mass relativistic objects. The lower the mass of the relativistic object that forms, M_x, the higher the mass of the shell of the CO core that is ejected during the supernova (for a given CO-core mass M^f_{CO}). When the mass of the relativistic object M_x is small, the mass of the ejected CO-core shell can exceed half the total mass of the binary, which can lead to its disruption. In this case, the gap in the distribution of M_x at $2–4M_\odot$ (Fig. 9) could be due to an observational selection effect: the intrinsic mass distribution

for relativistic objects is continuous, and the observed gap is due to a deficit of CBSs with this range of M_x values, due to their disruption during the supernova explosions that led to the formation of the relativistic objects (recall that the data in Table 5 and Figs. 8, 9 were obtained exclusively from observations of CBSs).

This mechanism for the disruption of CBSs should most influence low-mass X-ray binaries in which the masses of the relativistic objects are lowest; i.e., X-ray binaries with neutron stars. Therefore, the observed number of such systems should be small. However a large number of low-mass X-ray binaries with neutron stars are observed [25]; in the case of X-ray novae, the number of systems with neutron stars is ~30% [27]. Apparently, the asymmetry of the supernova explosion and other factors help to preserve WR + (A–M) binaries from disrupting when the CO core ejects more than half the mass of the system during the supernova. Therefore, the gap in the distribution of M_x at $2–4M_\odot$ cannot be associated with a deficit of low-mass X-ray binary systems with the corresponding parameters.

Figure 9 presents the mass distributions for relativistic objects in binaries and for the CO cores of WR stars at the end of their evolution (Table 1), calculated taking into account mass loss via the stellar wind for $\alpha = 1$ and $\alpha = 2$. This figure clearly demonstrates that the mass distribution for the relativistic objects is bimodal with a gap at masses of $2–4M_\odot$, while the distribution for the CO-cores of WR stars shows no indication of bimodality, and is instead continuous. The gaps in the mass distribution for the CO cores at large masses ($M^f_{\rm CO} > 9M_\odot$) are associated with insufficient statistics, due to the small number of massive WR stars (the same is true of gaps in the black-hole mass distribution for masses exceeding $10M_\odot$).

It is striking that the masses of the CO-cores of WR stars at the end of their evolution $M^f_{\rm CO}$ lie in the range $M^f_{\rm CO} = (1–2)–(20–44)M_\odot$. This interval for $M^f_{\rm CO}$ encompasses the masses of both neutron stars and black holes. However, in contrast to the mass distribution for the relativistic objects, the distribution of $M^f_{\rm CO}$ shows no signs of bimodality, and is continuous. The mean CO-core mass is $\overline{M}^f_{\rm CO} = 10.3M_\odot$ for $\alpha = 1$ and $\overline{M}^f_{\rm CO} = 7.4M_\odot$ for $\alpha = 2$, close to the mean black-hole mass, $\overline{M}_{\rm BH} = 8–10M_\odot$.

The difference in the mass distributions for relativistic objects and their progenitors—the CO cores of WR stars at the end of their evolution, $M^f_{\rm CO}$—suggests that the mass of the progenitor is not the only parameter determining the nature of the relativistic object that is formed (neutron star, black hole). As noted in [40, 79], other characteristics of the stellar core also influence the formation of a neutron star or black hole, such as its rotation, magnetic field, etc. The effects of rotation for some WR stars were recently detected in spectropolarimetric observations, from depolarization at the frequencies of emission lines (see, for example, [85]). Rapidly rotating WR stars constitute ~20% of all known WR stars.

7. THE $2–4M_\odot$ GAP IN THE MASS DISTRIBUTION FOR RELATIVISTIC OBJECTS

Recently, Wijers [86] discussed the problem of low-mass black holes, with masses only slightly exceeding those for neutron stars. If a collapsing iron core of a massive star has a mass that is slightly lower than the maximum mass for a neutron star, a supernova explosion occurs, resulting in the formation of a neutron star. When the newly formed hot neutron star cools and neutrinos diffuse inward, its mass will slightly exceed the upper limit for the mass of a cool neutron star, and it will collapse into a black hole [87, 88]. The infall of ejected matter back onto the neutron star can also stimulate its collapse. Brandt *et al.* [59] interpreted the large peculiar velocity of the center of mass of the X-ray nova GRO J1655–40 as the result of a two-stage collapse of the core of a massive star. Brown and Bethe [88] predicted that, assuming a soft equation of state for the neutron-star matter (upper mass limit $\sim 1.5M_\odot$), stars with masses $18–30M_\odot$ should form low-mass black holes with masses $\leq 2M_\odot$. In this case, the existence of $\sim 5 \times 10^8$ low-mass black holes in the Galaxy is predicted—nearly as many as massive black holes. It is noted in [23] that, due to the very strong stellar wind of the naked helium core of the massive (WR) star in a binary, the formation of a low-mass black hole is less probable in a close binary system than in the case of a single massive star. Because of the large mass decrease due to the stellar wind, the final mass of the carbon–oxygen and iron core turns out to be appreciably lower for a WR star that forms as a result of mass transfer in a binary than in the case of a single star with the same mass [29, 89].

As indicated above, taking into account the clumpiness of the WR stellar wind decreases the required mass-loss rate appreciably, so that the final masses of the carbon–oxygen cores of many WR stars end up being very large (Table 1). Consequently, the effect of mass loss by a WR star in a binary system via its stellar wind cannot qualitatively change the situation compared to the case of a single massive star with a powerful hydrogen envelope.

Therefore, if they exist, low-mass black holes should exist with equal probability in binary systems and as single stars. This raises the question of why we have not thus far detected low-mass black holes in close binary systems. Wijers [86] proposed two X-ray binary systems that could contain low-mass black holes: 4U 1700–37 (a massive X-ray binary containing a non-pulsating compact X-ray source with mass $1.5–1.8M_\odot$

[25]) and GRO J0422 + 32 (a low-mass X-ray binary with a black hole that was proposed to have a comparatively low mass $M_x \leq 2.5M_\odot$ [90]). The recent new estimate of the orbital inclination i for the GRO J0422 + 32 system based on the ellipsoidal effect for the optical star indicates that the black hole in this system has a mass exceeding $9M_\odot$ [91]. In addition, the X-ray spectrum and spectral behavior of the compact component in the 4U 1700–37 system are virtually indistinguishable from the corresponding characteristics for typical X-ray pulsars in massive X-ray binaries [92]. Therefore, there is no firm basis to consider the non-pulsating compact X-ray source in the 4U 1700–37 system to be a low-mass black hole.

Thus, we are forced to suggest that, most likely, low-mass black holes either do not exist, or occur very rarely compared to more massive black holes. Consequently, this suggests that the $2–4M_\odot$ gap in the mass distribution for relativistic objects (Fig. 9) is real. For some reason, heavy neutron stars (with masses $\sim 3M_\odot$) and light black holes (with masses $\lesssim 3M_\odot$) are not born in nature, in spite of the fact that the progenitors of relativistic objects (the final CO cores of WR stars) have a continuous mass distribution from $(1–2)–(20–44)M_\odot$ (Fig. 9). Following [40, 79, 93, 94], we suggest that it is not only the mass of the progenitor that determines the nature of the relativistic object that forms (neutron star, black hole), but other characteristics as well: rotation, magnetic field, and so forth. Further theoretical studies in this promising direction are of considerable interest for stellar-evolution theory.

8. SEARCH FOR THE PROGENITORS OF LOW-MASS X-RAY BINARIES AMONG WR STARS IN SB1 AND WR + C BINARIES

Since the theory of the evolution of CBSs predicts that low-mass X-ray binaries with neutron stars and black holes could form from WR + (A–M) binaries after passage through a common-envelope stage, let us consider possible candidates for the progenitors of low-mass X-ray systems among SB1 (Table 3) and WR + C (Table 4) Wolf–Rayet binaries [24, 27]. Given that the largest orbital period among the low-mass X-ray binaries (Table 5) is $6\overset{d}{.}5$ (the V404 Cyg system) and the largest companion (A2V) mass is $\sim 2.5M_\odot$ (the 4U 1543–47 system), we should choose from Tables 3 and 4 WR binaries with periods $P \leq 6\overset{d}{.}5$ and companion masses $M_v \leq 2.5M_\odot$.

Using these criteria, only one SB1 Wolf–Rayet binary from Table 3 can be considered a candidate progenitor of a low-mass X-ray binary. This is the B87 system (WN6 + ?), with orbital period $P = 2\overset{d}{.}7596$ and mass function $f_{WR}(M) = 0.1M_\odot$. The low mass function (absolute lower limit for the mass of the invisible companion) suggests the presence in this binary of a low-mass A–M companion. In the list of proposed WR + C binaries (Table 4), 11 of the 17 (~65%) have periods $P < 6\overset{d}{.}5$. The mass functions $f_{WR}(M)$ for all these systems are quite small, suggesting the presence of low-mass A–M companions.

In the standard theory of the evolution of massive CBSs [31, 32], WR + C binaries are viewed as second-generation WR stars in binaries undergoing secondary mass transfer. The low-mass C companions in such WR + C systems are proposed to be relativistic objects [31, 32]. The main basis for this suggestion is the large heights z above the Galactic plane for the majority of WR + C systems, taken as evidence for supernova explosions in these binary systems. In our interpretation, the large heights z could be associated with the evaporation of massive stars from stellar clusters instead of with supernova explosions [95]. We should emphasize that powerful X-ray emission ($L_x \cong 10^{38}$ erg/s) is observed from the true WR + C binary Cyg X-3, together with many other peculiar manifestations of the presence of a relativistic object that is accreting matter from the stellar wind of the WR star (see, for example, [25]). Since the X-ray emission from all the proposed WR + C binaries (Table 4) is very weak ($L_x < 10^{33}$ erg/s), models in which the low-mass C companion is a relativistic object cannot be appropriate. Therefore, we have a basis for an alternative interpretation: in at least some of the proposed WR + C systems, the low-mass companions are not relativistic objects, but instead low-mass A–M stars similar to those observed in low-mass X-ray binaries (Table 5). Strict periodicity has been demonstrated for only two proposed WR + C binaries: HD 50896 (WN5 + ?, $P = 3\overset{d}{.}7650 \pm 0.0001$, $f_{WR}(M) = 0.025M_\odot$) [96] and HD 197406 (WN7 + ?, $P = 4\overset{d}{.}31364$, $f_{WR}(M) = 0.280M_\odot$). Possible orbital periods for the other proposed WR + C binaries (Table 4) require confirmation. In this connection, further studies of the proposed WR + C binaries and searches for low-mass, cool A–M main-sequence stars or subgiants in these systems is of considerable interest for the theory of the evolution of close binary systems.

ACKNOWLEDGMENTS

The author thanks K.A. Postnov for discussions of this work. This work was supported by a “Leading Scientific Schools of Russia” grant (00-15-96553) and by the Russian Foundation for Fundamental Research (99-02-17589).

REFERENCES

1. B. Paczynski, in *Wolf–Rayet and High Temperature Stars (IAU Symposium 49)*, Ed. by M. Barry and J. Sahade (D. Reidel, Dordrecht, 1973), p. 143.
2. P. S. Conti, Mem. Soc. R. Sci. Liege Collect. **9** (6), 193 (1976).

3. *Wolf–Rayet Stars: Binaries, Colliding Winds, Evolution (IAU Symposium 163)*, Ed. by K. A. van der Hucht and P. M. Williams (Kluwer, Dordrecht, 1995).
4. *Wolf–Rayet Stars in the Framework of Stellar Evolution*, Ed. by J. M. Vreux, A. Detal, D. Fraipont-Caro, E. Gosset, and G. Rauw (Liège Univ., Liège, 1996).
5. *Wolf–Rayet Phenomena in Massive Stars and Starburst Galaxies (IAU Symposium 193)*, Ed. by K. A. van der Hucht, G. Koenigsberger, and P. R. G. Eenens (ASP, San Francisco, 1999).
6. A. M. Cherepashchuk, in *Wolf–Rayet Stars in the Framework of Stellar Evolution*, Ed. by J. M. Vreux, A. Detal, D. Fraipont-Caro, E. Gosset, and G. Rauw (Liège Univ., Liège, 1996), p. 155.
7. A. M. Cherepashchuk, J. A. Eaton, and Kh. F. Khaliullin, Astrophys. J. **281**, 774 (1984).
8. A. F. J. Moffat, L. Drissen, R. Lamontagne, and C. Robert, Astrophys. J. **334**, 1038 (1988).
9. I. I. Antokhin, A. F. Kholtygin, and A. M. Cherepashchuk, Astron. Zh. **65**, 558 (1988) [Sov. Astron. **32**, 285 (1988)].
10. A. M. Cherepashchuk, Astron. Zh. **67**, 955 (1990) [Sov. Astron. **34**, 481 (1990)].
11. A. M. Cherepashchuk, in *Wolf–Rayet Stars and Interrelation with Other Massive Stars in Galaxies (IAU Symposium 143)*, Ed. by K. A. van der Hucht and B. Hidayat (Kluwer, Dordrecht, 1991), p. 280.
12. D. J. Hilllier, Astron. Astrophys. **247**, 455 (1991).
13. I. I. Antokhin, T. Nugis, and A. M. Cherepashchuk, Astron. Zh. **69**, 516 (1992) [Sov. Astron. **36**, 260 (1992)].
14. A. M. Cherepashchuk, in *Evolutionary Processes in Interacting Binary Stars*, Ed. by Y. Kondo, R. F. Sistero, and R. S. Polidan (Kluwer, Dordrecht, 1992), p. 123.
15. Kh. F. Khaliullin, Astron. Zh. **57**, 395 (1974) [Sov. Astron. **18**, 229 (1974)].
16. A. M. Cherepashchuk, in *Wolf–Rayet Stars: Binaries, Colliding Winds, Evolution (IAU Symposium 163)*, Ed. by K. A. van der Hucht and P. M. Williams (Kluwer, Dordrecht, 1995), p. 262.
17. A. F. J. Moffat, in *Wolf–Rayet Stars: Binaries, Colliding Winds, Evolution (IAU Symposium 163)*, Ed. by K. A. van der Hucht and P. M. Williams (Kluwer, Dordrecht, 1995), p. 213.
18. N. St.-Louis, A. F. J. Moffat, L. Drissen, *et al.*, Astrophys. J. **330**, 286 (1988).
19. A. F. J. Moffat, L. Drissen, C. Robert, *et al.*, Astrophys. J. **350**, 767 (1990).
20. A. F. J. Moffat and C. Robert, Astrophys J. **421**, 310 (1994).
21. *Thermal and Ionization Aspects of Flow from Hot Stars: Observations and Theory*, Ed. by H. J. G. L. M. Lamers and A. Sapar (Astronomical Society of the Pacific, San Francisco, 2000), Astron. Soc. Pac. Conf. Ser., Vol. 204.
22. T. Nugis, P. A. Crowther, and A. J. Willis, Astron. Astrophys. **333**, 956 (1998).
23. G. E. Brown, J. C. Weingartner, and R. A. M. J. Wijers, Astrophys. J. **463**, 297 (1996).
24. A. M. Cherepashchuk, in *Proceedings of an International Conference in Honour of Professor A. G. Massevitch: Modern Problems of Stellar Evolution*, Ed. by D. S. Wiebe (Zvenigorod, 1998), p. 198.
25. A. M. Cherepashchuk, N. A. Katysheva, T. S. Khruzina, and S. Yu. Shugarov, *Highly Evolved Close Binary Stars: Catalog* (Gordon and Breach, Amsterdam, 1996), p. 1.
26. A. M. Cherepashchuk, N. A. Katysheva, T. S. Khruzina, and S. Yu. Shugarov, *Highly Evolved Close Binary Stars: Finding Charts* (Gordon and Breach, Amsterdam, 1996), p. 1.
27. A. M. Cherepashchuk, Space. Sci. Rev. **93** (3–4) (2000).
28. N. Langer, Astron. Astrophys. **220**, 135 (1989).
29. S. E. Woosley, N. Langer, and T. A. Weaver, Astrophys. J. **411**, 823 (1993).
30. R. A. Chevalier, Space. Sci. Rev. **74**, 289 (1995).
31. A. V. Tutukov and L. R. Yungel'son, Nauchn. Inf. Astron. Sovet Akad. Nauk SSSR **27**, 58 (1973).
32. E. P. J. van den Heuvel, in *Structure and Evolution of Close Binary Systems (IAU Symposium 73)*, Ed. by P. Eggleton, S. Mitton, and J. Whelan (D. Reidel, Dordrecht, 1976), p. 35.
33. E. P. J. van den Heuvel and G. M. H. J. Habets, Nature **309**, 598 (1984).
34. I. Iben, A. V. Tutukov, and L. R. Yungelson, Astrophys. J., Suppl. Ser. **100**, 217 (1995).
35. I. Iben, A. V. Tutukov, and L. R. Yungelson, Astrophys. J., Suppl. Ser. **100**, 233 (1995).
36. S. Wellstein and N. Langer, Astron. Astrophys. **350**, 148 (1999).
37. V. M. Lipunov, K. A. Postnov, and M. E. Prokhorov, *The Scenario Machine: Binary Stars Population Synthesis* (Harwood Academic Publ., Amsterdam, 1996).
38. S. N. Shore, M. Livio, and E. P. J. van den Heuvel, *Interacting Binaries* (Springer-Verlag, Berlin, 1994).
39. S. Portegies Zwart, F. Verbunt, and E. Ergma, Astron. Astrophys. **321**, 207 (1997).
40. E. Ergma and E. P. J. van den Heuvel, Astron. Astrophys. **331**, L29 (1998).
41. P. P. Eggleton and F. Verbunt, Mon. Not. R. Astron. Soc. **220**, 13P (1986).
42. M. De Kool, E. P. J. van den Heuvel, and E. Pylyser, Astron. Astrophys. **183**, 47 (1987).
43. E. P. J. van den Heuvel and J. Heize, Nature **239**, 67 (1972).
44. C. H. B. Sybesma, Astron. Astrophys. **186**, 147 (1986).
45. D. Vanbeveren, Astron. Astrophys. **252**, 159 (1991).
46. K. A. van der Hucht, in *Wolf–Rayet Stars in the Framework of Stellar Evolution*, Ed. by J. M. Vreux *et al.* (Liège Univ., Liège, 1996), p. 1.
47. P. A. Crowther, L. J. Smith, D. J. Hillier, and W. Schmutz, Astron. Astrophys. **293**, 427 (1995).
48. A. Maeder, in *Wolf–Rayet Stars in the Framework of Stellar Evolution*, Ed. by J. M. Vreux *et al.* (Liège Univ., Liège, 1996), p. 39.
49. P. Massey, Astrophys. J. **246**, 153 (1981).
50. V. G. Karetnikov and A. M. Cherepashchuk, Astron. Zh. **75**, 539 (1998) [Astron. Rep. **42**, 476 (1998)].
51. A. M. Cherepashchuk and V. G. Karetnikov, Odessa Astron. Publ. **12**, 175 (1999).

52. J. P. De Greve, in *Wolf–Rayet Stars in the Framework of Stellar Evolution*, Ed. by J. M. Vreux *et al.* (Liège Univ., Liège, 1996), p. 55.
53. D. Vanbeveren, in *Evolutionary Processes in Binary Stars*, Ed. by M. Wijers, M. Davies, and C. Tout (Kluwer, Dordrecht, 1996), p. 155.
54. É. A. Antokhina and A. M. Cherepashchuk, Pis'ma Astron. Zh. **14**, 252 (1988) [Sov. Astron. Lett. **14**, 105 (1988)].
55. A. M. Cherepashchuk, Mon. Not. R. Astron. Soc. **194**, 761 (1981).
56. A. M. Cherepashchuk and A. F. J. Moffat, Astrophys. J. Lett. **424**, L53 (1994).
57. P. S. Conti, in *Wolf–Rayet Stars in the Framework of Stellar Evolution*, Ed. by J. M. Vreux *et al.* (Liège Univ., Liège, 1996), p. 655.
58. G. Izraellan, R. Rebolo, G. Basri, *et al.*, Nature **401**, 142 (1999).
59. W. N. Brandt, Ph. Podsiadlowski, and S. Sigurdsson, Mon. Not. R. Astron. Soc. **277**, L35 (1995).
60. B. Paczynski, Acta Astron. **21**, 1 (1971).
61. L. R. Yungel'son and A. G. Masevich, Itogi Nauki Tekh., Ser. Astron. **21**, 43 (1982).
62. D. Schaerer and A. Maeder, Astron. Astrophys. **263**, 129 (1992).
63. P. Bartzakos, A. F. J. Moffat, and V. S. Niemela, Mon. Not. R. Astron. Soc., 2000 (in press).
64. A. M. Cherepashchuk, Pis'ma Astron. Zh. **2**, 256 (1976) [Sov. Astron. Lett. **2** (4), 138 (1976)].
65. A. M. T. Pollock, Astrophys. J. **320**, 283 (1987).
66. S. Mereghetti, T. Belloni, M. Shara, and L. Drissen, Astrophys. J. **424**, 943 (1994).
67. C. Robert and A. F. J. Moffat, Astrophys. J. **343**, 902 (1989).
68. G. Rauw, J. M. Vreux, E. Gosset, *et al.*, Astron. Astrophys. **306**, 771 (1996).
69. J. Schweickhardt, W. Schmutz, O. Stahl, *et al.*, Astron. Astrophys. **347**, 127 (1999).
70. V. S. Niemela, in *Wolf–Rayet Stars: Binaries, Colliding Winds, Evolution (IAU Symposium 163)*, Ed. by K. A. van der Hucht and P. M. Williams (Kluwer, Dordrecht, 1995), p. 223.
71. S. V. Marchenko, A. F. J. Moffat, and G. Koenigsberger, Astrophys. J. **422**, 810 (1994).
72. S. V. Marchenko, A. F. J. Moffat, P. R. J. Eenens, *et al.*, Astrophys. J. **450**, 811 (1995).
73. D. Lewis, A. F. J. Moffat, J. M. Matthews, *et al.*, Astrophys. J. **405**, 312 (1993).
74. I. R. Stevens, Astrophys. J. **404**, 281 (1993).
75. A. M. Cherepashchuk, Usp. Fiz. Nauk **166**, 809 (1996) [Phys. Usp. **39**, 759 (1996)].
76. A. V. Tutukov and A. M. Cherepashchuk, Astron. Zh. **74**, 497 (1997) [Astron. Rep. **41**, 355 (1997)].
77. P. A. Charles, in *Theory Black Holes Accretion Disks*, Ed. by M. A. Abramowicz, G. Bjornsso, and J. Pringlo (in press); astro-ph/9806217.
78. S. E. Thorsett and D. Chakrabarty, Astrophys. J. **512**, 288 (1999); astro-ph/9803260.
79. A. V. Tutukov and A. M. Cherepashchuk, Astron. Zh. **62**, 1124 (1985) [Sov. Astron. **29**, 654 (1985)].
80. C. D. Bailyn, R. K. Jain, P. Coppi, and J. A. Orosz, Astrophys. J. **499**, 367 (1998).
81. J. van Paradijs and J. E. McClintock, in *X-ray Binaries*, Ed. by W. H. G. Lewin (Cambridge Univ. Press, Cambridge, 1995), p. 58.
82. E. A. Antokhina and A. M. Cherepashchuk, Pis'ma Astron. Zh. **23**, 883 (1997) [Astron. Lett. **23**, 773 (1997)].
83. T. Shahbaz, Mon. Not. R. Astron. Soc. **298**, 153 (1998).
84. S. O. Tagieva, A. Ankay, O. H. Guseinov, and A. Sezer, Astron. Astrophys. Trans. (2000).
85. T. J. Harries, D. J. Hillier, and I. D. Howarth, Mon. Not. R. Astron. Soc. **296**, 1072 (1998).
86. A. M. J. Wijers, in *Evolutionary Processes in Binary Stars*, Ed. by A. M. J. Ralf *et al.*; NATO ASI Ser., Ser. C **477**, 327 (1996).
87. G. S. Bisnovatyi-Kogan, in *Proceedings of an ESO Workshop on SN 1987 A, July 3–6, 1987*, Ed. by I. Danziger (European Southern Observatory, Garching bei München, 1987), p. 347.
88. G. E. Brown and H. A. Bethe, Astrophys. J. **423**, 659 (1994).
89. S. E. Woosley, N. Langer, and N. A. Weaver, Astrophys. J. **448**, 315 (1995).
90. J. Casares, A. S. Martin, P. A. Charles, *et al.*, Mon. Not. R. Astron. Soc. **276**, L35 (1995).
91. G. Beekman, T. Shahbaz, T. Naylor, *et al.*, Mon. Not. R. Astron. Soc. **290**, 303 (1997).
92. A. P. Reynolds, A. Owens, L. Kaper, *et al.*, Astron. Astrophys. **349**, 873 (1999).
93. V. S. Imshennik, Space Sci. Rev. **74**, 325 (1995).
94. G. S. Bisnovatyĭ-Kogan, Astron. Zh. **47**, 813 (1970) [Sov. Astron. **14**, 652 (1971)].
95. A. Poveda, J. Ruíz, and C. Allen, Tonantzintla y Tacubaya Bull. **4**, 86 (1967).
96. L. N. Georgiev, G. Koenigsberger, M. M. Ivanov, *et al.*, Astron. Astrophys. **347**, 583 (1999).
97. S. V. Marchenko, A. F. J. Moffat, and P. R. J. Eenens, Publ. Astron. Soc. Pac. **110**, 1416 (1998).

Translated by D. Gabuzda

Astronomy Reports, Vol. 45, No. 2, 2001, pp. 138–143. Translated from Astronomicheskiĭ Zhurnal, Vol. 78, No. 2, 2001, pp. 165–171.

Synchrotron Spectra of Short-Period Pulsars

I. F. Malov

Pushchino Radio Astronomy Observatory, Astro Space Center, Lebedev Institute of Physics, Moscow Region, 142292 Russia

Received January 11, 2000

Abstract—A model with synchrotron radiation near the light cylinder is proposed to explain the observed spectra of short-period pulsars ($P \le 0.1$ s). These spectra can be described if a power-law energy distribution of the emitting electrons with exponent $\gamma = 2$–8 is assumed. For most pulsars, the peak frequency ν_m is below 10 MHz. The $\nu_m(\gamma)$ dependence is derived, and shows that the peak frequencies for pulsars with spectral indices $\alpha < 1.5$ may fall in the observable range. In particular, ν_m may be $\nu_m \sim 100$ MHz for PSR J0751 + 1807 and PSR J1640 + 2224. The observed radio spectrum of Geminga (PSR J0633 + 1746) can be described by a synchrotron model with a monoenergetic or Maxwellian distribution of relativistic electrons and a small angle β between the spin axis and magnetic moment ($\beta \sim 10°$). © *2001 MAIK "Nauka/Interperiodica".*

1. INTRODUCTION

In [1], we analyzed differences in the parameters of pulsars with short ($P < 0.3$ s) and long ($P \sim 1$ s) rotational periods *P*. Subsequently, the accumulated observational data and theoretical results led to the hypothesis that different radiation models were appropriate for these two groups of sources (see, for example, [2]). There is much evidence that radiation in pulsars with $P \le 0.1$ s is generated by the synchrotron mechanism [3–4] near the light cylinders of these objects. The radius of the light cylinder

$$r_{LC} = \frac{cP}{2\pi} \tag{1}$$

corresponds to rigid rotation at the velocity of light. The synchrotron model can be tested by comparing the observed spectra of short-period pulsars with predictions based on models in which their radiation has a synchrotron nature. The spectra of northern and southern millisecond pulsars [5, 6] enable us to perform such a comparison, and to derive constraints on these objects' parameters in order for the model to be valid. The present paper is devoted to this problem.

2. ENERGY DISTRIBUTIONS OF THE EMITTING ELECTRONS

The appearance of a synchrotron spectrum depends on the magnetic-field intensity, plasma density, and distributions of the emitting particles in pitch angle and energy. The most common distributions considered [7] are monoenergetic

$$N(\varepsilon) = N_{01}\delta(\varepsilon - \varepsilon_0), \tag{2}$$

relativistic Maxwellian

$$N(\varepsilon) = N_{02}\varepsilon^2 e^{-(\varepsilon/kT)^2}, \tag{3}$$

and power-law

$$N(\varepsilon) = N_{03}\varepsilon^{-\gamma}. \tag{4}$$

Here, $\varepsilon = m_e c^2\Gamma$ is the energy of a single electron with Lorentz factor $\Gamma = \left(1 - \frac{V^2}{c^2}\right)^{-1/2}$, T is the electron temperature, and N_{01}, N_{02}, and N_{03} are constants.

The distribution function of the emitting electrons (or positrons) has the form presented in Fig. 1 of [8], where Γ_b is the Lorentz factor corresponding to the maximum in the distribution of the primary-beam particles, Γ_p is the Lorentz factor at the maximum of the secondary-plasma particles, and $\Delta\Gamma$ is the width of the distribution function of the secondary particles. Estimates show that the observed radio emission is associated with secondary plasma, whereas the emission of the beam electrons can account for the optical, X-ray, and gamma-ray radiation [3].

If $\Delta\Gamma \ll \Gamma_p$, we can roughly assume that the emitting particles have a monoenergetic distribution. In this case, the total spectrum is similar to the spectrum of a single particle (Fig. 2), and peaks at a frequency [7]

$$\nu_M = 0.29\nu_{\rm cr} = \frac{0.87}{4\pi}\frac{eH}{mc}\Gamma^2\sin\psi, \tag{5}$$

where $\psi = (\mathbf{H}, \mathbf{V})$ is the pitch angle (which we assume to be the same for all radiating particles). At frequencies $\nu \gg \nu_M$, the intensity of the emission decrease exponentially:

$$I(\nu) \propto \sqrt{\frac{\nu}{\nu_{\rm cr}}}e^{-\nu/\nu_{\rm cr}}. \tag{6}$$

The spectra of pulsars beyond the maximum have a power-law, not exponential, form. Only in Geminga, which can be classified as a short-period pulsar accord-

ing to many of its parameters [9], is a very steep drop in the flux observed at frequencies above $\nu_M \approx 100$ MHz [10]. This can be interpreted as an exponential cutoff. In this case, the following relationship should be satisfied:

$$H\Gamma^2 \sin\psi = 82, \quad (7)$$

which, for a dipole field and mean pitch angle [4]

$$\bar{\psi} = \left[\frac{3\pi^2 m^4 c^6 \left(\frac{r}{R_*}\right)^9 \rho}{e^5 H_s^3 P^2 r \Gamma_p^2}\right]^{1/2} \quad (8)$$

is valid for $\Gamma_p = 10$, $\rho \approx r_{LC} \approx 10^9$ cm, $r = 0.9\, r_{LC}/\sin\beta$, and an angle between the magnetic-moment and spin-axis vectors of $\beta = 19°$, i.e., for quite reasonable values of these parameters.

At frequencies $\nu < \nu_M$, the intensity should decrease as $\left(\frac{\nu}{\nu_{cr}}\right)^{1/3}$. Observations of Geminga show that, indeed, the flux decreases below 100 MHz [10]; however, a detailed comparison of the theory and observations will become possible only after the observed spectrum of this source has been extended to lower frequencies.

If $\Delta\Gamma \sim \Gamma_p$, we can approximately assume the distribution of the secondary-plasma particles to be Maxwellian. However, in this case, the high-frequency spectrum should be much steeper than observed pulsar spectra. Indeed, the maximum spectral index $S_\nu \propto \nu^{-\alpha}$, defined as α, for southern pulsars is 2.9 [6], whereas the spectral index at high frequencies for a synchrotron spectrum with a Maxwellian particle distribution should be $\alpha > 3$ [7]. Again, only in the case of Geminga might such a distribution be acceptable. If we suppose that the spectral maximum corresponds to optical depths $\tau \sim 1$, we can estimate the height at which the emission is generated, together with certain parameters of the pulsar. The total spectrum will peak at ~100 MHz for the parameter values

$$r = \frac{r_{LC}}{\sin\beta}, \quad \beta = 10°, \quad kT = mc^2, \quad \psi \sim 10^{-2} \text{ rad},$$

which are fairly consistent with current ideas about Geminga. At large optical depths, the emission intensity for a Maxwellian distribution decreases as ν^2 [7]. As for the monoenergetic distribution, a comparison of this effect with the observed flux decreases at low frequencies will become possible only after further acquisition of observational data.

As noted above, the spectra of millisecond pulsars in the range studied, from 400 to 1400 MHz, have a power-law form. In the synchrotron model, such spectra can be obtained with a power-law energy distribution (4) for the emitting electrons. In this case, the observed spectral index α is related to the exponent of the energy spectrum γ as

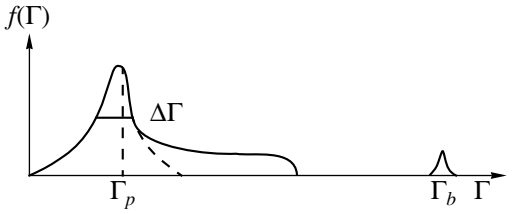

Fig. 1. Distribution function of the electrons in the Lorentz factor Γ in the magnetosphere of a pulsar.

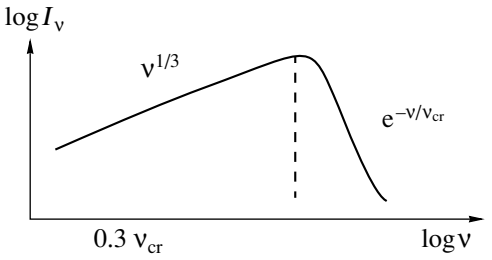

Fig. 2. Synchrotron radiation spectrum for a relativistic electron.

$$\alpha = \frac{\gamma - 1}{2}. \quad (9)$$

The values of α for northern-hemisphere pulsars [5] are from 0.5 ± 0.5 to 3.5 ± 0.5, while $\alpha = 1.1$–2.9 [6] for southern objects. These values correspond to a range of $\gamma = 2\alpha + 1$ from 2.0 to 8.0. Such slopes could correspond to the declining post-maximum section at $\Gamma = \Gamma_p$ on the accepted secondary-particle distribution for pulsars (Fig. 1).

3. MODELS FOR THE POWER-LAW DISTRIBUTION OF ELECTRONS

Let us estimate the frequency of the spectral maximum ν_M, which, for a power-law energy distribution for the emitting electrons, is a function of γ and is determined from the equations [7]

$$\frac{\nu_1}{\nu_m} = \tau_m^{\frac{2}{\gamma+4}}, \quad (10)$$

$$e^{\tau_m} = 1 + \frac{\gamma+4}{5}\tau_m, \quad (11)$$

$$\nu_1 = 2c_1 (sc_6)^{2/(\gamma+4)} N_0^{2/(\gamma+4)} (H\sin\psi)^{\frac{\gamma+2}{\gamma+4}}, \quad (12)$$

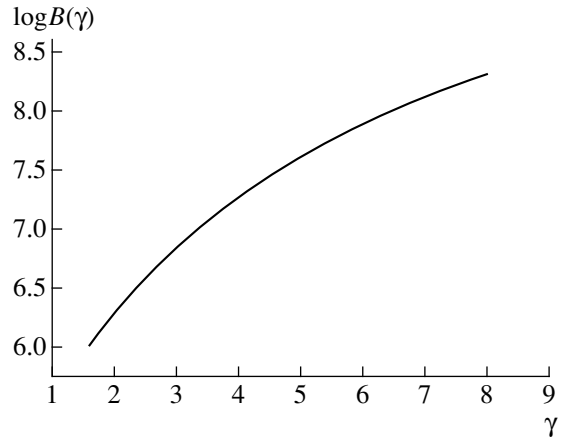

Fig. 3. Function $B(\gamma)$ (Table 1).

where

$$c_1 = \frac{3e}{4\pi m^3 c^5}, \tag{13}$$

$$c_6 = \frac{\pi e m^5 c^{10}}{24\sqrt{3}}\left(\gamma + \frac{10}{3}\right)\Gamma\left(\frac{3\gamma+2}{12}\right)\Gamma\left(\frac{3\gamma+10}{12}\right), \tag{14}$$

$$N_0 = n_p(\gamma-1)\varepsilon_0^{\gamma-1}. \tag{15}$$

For $\gamma = 2.0$–8.0, the optical depth τ_m corresponding to the spectral maximum is 0.35–15.5. Expressing the plasma density n_p in terms of the beam density n_b, namely

$$n_p = \frac{n_b\Gamma_b}{2\Gamma_p} = \frac{H}{2Pce}\frac{\Gamma_b}{\Gamma_p}, \tag{16}$$

and adopting

$$\varepsilon_0 = mc^2, \tag{17}$$

$$s = 0.1r_{LC}, \tag{18}$$

$$\rho = r_{LC}, \tag{19}$$

for a dipole magnetic field and ψ from Eq. (8), we obtain

$$\nu_m = A(\gamma)\tau_m^{-\frac{2}{\gamma+4}}P^{\frac{\gamma-10}{2(\gamma+4)}}H_s^{\frac{2-\gamma}{2(\gamma+4)}} \times \Gamma_b^{\frac{2}{\gamma+4}}\Gamma_p^{-1}R_*^{\frac{3(2-\gamma)}{2(\gamma+4)}}(\sin\beta)^{\frac{4-\gamma}{\gamma+4}}, \tag{20}$$

where

$$A(\gamma) = 10^{\frac{-0.78\gamma-3.84}{\gamma+4}} \times\left[(\gamma-1)\left(\gamma+\frac{10}{3}\right)\Gamma\left(\frac{3\gamma+2}{12}\right)\Gamma\left(\frac{3\gamma+10}{12}\right)\right]^{\frac{2}{\gamma+4}} \times e^{-\frac{2+3\gamma}{2(\gamma+4)}}m^{\frac{\gamma}{\gamma+4}}c^{\frac{7\gamma-2}{2(\gamma+4)}}. \tag{21}$$

Relationship (20) can be written

$$\nu_m = B(\gamma)P^{\frac{\gamma-10}{2(\gamma+4)}}H_s^{\frac{2-\gamma}{2(\gamma+4)}}(\sin\beta)^{\frac{4-\gamma}{\gamma+4}}. \tag{22}$$

The function

$$B(\gamma) = A(\gamma)\Gamma_b^{\frac{2}{\gamma+4}}\Gamma_p^{-1}R_*^{\frac{3(2-\gamma)}{2(\gamma+4)}}\tau_m^{-\frac{2}{\gamma+4}} \tag{23}$$

is tabulated in Table 1 and presented in Fig. 3. We assume the above values of Γ_b and Γ_p to be the same for all objects in Table 1. Table 2 lists the values of $\nu_m^* = \nu_m(\sin\beta)^{\frac{\gamma-6}{2(\gamma+4)}}$, calculated with $R_* = 10^6$ cm, $\Gamma_b = 5\times10^6$, and $\Gamma_p = 10^3$ on the basis of Eq. (22). The values of the pulsar parameters from [5, 6, 11] are also given. The spectral indices α in the left-hand and right-hand parts of the corresponding column are taken from [6] and [5], respectively. We have taken α for PSR J1640 + 2224 from [12]. When calculating ν_m^* for pulsars having two measurements of α, we took the mean value, $\bar{\alpha} = \frac{\alpha_1+\alpha_2}{2}$. We also took into account the fact that catalogs use magnetic-field values $H_k = H_s\sin\beta$.

We can see from Table 2 that $\nu_m^* \lesssim 10$ MHz for all the pulsars, except PSR J0751 + 1807 and PSR J1640 + 2224. To identify possible maxima in the spectra of pul-

Table 1

γ	$B(\gamma)$
1.6	1.08×10^6
2.0	2.03
2.4	3.48
2.8	5.60
3.2	8.65
3.6	1.29×10^7
4.0	1.84
4.4	2.57
4.8	3.48
5.2	4.60
5.6	5.97
6.0	7.61
6.4	9.58
6.8	1.19×10^8
7.2	1.46
7.6	1.70
8.0	2.15

sars J0613–0200, J1713 + 0747, B1855 + 09, and J2337 + 1439, observations at decameter waves are necessary. Meter-wavelength data are needed for PSR J1640 + 2224 with $\nu_m^* = 49$ MHz and PSR J0751 + 1807 with $\nu_m^* = 37$ MHz.

We should emphasize that we did not take into account the effect of the factor $f(\beta) = \sin\beta^{\frac{\gamma-6}{2(\gamma+4)}}$ in our calculations. Table 3 lists intervals of $f(\beta)$ for $\gamma = 2.0$–8.0. For angles $\beta > 30°$, the effect of this factor can be neglected. For $\beta < 10°$, taking the factor $f(\beta)$ into account in the transition from ν_m^* to ν_m can change the frequency by more than a factor of two. In particular, in PSR J0751 + 1807, $\gamma = 2.8$ and $f(\beta) = 0.39$–0.66 when $\beta = 1°$–$10°$ and $f(\beta) = 0.66$–1.2 when $\beta = 10°$–$90°$; i.e., $\nu_m \sim 2\nu_m^*$ for small values of β and $\nu_m \sim \nu_m^*$ for large values of β. Similar corrections apply to PSR J1640 + 2224, with $\gamma = 2.6$.

To estimate the peak frequencies in millisecond pulsars, it is useful to analyze the dependences of ν_m on other parameters in Eq. (22). With this in mind, we will use the sample of 24 objects in Table 2 with calculated values of ν_m^*. The mean periods, surface magnetic fields, and energy-spectrum exponents for these objects are $\bar{P} = 9.4$ ms, $\overline{\log H_k}$ [G] = 8.815, and $\bar{\gamma} = 4.8$. Figures 4–6 show the $\nu_m^*(\gamma)$, $\nu_m^*(P)$, and $\nu_m^*(H_k)$ dependences. The strongest effect on the peak frequency is exerted by γ (in the observable range of γ, ν_m^* changes by a factor of almost 40). According to Fig. 4, we should expect that the maxima in pulsars with small spectral indices will be observed in an accessible frequency band (at ≥100 MHz). This conclusion is reflected in Table 2. We can see from Figs. 5 and 6 that an increase of H_k by three orders of magnitude results in a decrease of ν_m^* by a factor of only three, and for P from 1 to 60 ms, $\nu_m^* =$ (3–11) MHz.

4. DISCUSSION AND CONCLUSIONS

The above analysis shows that a synchrotron-radiation model can explain the observed spectra of millisecond pulsars in the case of a power-law electron-energy distribution. Using formula (22) to estimate the peak frequency for the spectra of short-period pulsars with normal values for the magnetic field ($H_k \sim 10^{12}$ G) results in very small values of ν_m^*. For example, in PSR 0531 + 21 and PSR 0833–45, $\nu_m^* = 2.47 \times 10^5$ Hz. This implies that we should not observe synchrotron self-absorption in the radio spectra of these objects. For some pulsars, values of ν_m around 100 MHz are predicted (see Table 2). In the spectra of some, an appreciable flattening below 400 MHz is, indeed, observed (this is true, for example, of PSR J1640 + 2224 [12]). However, to test the synchrotron model, additional data at lower frequencies (≤100 MHz) are required.

Above, we have used the formulas for incoherent synchrotron radiation. However, it is known that the radio emission of pulsars is coherent, which is usually

Table 2

No.	PSR	P, ms	$\log H_k$	α	ν_m^*, MHz
1	J0034–0534	1.9	8.05	2.6	6.08
2	J0437–4715	5.8	8.76	1.1 (1.8)	9.58
3	J0613–0200	3.1	8.27	1.5 (1.9)	11.61
4	J0711–6830	5.5		1.7 (1.4)	
5	J1024–0719	5.2		1.7 (1.5)	
6	J1045–4509	7.5	8.58	2.0 (1.5)	7.46
7	J1455–3330	8.0		1.8	
8	J1603–7202	14.8		1.8 (1.3)	
9	J1623–2631	11.0	9.48	1.5	6.52
10	J1643–1224	4.6	8.60	1.9 (2.4)	5.73
11	J1730–2304	8.1	8.60	1.9 (1.8)	6.52
12	J1744–1134	4.1		1.8 (1.6)	
13	J1804–2718	9.3		2.9 (3.2)	
14	J1823–3023A	5.4	9.64	2.7	2.16
15	J1911–1114	3.6		2.6 (3.3)	
16	J2051–0827	4.5		1.6 (1.8)	
17	J2124–3358	4.9		1.5 (1.1)	
18	J2129–5718			2.2	
19	J2145–0750	16.1		2.1 (1.6)	
20	J0751 + 1807	3.5	8.23	0.9	36.67
21	J1012 + 5307	5.3	8.45	1.8	8.26
22	J1022 + 1001	16.5		1.7	
23	B1257 + 12	6.2	8.95	1.9	5.89
24	J1518 + 4904	40.9		0.5	
25	B1534 + 12	37.9	9.99	3.0	1.11
26	B1620–26	11.1	9.48	2.5	2.38
27	J1640 + 2224	3.2	7.99	[12] 0.8	49.26
28	J1713 + 0747	4.6	8.30	1.5	12.70
29	B1802–07	23.1	9.53	1.0	9.77
30	B1855 + 09	5.4	8.56	1.3	14.60
31	B1913 + 16	59.0	10.36	1.4	3.06
32	B1937 + 21	1.6	8.61	2.3	6.34
33	B1953 + 29	6.1	10.43	2.2	2.39
34	J2229 + 2643	3.0	7.88	2.2	8.22
35	J2337 + 1439	3.4	7.97	1.4	17.97
36	J0218 + 4232	2.3	8.63	2.8	3.51
37	J0621 + 1002	28.9		2.5	
38	B1957 + 20	1.6	8.22	3.5	3.24

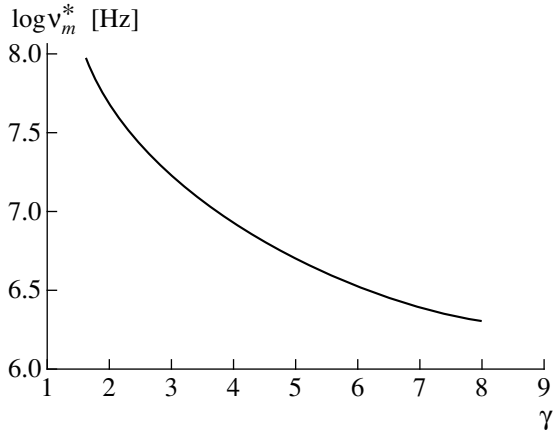

Fig. 4. The $\log \nu_m^*(\gamma)$ dependence for $P = 9.4$ ms and H_k (G) = 8.815.

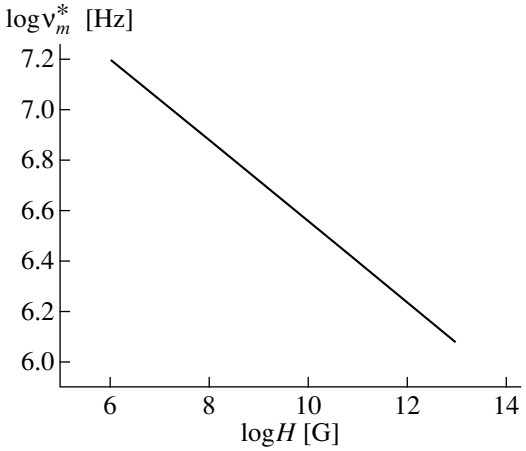

Fig. 5. The $\log \nu_m^*(H_k)$ dependence for $\gamma = 4.8$ and $P = 9.4$ ms.

associated with the development of plasma instabilities. The development of synchrotron instability in a relativistic plasma moving along a ring was considered by Goldreich and Keeley [13]. Precisely this instability can play an essential role in the generation of the observed emission from short-period pulsars [2]. A detailed development of the theory of coherent synchrotron radiation is necessary here. We assume that there exist near the light cylinder plasma irregularities (clumps, layers, solitons) that radiate coherently at decimeter and meter wavelengths. The longitudinal size of such irregularities should be less than the wavelength. For the purpose of estimation, we assume this size to be 20 cm. The transverse size of the irregularities can be larger. For example, let us estimate the total power emitted by a cylindrical layer with a diameter of ~2 m. Its volume is ~10^6 cm^3. The plasma density n_p at a distance r_{LC} can be taken to be 10^9 cm^{-3}, and the total number of particles in the layer to be $N = 10^{15}$. The synchrotron power emitted by a single particle [7]

$$q = \frac{2e^4H^2\gamma^2\sin^2\psi}{3m^2c^3} \qquad (24)$$

for $\psi \sim 10^{-2}$ rad is $\sim 5 \times 10^{-9}$ erg/s, and the total luminosity of the layer is $W \sim qN^2 \sim 5 \times 10^{21}$ erg/s. For the adopted length for the emission-generation region, $s \sim 0.1r_{LC} \sim 5 \times 10^6$ cm (for $P = 9.4$ ms), the existence of 10^5 such layers, to provide an integrated radio luminosity comparable to that observed, is quite plausible. Thus, these estimates show that the model considered here does is consistent with the energy requirements inferred from observations.

Table 3

β, deg	$f(\beta)$
1	0.26–1.40
2	0.33–1.32
3	0.37–1.28
4	0.41–1.25
5	0.44–1.23
6	0.47–1.21
7	0.50–1.19
8	0.52–1.18
9	0.54–1.17
10	0.56–1.16
20	0.70–1.09
30	0.79–1.06
40	0.86–1.04
50	0.91–1.02
60	0.95–1.01
70	0.98–1.01
80	0.99–1.00
90	1

We list the main conclusions of the work below.

(1) We have proposed a model with synchrotron radiation near the light cylinder to explain the observed spectra of short-period pulsars ($P \leq 0.1$ s).

(2) The spectrum of Geminga, which can be classified as a short-period pulsar according to a number of its parameters and their dependences, is satisfactorily described by a monoenergetic or relativistic Maxwellian energy distribution for the emitting electrons. In this case, consistency with the observations demands that the angle β between the spin axis and magnetic moment be small (β ~ 10). The requirement that the angle β be small was already demonstrated from other considerations in [9].

(3) The spectra of millisecond pulsars can be described if a power-law energy distribution is assumed for the rela-

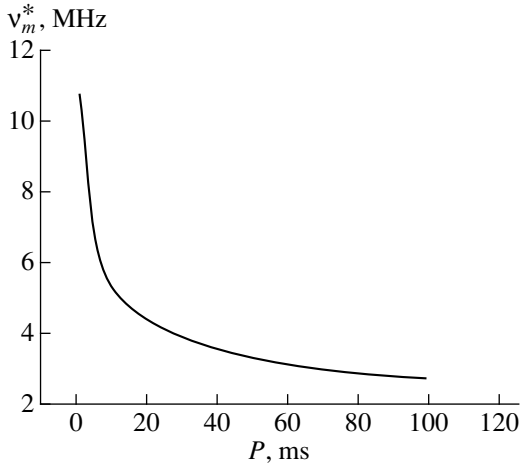

Fig. 6. The $\log \nu_m^*(P)$ dependence for $\gamma = 4.8$ and H_k (G) = 8.815.

tivistic electrons. The exponent γ for this distribution should be between two and eight.

(4) Estimates of the peak frequencies ν_m for the synchrotron spectra of short-period pulsars indicate that, for most such objects, self-absorption begins only at very low frequencies ($\nu_m \lesssim 10$ MHz). This conclusion may be confirmed by the results of [14], which demonstrate that the spectrum of the pulsar PSR B1937 + 21 remains linear down to 26 MHz.

(5) The $\nu_m(\gamma)$, $\nu_m(P)$, and $\nu_m(H_k)$ dependences for our model show that the major role in determining the peak frequency is played by the energy distribution γ. As γ changes from two to eight, ν_m decreases from 7×10^7 to 10^6 Hz. The influence of other parameters is much weaker.

(6) We predict that ν_m will be in an observable waveband for pulsars with the least steep spectra (with spectral indices $\alpha < 1.5$). Detection of the predicted low-frequency cutoff is most probable in the spectra of PSR J0751 + 1807 ($\alpha = 0.9$) and PSR J1640 + 2224 ($\alpha = 0.8$). Observations at frequencies ≤100 MHz are desirable in this connection.

(7) The model proposed could be tested using polarization observations. For a uniform magnetic field and small source optical depth, the degree of polarization p does not depend on frequency and is described by the relationship [7]

$$p = \frac{\gamma + 1}{\gamma + 7/3} = \frac{\alpha + 1}{\alpha + 5/3}. \quad (25)$$

In the interval of γ from two to eight, p grows from 0.69 to 0.87. For a nonuniform magnetic field and increasing source optical depth, the degree of polarization becomes considerably lower; the character of the $p(\gamma)$ dependence also changes. For an optically thick source [7],

$$p = \frac{3}{6\gamma + 13} = \frac{3}{12\alpha + 19},$$

i.e., when γ increases from two to eight, the degree of polarization decreases from 12 to 5%. Data on the polarization of millisecond pulsars [15] show that p is confined to the interval from 12 to 70%, and there is no correlation between p and γ. This result can be explained in the proposed model by invoking a nonuniform magnetic field in an emission-generation region with some finite optical depth, which is different in different pulsars. Therefore, more accurate polarization measurements for a larger number of pulsars are desirable to further test the model.

ACKNOWLEDGMENTS

This work was supported by the Russian Foundation for Basic Research (project code 97-02-17372) and INTAS (grant 96-0154). The author is grateful to L.B. Potapova for help in the preparation of the materials for printing and to an anonymous referee for useful comments.

REFERENCES

1. I. F. Malov and S. A. Suleĭmanova, Astrofizika **18**, 107 (1982).
2. I. F. Malov, Astron. Zh. **74**, 697 (1997) [Astron. Rep. **41**, 617 (1997)].
3. I. F. Malov, Astron. Zh. **76**, 825 (1999) [Astron. Rep. **43**, 727 (1999)].
4. I. F. Malov and G. Z. Machabeli, Astron. Zh. **76**, 788 (1999) [Astron. Rep. **43**, 691 (1999)].
5. M. Kramer, K. M. Xilouris, D. R. Lorimer, *et al.*, Astrophys. J. **501**, 270 (1998).
6. M. Toskano, M. Bailis, R. N. Manchester, and J. S. Sandhu, Astrophys. J. **506**, 863 (1998).
7. A. Pacholczyk, *Radio Astrophysics. Nonthermal Processes in Galactic and Extragalactic Sources* (Freeman, San Francisco, 1970; Mir, Moscow, 1973).
8. J. Arons, in *Proceedings of the Varenna Summer School and Workshop on Plasma Astrophysics, 1981*, p. 273.
9. I. F. Malov, Astron. Zh. **75**, 281 (1998) [Astron. Rep. **42**, 246 (1998)].
10. V. M. Malofeev, in *Physics of Neutron Stars* (St. Petersburg, 1999), p. 29.
11. J. H. Taylor, R. N. Manchester, A. G. Lyne, and F. Camilo, private communication, 1995.
12. M. Kramer, C. Lange, D. R. Lorimer, *et al.*, Astrophys. J. **526**, 957 (1999).
13. P. Goldreich and D. A. Keeley, Astrophys. J. **170**, 463 (1971).
14. W. Sieber and J. H. Seiradakis, Preprint No. 164, MPIfR (Bonn, 1983).
15. K. M. Xilouris, M. Kramer, A. Jessner, *et al.*, Astrophys. J. **501**, 286 (1998).

Translated by G. Rudnitskiĭ

Astronomy Reports, Vol. 45, No. 2, 2001, pp. 144–156. Translated from Astronomicheskiĭ Zhurnal, Vol. 78, No. 2, 2001, pp. 172–186.

Modeling the Spectral Energy Distributions of L Dwarfs

Ya. V. Pavlenko

Main Astronomical Observatory, National Academy of Sciences of Ukraine, Golosiiv, Kiev-127, 03680 Ukraine

Received March 1, 2000

Abstract—Mechanisms for the formation of the optical (λλ500–950 nm) spectra of L dwarfs—stars and substellar objects with $T_{\rm eff} < 2200$ K—are discussed. Their spectral energy distributions are determined primarily by the K I and Na I resonance-doublet absorption lines. The equivalent widths of these absorption lines formally computed using the dusty model atmospheres of Tsuji can reach several thousand angstroms. In this case, the extended wings of these lines form a pseudo-continuum for weaker absorption lines and even molecular bands. Mechanisms for the broadening of alkali-element lines in the atmospheres of late-type stars due to interactions between neutral atoms and hydrogen molecules are analyzed. The computed optical spectral energy distributions of several L dwarfs are compared with their observed spectra. © *2001 MAIK "Nauka/Interperiodica".*

1. INTRODUCTION

Studies of the formation of strong alkali lines in the atmospheres of late-type stars are undoubtedly of interest for a number of problems in modern astrophysics. The extended wings of such absorption lines carry information about the physical conditions—gas pressure, temperature, and velocity field—in the atmospheric layers where they form. Modeling these lines is necessary for testing our views of the physics of intraatomic processes involving radiation fields and interactions with other atoms and molecules. These lines are far from the strongest in the spectra of solar-type stars. Their intensity increases with decreasing effective temperature below 4000 K; however, the line wings become appreciably blended by numerous lines of other atoms and molecules.

In this sense, spectroscopic studies of low-mass objects ($M < 0.07\ M_\odot$) recently discovered in the very near solar neighborhood provide a unique opportunity for investigating such problems. No classification criteria analogous to those used for earlier-type (A–M) stars have thus far been developed for L dwarfs. Even in the M-dwarf case, the situation is not as straightforward as it seemed several years ago. The optical spectral energy distributions of M dwarfs[1] are known to be dominated by TiO and VO absorption bands [1]. The class of low-mass dwarfs includes both stars in the proper sense of the word (VB8, VB10, PPL1, and others [2, 3]) and (young) brown dwarfs—substellar objects with masses below a certain threshold ($M < 0.065 M_\odot = 65 M_J$, where M_J is the mass of Jupiter): Teide 1, Calar 3 [4], and PPL 15 [5]. It is currently believed that there is no hydrogen burning in the interiors of brown dwarfs: they first radiate energy released during their gravitational contraction, then slowly cool over cosmological time scales. Therefore, strictly speaking, many brown dwarfs should be classified as subgiants—the time scales for their gravitational contraction and cooling exceed the lifetime of our Galaxy [6]. Rebolo *et al.* [7] suggested a so-called "lithium test" for identifying brown dwarfs: their low temperatures ($T \le 2.51 \times 10^6$ K) prevent this element from being burned in the interiors of brown dwarfs, so that these objects should exhibit very strong lithium absorption lines, which indeed have been observed in the spectra of a number of low-mass objects [4, 5].

The other known classes in the lower part of the Hertzsprung–Russell diagram are L and T dwarfs. Note that the IAU has not yet adopted the classifications "L dwarf" and "T dwarf." We use them here only to refer to the spectral types of objects whose optical spectra differ substantially from those of M dwarfs.

L dwarfs. This family of objects (Kelu1, GD 165B, BRI 0021–0214, DenisP J1228–1547, DenisP J0205–1159, and others [8]) was discovered in the past three to four years. The optical spectra of L dwarfs are characterized by the presence of resonance lines of the alkali elements K I, Na I, Rb I, and Cs I. The intensities of the K I and Na I resonance lines substantially exceed those of the absorption lines of other metals, and determine to a large degree the spectral energy distribution profiles of L dwarfs [9–11]. Compared to those for M dwarfs, the TiO and VO molecular bands in the spectra of L dwarfs are much weaker, or even completely absent. However, CrH and FeH absorption bands are present in the red part of the spectrum [12]. The dividing line between M and L dwarfs is usually drawn near $T_{\rm eff} \approx$ 2200 K [13]. L dwarfs include both stars in the proper sense of the word and brown dwarfs. Identifying the brown-dwarf subset within the L-dwarf family is by no

[1] In this paper, we refer to spectra in the wavelength interval λλ600–900 nm as "optical."

means an easy task, because of problems applying the "lithium test" to these objects [19].

T dwarfs. When its mass is below $35M_J$, an object no longer exhibits K I and Na I resonance lines in its spectra. The formation of the optical spectra of such low-mass bodies with $T_{\rm eff} < 1000$ K (Gl 229B [14], objects from the SDSS [15, 16] and 2MASS [17, 18] surveys) should be dominated by the absorption and/or scattering of radiation by dust grains [19]. Essentially, the physical conditions in the atmospheres of these objects approach those in planetary interiors; however, the observed Cs I and Rb I absorption lines indicate that T-dwarf atmospheres contain an inversion layer, i.e., a photosphere in the classical sense.

Of course, this classification is only preliminary. However, the introduction of new spectral types in the near future (for the first time since the development of the Harvard classification [20]) to describe the family of low-mass objects considered here seems quite possible.

In this paper, we will be interested only in the spectra of L dwarfs. As noted above, the spectral energy distributions of these objects in the optical (λλ500–850 nm) are dominated by the Na I (λλ588.995 and 589.592 nm) and K I (λλ766.491 and 769.897 nm) resonance doublet absorption lines, whose observed wings are extremely broad (hundreds and thousands of Å!). We model the formation of saturated potassium and sodium resonance-doublet lines in the atmospheres of L dwarfs, and compare the computed and observed optical spectra over a wide wavelength interval (λλ580–900 nm). This paper is based on the same observational data on the spectra of L dwarfs as in our previous work [19].

2. COMPUTATIONAL PROCEDURE

We computed the L-dwarf theoretical spectral energy distributions[2] using the WITA31 version of the WITA5 code [9, 12]. We used Tsuji's [22] model atmospheres to determine the conditions for the dust–gas segregation phase, when the mean radius of the dust grains r_d exceeds the threshold value r_c corresponding to a thermodynamical equilibrium of the dust–gas transition. Following Tsuji [22], we refer to these models as C model atmospheres, to distinguish them from A model atmospheres, which do not include dust at all, and B model atmospheres, where $r_d = r_c$. We computed our synthetic spectra for the solar elemental abundances of [23] in the framework of classical approximations—LTE, a plane-parallel geometry, neither sources nor sinks of energy—taking into account the ionization–dissociation equilibria of about ≈100 species. Overall, our description of the state of matter in the atmospheres of L dwarfs did not differ from that in [10].

[2] For the sake of simplicity, we use the term "synthetic spectra" as a synonym for "theoretical spectral energy distributions."

A number of particular effects must be taken into account when computing L-dwarf spectra, as discussed below.

Dust formation. The high pressures and low temperatures in the atmospheres of L dwarfs favor gas–dust transitions for a number of molecules; i.e., formal solution of the system of ionization–dissociation equations for these molecules yields partial pressures P_i exceeding the corresponding saturation pressures P_s. We adopted the P_s values as functions of temperature from [24], and substituted the saturation pressures P_s for P_i values exceeding P_s [10]. Naturally, this enables us to estimate only upper limits for decreases in the concentrations of individual atoms and molecules in the atmospheres of L dwarfs. Therefore, a special algorithm to describe the molecular bands observed in the atmospheres of L dwarfs was implemented in the WITA5 program. Namely, the concentrations of the ith component, n_i^e, for the solution of the system of ionization–dissociation equilibrium equations are reduced to ensure the best agreement between theory and observations: $n_i = n_i^e R_i$. We assumed that $0 < R_i < 1$ and that R_i for the ith component did not change with depth in the atmosphere. Naturally, this approximation proved inadequate in a number of cases (see below). On the other hand, its simplicity enabled the numerical computations to be performed.

Additional (dust) opacity. As was shown by Tsuji [25], dust-grain formation in the atmospheres of stars with $T_{\rm eff} < 2600$ K increases the temperature of the outer layers of their atmospheres. In addition, the formation of dust grains involves vanadium and titanium atoms, so that the blanketing effect due to VO and TiO molecular-band absorption is reduced [26]. More recent computations have shown that these effects become especially important in the atmospheres of L dwarfs [19], where the temperature structure of the atmosphere responds to blanketing-effect variations due to the turning on of additional opacity sources associated with the absorption and/or scattering of light by dust grains. The computed synthetic spectra prove to be very sensitive even to small opacity variations. As in [19], we assume that this additional opacity can be fitted by the formula $a_\nu = a_0(\nu/\nu_0)^N$, and determined a_0, ν_0, and N by comparing the observed and computed optical-spectra profiles. Note that the values for N thus determined lie in the interval from zero to four. If we assume that the additional opacity is due to the scattering of radiation by dust grains (aerosols), then $N = 0$ and $N = 4$ correspond to the extreme cases of "white" and Rayleigh scattering, respectively.

3. ATOMIC ABSORPTION LINES IN THE SPECTRA OF L DWARFS

The low temperatures in the atmospheres of L dwarfs *a priori* prevent substantial degrees of ionization of alkali elements, with their low ionization potentials. For

this same reason, most alkali atoms are in their ground states, implying that primarily the resonance lines of neutral atoms—Na I, K I, Rb I, and Cs I—should be observed in the spectra of L dwarfs [9–11]. Some L-dwarf spectra also exhibit absorption lines of the Li I resonance doublet (λ670.8 nm [19]).

All these lines are produced in 2*s*–2*p* transitions. The structure of alkali atoms is hydrogen-like, having an outer electronic envelope with a single valence electron lying above filled inner shells, whose number increases with *Z*. Note the following circumstances.

(1) The effects of splitting into sublevels for the $np^2\ P_{1/2}$ and $np^2\ P_{3/2}$ terms of alkali elements increase with atomic number *Z*. Thus, the lines of the Li I resonance doublet are separated by $\Delta \approx 1.7$ cm^{-1}, whereas the corresponding separations for Rb I and Cs I are 238 and 556 cm^{-1}, respectively [27]. Naturally, such substantial values for Δ imply that the corresponding doublet components form well-separated absorption lines in the observed spectrum.

(2) The ground states of neutral atoms are not broadened; all broadening of the resonance lines is due to broadening of the quantum sublevels of the second term, $np^2\ P$ (which, in the case of alkali elements, is closest to the ground state).

Since we are modeling very strong absorption lines, we consider it appropriate to describe the corresponding computational technique in more detail. We take into account several line-broadening mechanisms for neutral atoms, the first being Doppler broadening due to the thermal motions of particles. In the absence of large anomalies in the velocity distribution, this mechanism is restricted to the line cores.

Second, we allow for intrinsic broadening of the absorption lines of neutral atoms and broadening due to collisions with other particles. We used the technique implemented by Kurucz [28] in his ATLAS6 program, which was subsequently modified by Pavlenko and Shavrina [29] to adapt it to the WITA code. The code takes into account the total effect on the profile of each line due to various types of interactions: $\gamma = \gamma_2 + \gamma_4 + \gamma_6$, where γ_2, γ_4, and γ_6 describe intrinsic, Stark, and van der Waals broadening, respectively. In a transition between two bound atomic states, the uncertainty of the transition frequency, or the intrinsic line width, is:

$$\gamma_2 = 0.22/\lambda^2, \tag{1}$$

where λ is the wavelength in cm. The Stark broadening is:

$$\gamma_4 = 13.595 N_e/(E_{\text{ioniz}} - E_{\text{up}}), \tag{2}$$

where E_{ioniz} and E_{up} are the upper-level ionization and excitation potentials, respectively, and N_e is the electron density. When computing γ_6, Kurucz [28] included the total effect of hydrogen and helium atoms and hydrogen molecules. We have in the approximation of Unsold [30]:

$$\gamma_6 = (n(\text{H}) + n(\text{He})\gamma_6(\text{He})/\gamma_6(\text{H}) + n(\text{H}_2)\gamma_6(\text{H}_2)/\gamma_6(\text{H}))\gamma_6(\text{H}), \tag{3}$$

where $\gamma_6(\text{He})/\gamma_6(\text{H}) = 0.42$, $\gamma_6(\text{H}_2)/\gamma_6(\text{H}) = 0.83$, and $\gamma_6(\text{H}) = 17.0 C_6^{2/5} v_t^{3/5} n(\text{H})$. Detailed computational formulas for $\gamma_6(\text{H})$ can be found in a number of monographs and original papers [28, 31, 32].

Based on their modeling of the Na I λλ8194.79, 8194.8, 28183.25 nm subordinate triplet in the spectra of an M dwarf, Pavlenko *et al.* [33] showed that Eq. (3) overestimates the effect of H_2 molecular broadening on the observed line profiles. More realistic results can be obtained with the formula

$$\gamma_6 = (n(\text{H}) + n(\text{He})\gamma_6(\text{He})/\gamma_6(\text{H}))\gamma_6(\text{H}). \tag{4}$$

In the spectra of M dwarfs, this triplet is appreciably blended by molecular lines. It is therefore of interest to test the conclusions of Pavlenko *et al.* [33] by modeling the spectra of L dwarfs, in which, as noted above, the wings of the resonance doublets extend virtually over the entire optical wavelength interval (see Section 4.1).

The opacity in late-type dwarfs decreases with decreasing temperature at the photospheric level. As a result, the photospheres shift toward regions with higher gas pressures. The comparison of a model atmosphere for the Sun with that for an L dwarf with $T_{\text{eff}}/\log g = 1200/5.0$ shows that the gas pressure P_g at the lower boundary of the HOLMU solar model atmosphere [34] corresponds to the P_g values in the upper layers of the L-dwarf model atmospheres considered. At the same time, the temperatures in the atmospheres of L and M dwarfs at the level where the lines form are substantially lower (by several thousand degrees) compared to solar-type stars.

It follows that alkali absorption lines in the atmospheres of L dwarfs form inside a dense shell of relatively cool matter consisting of neutral atoms, molecules, and, as has recently been elucidated, dust grains [25]. Note that, in this case, the surface gravity for the solar atmosphere differs only slightly from that for the L dwarf ($\log g = 4.44$ and 5.0, respectively), implying that the difference between the gas pressures at the photospheric layers of the two stars is due to the masses ($m \approx P_g/g$) lying above them.

Compared to the solar atmosphere, the changes in the roles of various broadening mechanisms affecting the lines of neutral metals in L-dwarf atmospheres can be qualitatively assessed as follows. Van der Waals broadening is the dominant mechanism for atomic absorption lines in the atmospheres of solar-type stars. Broadening mechanisms associated with the electric fields of ions and electrons become important only at the lower photospheric boundary [23, 29], and intrinsic broadening is significant only at low densities. Natu-

rally, the contributions of intrinsic and Stark broadening can only decrease with decreasing $T_{\rm eff}$, so that van der Waals broadening should be the dominant effect in the alkali absorption lines in the atmospheres of L dwarfs.

3.1. Absorption-Coefficient Profile of a Spectral Line

We fitted the line absorption-coefficient profiles using Voigt (Harting) functions $H(a, v)$ with the parameters $a = \gamma/(4\pi\Delta\nu_D)$ and $v = \Delta\nu/\Delta\nu_D$, where $\Delta\nu_D = (v_t^2 + 2RT/\mu)^{1/2}$ is the Doppler line halfwidth determined by the velocity dispersion. We set the microturbulence velocity equal to 2 km/s; it was this parameter that primarily determined $\Delta\nu_D$, since, due to the low temperatures, the amplitudes of thermal motions are very low in the atmospheres of L dwarfs.

The a values computed for the resonance potassium and sodium lines with allowance for broadening due to H and He atoms and H_2 molecules can be enormously high [$a > 10$ and 100 at the lower photospheric boundaries of 2000/5.0 and 1200/5.0 L dwarfs, respectively (Fig. 1)]. The same quantities computed without taking into account collisions with hydrogen molecules are lower by a factor of about 10. However, even in this case, the absorption-line broadening is much stronger in L dwarfs than in solar-type stars, where $a = 0.001$–0.1.

To first approximation, the variation of a with depth in the atmospheres of L dwarfs can be described by a power law. This can easily be explained by the fact that the broadening of alkali lines is primarily determined by hydrogen and helium atoms [and hydrogen molecules (?)], whose vertical density profiles can also be described by power laws.

3.2. The Correction Factor E

As noted above, we computed the damping constant γ_6 using the approximation of Unsold [30]. It is well known that quantum-mechanical computations yield γ_6^q values that differ somewhat from γ_6: to first approximation, $\gamma_6^q = E\gamma_6$ and $1 < E < 2$ for most of the lines.

For obvious reasons, quantum-mechanical computations of E are very difficult to perform. However, similar correction factors E for alkali lines have been derived in a number of other studies [23]. For example, the theoretical computations of Andretta *et al.* [35] yielded $E = 1.4$–1.8 for alkali lines, though we note that they used a somewhat different technique to estimate γ_6.

Unfortunately, laboratory measurements of E are even more uncertain, mainly due to problems in reproducing the conditions of stellar atmospheres. However, on the whole, the results of laboratory analyses agree with theoretical computations [23, 36].

Many authors consider it more appealing to determine the correction factor E empirically via the interpretation of absorption lines in the solar spectrum, especially since many parameters ($T_{\rm eff}$, $\log g$, and heavy-element abundances) are known with rather good accuracy in this case. On the other hand, there remains some uncertainty in the determination of model atmospheres and velocity fields [23] (see next section).

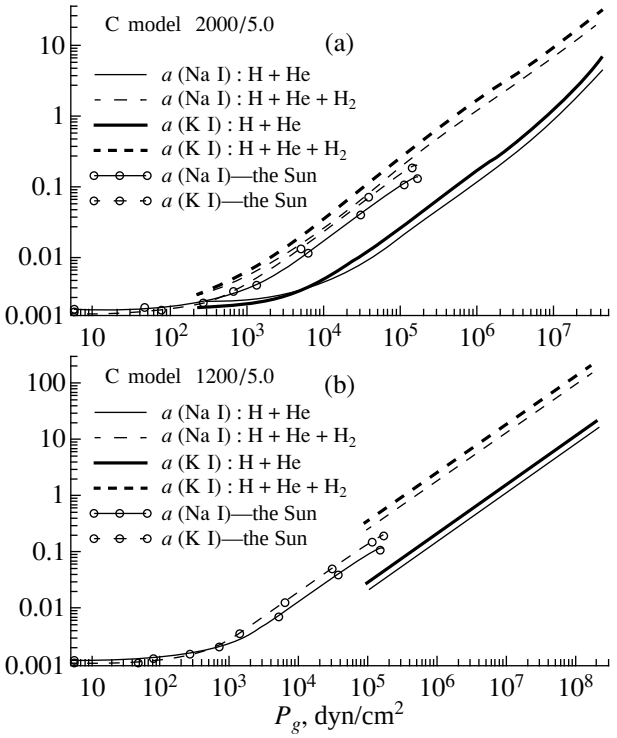

Fig. 1. Damping parameters a for the resonance absorption lines computed using the HOLMU solar model atmosphere [34] and C-type L-dwarf model atmospheres (a) 2000/5.0 and (b) 1200/5.0 of Tsuji [22].

3.3. Na I and K I Resonance Lines in the Solar Spectrum

We followed the usual procedure and tested our technique for computing the profiles of strong Na I and K I resonance lines by comparing our synthetic spectra for the Sun with observed solar spectrum [37]. Our profiles of the Na I λλ588.995, 589.592 nm doublet computed using the HOLMU solar model atmosphere [34] indicate that the observed line wings can be described by $E = 2 \pm 0.5$ (Fig. 2). On the whole, the blending of the lines of this doublet was much weaker than the blending of the resonance Na I doublet. The wings of the sodium lines are rather well defined in the observed spectrum.

Unfortunately, the lines of the K I λλ766.491, 769.897 nm resonance doublet in the solar spectrum are much weaker, and their wings are more blended. Moreover, the lines contributing to the blending are even stronger than in the case of the Na I doublet, making the determination of the optimal E value problematic (Fig. 2). However, Takeda *et al.* [38] estimated $E = 10$ for the

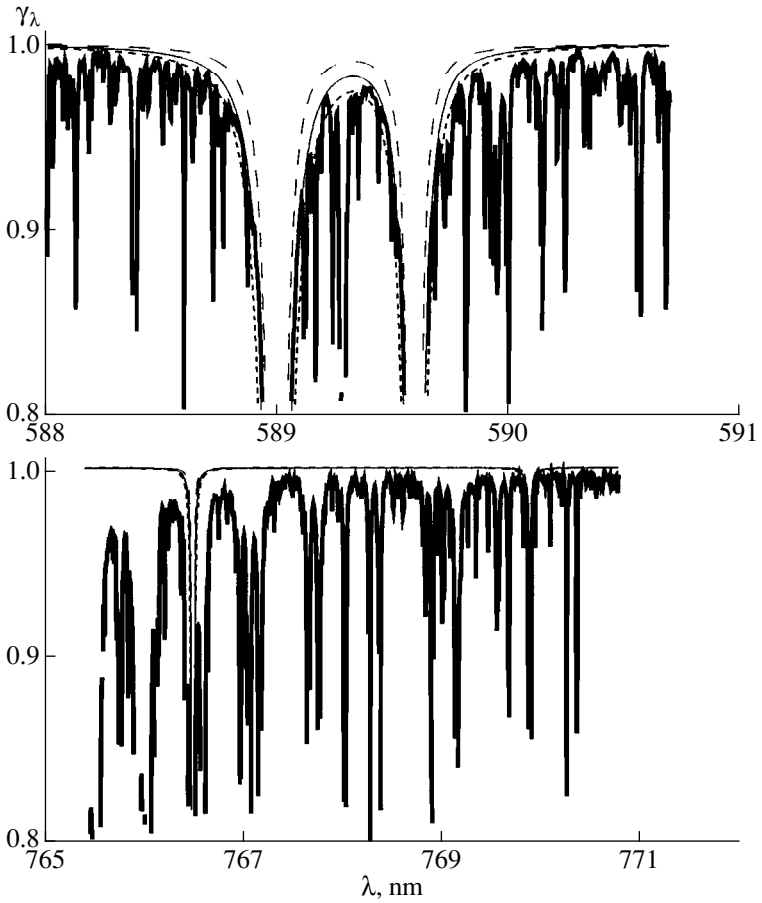

Fig. 2. Comparison of the computed profiles of the Na I and K I resonance doublets for the HOLMU [34] solar model atmosphere with the observed line profiles in the solar spectrum [37]. The solid bold line shows the observed spectrum. The long-dashed, solid, and short-dashed thin lines show the results of computations with E = 1, 2, and 3, respectively.

doublet line at λ 769.897 nm. In our opinion, this is clearly an overestimate. The structure of the radiation transitions and main parameters of potassium and sodium atoms are very similar, so that the resonance lines of these atoms are unlikely to have very different E values.

4. RESULTS

The gas pressure at the absorption-line formation depths in L-dwarf atmospheres can reach $P_g \sim 10^6$ dyn/cm^2 and more, exceeding P_g in the Earth's atmosphere. This cannot but affect the formation of saturated absorption lines.

4.1. Relative Importance of Broadening due to Hydrogen Molecules

The atmospheres of solar-type stars are dominated by atomic hydrogen: in this case $n_H > n_{He} > n_{H_2}$, making the estimation of the contribution of molecular hydrogen to the broadening of metal absorption lines very difficult.

The situation changes at lower T_{eff}. Our numerical computations show that, in L-dwarf atmospheres with $T_{eff} < 2000$ K, hydrogen exists mainly in the form of H_2 molecules: $n_{H_2} > n_{He} > n_H$. According to formula (3), in this case, line broadening should be dominated by the effect of interactions with hydrogen molecules. We performed a number of numerical simulations in order to determine the contributions of the various alkali line-broadening mechanisms. In particular, we computed several optical spectra for the L dwarf Kelu 1. We chose this L dwarf because various authors [19, 39] have reported fairly consistent effective temperatures for this star (~2000 K). It follows from general considerations that the surface gravity in the atmosphere of Kelu 1 cannot differ too much from 10^5 [19]. Thus, in the case of Kelu 1, we have a number of physical constraints that can be applied when selecting the input parameters, which decreases substantially the uncertainty in the results obtained [19].

Figure 3 compares the computed optical spectral energy distributions for Kelu 1 with observed spectra. We computed synthetic spectra for two cases: with the

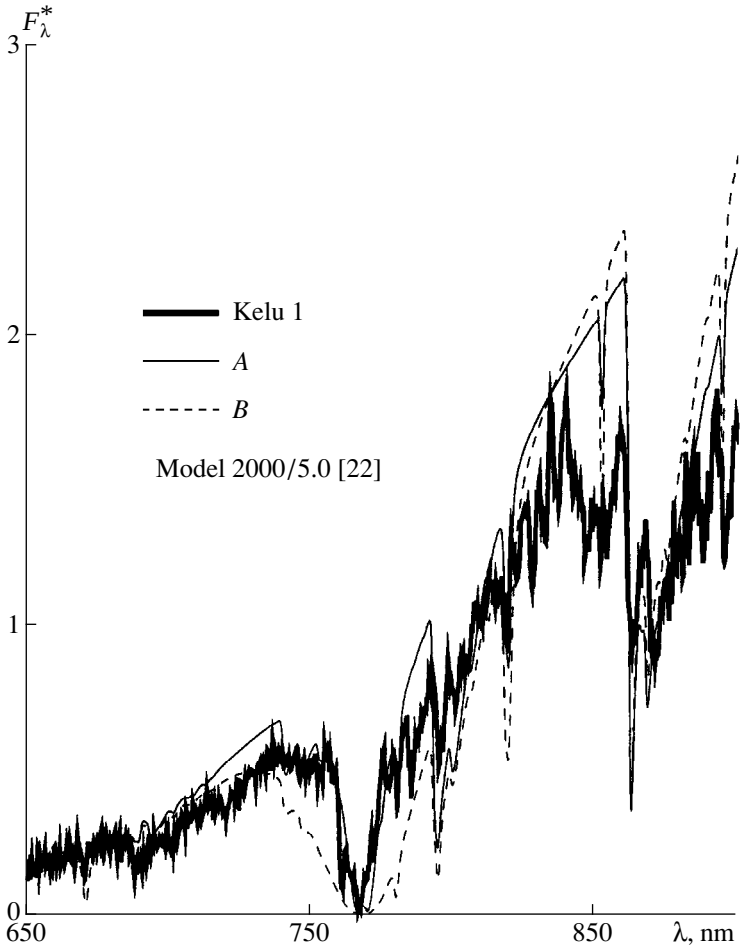

Fig. 3. Comparison of the observed spectral energy distribution of Kelu 1 with the spectral energy distribution computed without (curve *A*) and with (curve *B*) allowance for the absorption-line broadening attributable to the interaction with hydrogen molecules.

damping constants for the K I and Na I resonance-doublet lines determined both with and without allowance for line broadening due to hydrogen molecules (curves *A* and *B* in Fig. 3, respectively). As in our previous paper [19], our computations included the additional extinction $\sigma_\lambda = a_0(\lambda_0/\lambda)^N$. Figure 3 shows the computation results for $a_0 = 0.03$ and $N = 4$. We then decreased the VO and TiO concentrations by factors of 12 and 100, respectively, throughout the entire depth of the model atmosphere. The anomalously low intensities of the bands of these molecules clearly indicate dust-grain formation processes involving Ti and V atoms that have not been taken into account.

We then normalized the observed and computed spectra to the same flux at λ834.4 nm.[3] Even the relatively simple model adopted here yielded a fully satisfactory description of the observed spectral energy distribution for Kelu 1 (see also [19]). On the whole, the shape of the optical spectrum of this star is determined by the wings of the Na I λλ5889.95, 5895.92 nm and K I λλ7664.91, 7698.97 nm strong resonance doublets.

Here, we are primarily interested in comparing the observed and computed profiles of the K I resonance doublet. As is evident from Fig. 3, taking into account van der Waals broadening due to the interaction of K I atoms with H_2 molecules yields synthetic Kelu 1 spectra with implausibly broadened profiles (i.e., they are inconsistent with the observations). At the same time, the profiles of the K I λλ766.491, 769.897 nm resonance doublet computed without allowance for van der Waals broadening—i.e., based on Eq. (4), which includes interactions with H_2 molecules—agree well with the observations.

The resonance absorption lines of alkali elements in the spectra of L dwarfs become stronger with decreasing effective temperature. Figure 4 compares the computed optical spectral energy distributions for the L dwarf DenisP J0205–1159 with its observed spectra. In this case, as for Kelu 1, our computations included the effects of van der Waals broadening as estimated using Eqs. (3) and (4).

[3] We verified that our choice of the wavelength used to normalize the observed and computed energy distributions did not appreciably effect the principal results.

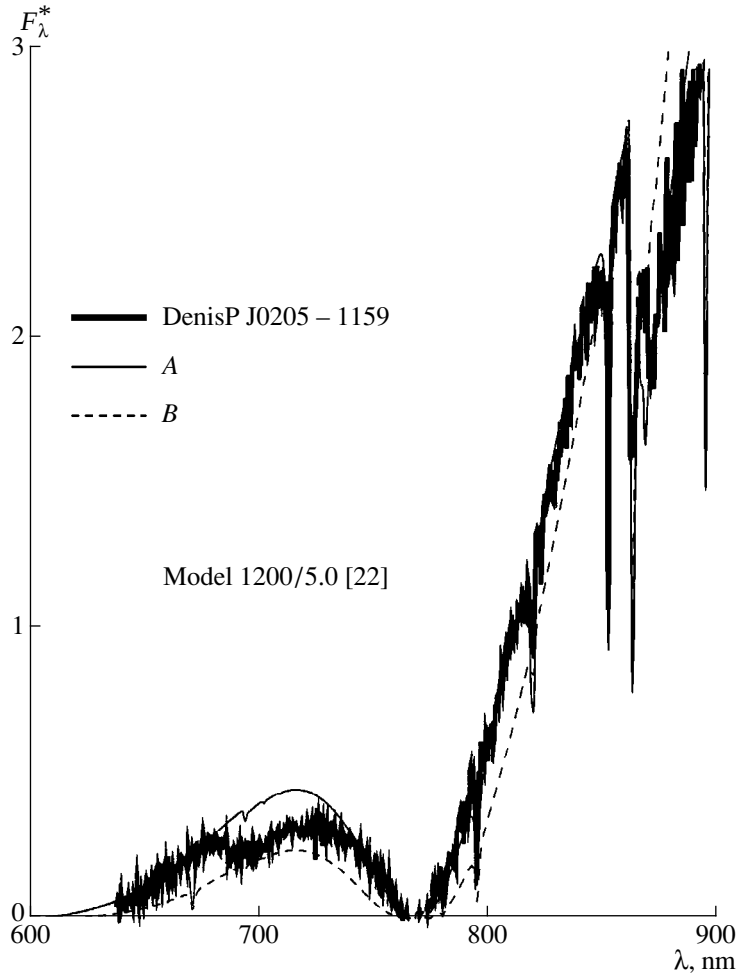

Fig. 4. Same as Fig. 3 for DenisP J0205–1159.

Again, the results using Eq. (4) are in better agreement with the observations. Note that the spectrum of this L dwarf forms at lower temperatures and, consequently, at higher pressures. Molecular bands that are prominent in the spectrum of Kelu 1 disappear almost completely in that of DenisP K0205–1159. Therefore, our computations did not include TiO and VO band absorption; i.e., we assumed that the concentrations of these molecules were insignificant, since the Ti and V atoms are bound in dust grains.

4.2. Equivalent Widths of K I and Na I Resonance Lines

Figures 3 and 4 show the *normalized* spectral energy distributions for Kelu 1 and DenisP J0205–1159. Naturally, these results give only a rough idea about the *absolute intensities* of the observed absorption lines.

As a rule, absorption-line strengths are formally estimated by analyzing their equivalent widths, and such analyses require computing spectra in terms of residual intensities. We performed such computations for two C model atmospheres of Tsuji [22]: 1200/5.0 (the case of DenisP J0205–1159) and 2000/5.0 (Kelu 1) both for the absorption lines taken separately and for their blend (Figs. 5 and 6).

Let us note here a number of important points.

(1) The observed lines of the K I and Na I resonance doublets appear as *single* absorption lines in the spectra of L dwarfs. Here, we deal with physical blending: two neighboring absorption lines become strong enough to form a single blend.

(2) The Na I resonance doublet is appreciably stronger than the K I resonance doublet, since the abundance of sodium in the solar atmosphere ($\log N$ (Na) = –5.72) is much higher than the abundance of potassium ($\log N$ (K) = –6.92).[4]

(3) At low effective temperatures ($T_{\rm eff} < 2000$ K), the lines of the K I λλ766.491, 769.897 nm resonance doublet are actually located in the wing of the blend of the Na I λλ588.995, 589.592 nm resonance line.

[4] On a scale with $\Sigma N_i = 1$.

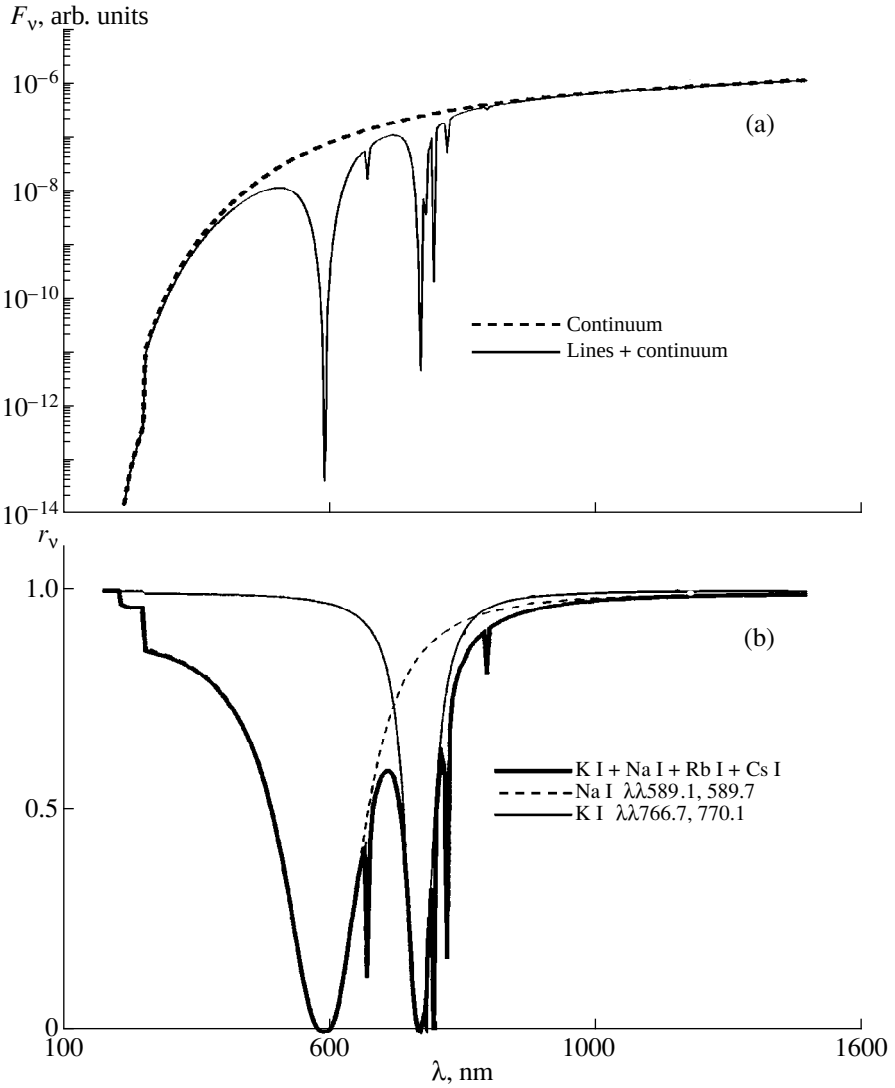

Fig. 5. Computed fluxes for (a) L-dwarf C model atmosphere 2000/5.0 and (b) alkali absorption lines (in the residual intensity spectrum) for the same model atmosphere. Separate profiles are shown for each line and their sum.

The formally computed equivalent widths of the lines of the Na I and K I resonance doublets can be enormously high: 6640 and 2500 Å for C model atmosphere 1200/5.0 and 3550 and 880 Å for C model atmosphere 2000/5.0, respectively; it would be appropriate to measure such intensities in kiloangstroms. These are evidently the strongest absorption lines that have been observed in the spectra of astronomical objects.

4.3. Formation of L-Dwarf Spectra

The visible spectral energy distribution of L dwarfs is thus to a large extent determined by absorption in neutral potassium and sodium resonance lines. Their wings form a sort of pseudo-continuum for weaker absorption lines and even molecular bands. Figure 7 shows a series of theoretical spectra computed for L-dwarf C model atmosphere 1200/5.0. For the sake of simplicity, the absorption bands of only two molecules are shown in Fig. 7: CrH and VO.

If there were no superstrong sodium and potassium absorption lines, the optical spectra of L dwarfs would consist solely of absorption bands of CrH and other molecules, with their intensities dependent only on the decrease of the concentrations of absorbing particles due to partial binding of atoms in dust grains. Figure 7 shows VO and CrH molecular bands computed for the case of chemical equilibrium [10] (i.e., with allowance for the decrease of the VO concentration to levels determined by the thermodynamical equilibrium of the gas–dust phase transition).

The situation changes if we take into account absorption due to the K I and Na I resonance lines. The

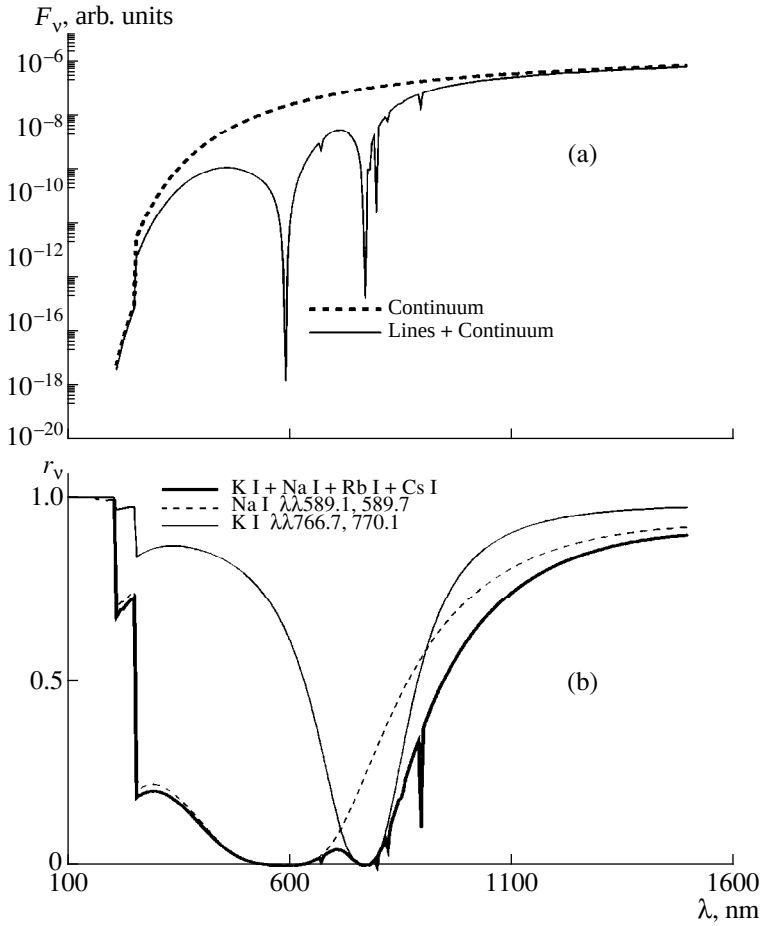

Fig. 6. Same as Fig. 5 for model atmosphere 1200/5.0 (the case of DenisP J0205–1159).

molecular bands at $\lambda < 800$ nm are virtually swamped by absorption in the wings of these lines. Of special interest is the fact that the positions of the heads of the molecular bands of VO [the (0.1) band of the $B^4\Pi_{(r)} - X^4\Sigma^-$ system] and CrH [the (0.0) band of the $A^6\Sigma^{(+)} - X^6\Sigma^{(+)}$ system] virtually coincide, with the intensities of these bands decreasing toward the red. This, in particular, means that the λ 860 nm feature in the spectra of late L-dwarfs can be interpreted equally well as either VO or CrH absorption (see Fig. 8 for DenisP J0205–1159, $T_{\rm eff}$ = 1200 K [19]). Other bands of these molecules are barely visible at shorter wavelengths in the spectrum of DenisP J0205–1159, making the final identification of the observed molecular bands somewhat difficult.

The situation simplifies somewhat in the case of Kelu 1 (Fig. 3). The spectrum of this L dwarf exhibits a number of relatively weak VO bands. In the process of reproducing their intensities in the observed spectrum, we obtain a number of natural restrictions on the adopted molecular absorption model. Thus, it seems quite appropriate to assume that the model should reproduce the relative intensities of individual bands in the object's spectrum. Strong VO bands are located at λλ640 and 680 nm, and the intensity of the 640 nm band can be described by $R_{\rm VO} = 0.001$. However, in this case, the (0.0) band of the $B^4\Pi_{(r)} - X^4\Sigma^-$ system appears as a very weak absorption feature in the computed spectrum. On the other hand, including the CrH-band absorption makes it possible to fit the profile of the 860 nm band quite satisfactorily. Thus, the 860-nm absorption in the spectrum of Kelu 1 (and, consequently, of L dwarfs with lower $T_{\rm eff}$) is due to the (0.0) band of the $A^6\Sigma^{(+)} - X^6\Sigma^{(+)}$ system of the CrH molecule.

5. DISCUSSION

We have synthesized the spectra of L dwarfs using fairly simple models. Note that the observed spectra of the L dwarfs became available only quite recently. However, there is no doubt that the mechanisms for the formation of L-dwarf spectra differ from those for the spectra of stars with higher effective temperatures. The extremely low temperatures and high pressures in L-dwarf atmospheres mean that we are actually dealing with a cross-disciplinary field between the physics of stellar and planetary atmospheres.

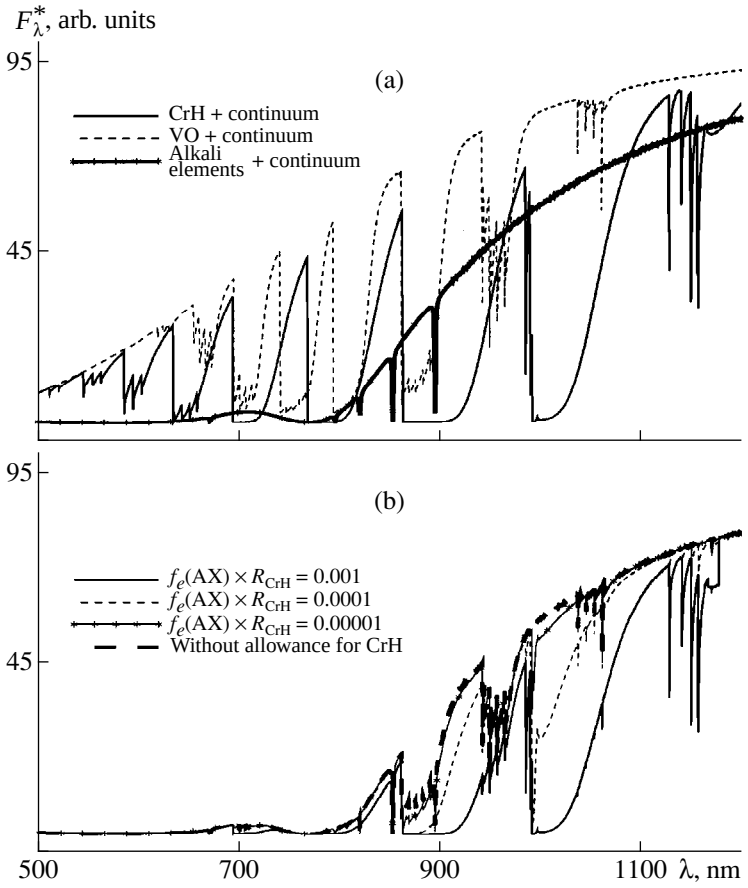

Fig. 7. Synthetic spectra computed for C model atmosphere 1200/5.0 taking into account (a) continuum absorption in the CrH and VO bands only and (b) absorption in the K I and Na I resonance doublets. The results of computations for several f_eR_{CrH} values are shown, where f_e is the oscillator strength for the $A^6\Sigma^{(+)}$–$X^6\Sigma^{(+)}$ system of the CrH molecule.

5.1. Line-Broadening Mechanisms

We analyze here the formation of extremely intense alkali absorption lines. The question naturally arises of whether classical techniques can be applied to model such spectra. In the case of L dwarfs, we are faced for the first time with the problem of modeling optical spectra with a relatively simple structure, formed as a result of absorption in the lines of the resonance doublets of two alkali elements: K I and Na I. Naturally, this imposes special requirements on the reliability of the technique used to compute the corresponding line profiles.

We found the hypothesis that atomic line broadening can be satisfactorily described in terms of adiabatic shock theory [32] to be fully justified in this case, especially since we can now for the first time observe atomic-line wings several hundred and even several thousand angstroms from their core wavelengths. In the spectra of L dwarfs, we "see" atomic levels pressure-broadened on scales comparable to the intra-atomic scale. At the same time, the line profiles can be modeled quite satisfactorily using fairly simple concepts and approaches.

However, observations of L-dwarf spectra pose a number of new problems that demand the testing and modification of existing modern astrophysical tools. The techniques used in this paper were adopted from methods used for traditional stellar astrophysics. The applicability of at least of some of these to the synthesis of L-dwarf spectra is questionable. The chief problem seems to be overestimation of the role of atomic-line broadening due to hydrogen molecules. We found that the line profiles computed without allowance for broadening due to hydrogen molecules gave the best agreement with the observations. However, this might be due to (1) uncertainties in the formulas used to compute line broadening due to interactions between neutral metal atoms and hydrogen molecules and (2) peculiarities (anomalies) of the chemical equilibrium of the atoms and hydrogen molecules in L-dwarf atmospheres. However, this latter circumstance seems less plausible. The H_2 molecule is currently well understood, and the corresponding chemical-equilibrium constants are known rather accurately. On the other hand, the line wings computed taking into account only broadening by hydrogen atoms reproduce the observations fairly well, which can be

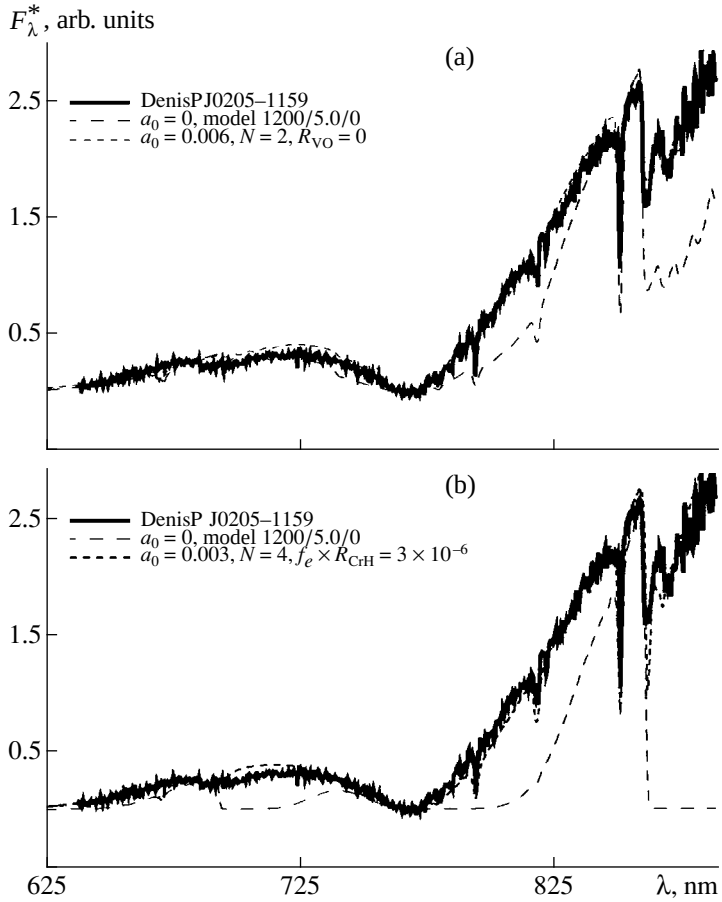

Fig. 8. Comparison of the observed optical spectra of DenisP J0205–1159 with the spectra computed taking into account (a) VO and (b) CrH band absorption.

interpreted as (indirect) corroboration of our chemical-equilibrium computations for L-dwarf atmospheres.

At the same time, we had to adopt a number of (by no means obvious) hypotheses and what seems likely to be non-ideal input data (model atmospheres, opacity sources, etc.), whose applicability remains to be verified. This is certainly true of the correction factor E for the van der Waals damping constant. In this paper, we determined E values for the K I and Na I resonance doublets from an analysis of the solar spectrum. Note that atomic-line broadening in the solar atmosphere depends primarily on interactions with hydrogen atoms. However, at lower effective temperatures, neutral helium atoms and hydrogen molecules become the dominant components in terms of numbers of particles. In principle, it is precisely these particles that are responsible for absorption-line broadening in the case considered. Therefore, strictly speaking, L-dwarf spectra cannot be computed using the E values for the absorption lines in the spectra of solar-type stars. The situation is further exacerbated by the fact that the K I and Na I line profiles depend strongly on both $T_{\rm eff}$ and $\log g$ [19]. The main factor hindering the determination of E from analyses of L-dwarf spectra is, therefore, the uncertainties in $T_{\rm eff}$ and $\log g$ for these objects.

5.2. Model Atmospheres

We have used Tsuji's [22] model atmospheres computed applying the usual classical assumptions. However, such assumptions as LTE, a lack of opacity sources and sinks, and energy transport only via radiation transfer and convection are clearly not fully justified. Problems arise because the dust component must be taken into account at low temperatures and high pressures, affecting both the thermodynamic properties of the matter in the atmospheres of L dwarfs and their structures. Possible manifestations of these effects include inhomogeneity (stratification) in the heights of molecular concentrations and the presence of layers of dust clouds with different optical properties. Inhomogeneity in the vertical profiles of the molecular distributions has already shown up in the case of Kelu 1: the intensities of different bands of the same molecules cannot be described using a homogeneous model.

We treated the decrease of molecular concentrations due to the binding of molecules in dust grains using

very simple hypotheses. Namely, we reduced the partial pressures of individual molecules to values corresponding to the gas–dust phase transition. Naturally, the true nature of dust-grain formation could be much more complex. On the other hand, we must bear in mind that, in this case, the dust grains form in the convection zone. Like M dwarfs, L dwarfs possess powerful convective envelopes, which can transport dust grains deep into the atmosphere, where they are efficiently destroyed.

The description of the properties of the dust component in L-dwarf atmospheres poses a fundamentally new problem. In this case, we must describe the properties of dust grains formed in a relatively cool plasma with C/O < 1; i.e., that is oxygen-rich. A consistent approach should include a full set of phase transitions involved in the formation of multi-atomic dust grains. Unfortunately, it is currently impossible to adequately allow for an entire sequence of all possible (and, strictly speaking, time-dependent) chains of chemical reactions.

All our computations involved model atmospheres with normal (i.e., solar) chemical composition; i.e., we assumed that L dwarfs belong to the Galactic disk population. This assumption seems quite natural, since we are modeling the spectra of objects in the solar neighborhood. On the other hand, L dwarfs could include low-mass stars born in early stages of the Galaxy's evolution; i.e., objects with metal-deficient atmospheres. Note that the evolutionary time scales for L dwarfs are comparable to the cosmological time scale. At the same time, it follows from general considerations that the kinematic parameters of these old L dwarfs, which are actually halo stars, should differ appreciably from those of disk L dwarfs. On the whole, the concept of the chemical composition of stellar atmospheres acquires a somewhat different meaning in the case of L dwarfs. In this case, analyses of atomic lines must take into account the decrease in the numbers of atoms due to their binding in both molecules and dust grains. We intend to analyze the ionization–dissociation equilibrium of alkali elements in a separate paper.

5.3. Molecular Opacity

We were not able to describe the profiles of individual bands of the "traditional" M-dwarf molecules VO and TiO observed in the spectra of L dwarfs in terms of the adopted physical model. The evident discrepancies between the computed synthetic spectra and the observed spectrum of Kelu 1 at λλ790, 850 nm can naturally be explained by the fact that the real situation differs from the model adopted here. As noted above, L-dwarf atmospheres can show the effects of both the stratification of molecular distributions and the formation of cloud-like gas–dust structures. This is reflected, in particular, by the fact that the spectrum of Kelu 1 exhibits a fairly strong feature at λλ840–855 nm, which is apparently formed by the bands of the ϵ subsystem of TiO ($E^3\Pi - X^3\Delta$), whereas other band systems of this molecule are relatively weak or even nonexistent.

An alternative interpretation is that some processes in L-dwarf atmospheres drive the level populations into a non-equilibrium state. The point here is that all our computations were performed assuming LTE. However, low electron temperatures and electron densities together with the presence of a dust component give rise to a radically new pattern for processes involving the radiation field. Unfortunately, the entire set of all possible processes cannot be analyzed in detail in the framework of this paper. However, the observed discrepancies between the intensities of individual bands in the L-dwarf spectra are of interest for further study. At any rate, this suggests that a more refined approach to analyzing L-dwarf spectra should include non-equilibrium models, with allowance for departures from LTE for both atoms and molecules.

5.4. Additional Opacity

Gas–dust phase transitions reduce the concentrations of TiO and VO molecules, whose absorption bands are an important opacity source in M-dwarf atmospheres. On the other hand, the formation of the dust component in L-dwarf atmospheres changes the temperature structure of these stars and, as we showed in our earlier paper [19], appreciably affects their spectral energy distributions. Broadly speaking, we should point out a number of typical problems with opacity computations at low temperatures, which arise in the case L dwarfs. Absorption due to H^- ions is very important in this case: all atoms are in their ground states, so that bound–free absorption shows up only in the ultraviolet. Moreover, molecular absorption in the optical part of L-dwarf spectra is substantially weakened due to the binding of many molecules and/or atoms in dust grains. As a result, even a small amount of additional opacity affects the shape of the spectra [19].

Unfortunately, the optical properties of the absorbing dust grains in L-dwarf atmospheres are known only approximately [22]. In general, they should depend on many parameters: the size of the absorbing dust grains, their chemical composition, shape, spatial orientation, etc. Naturally, our model for the additional opacity in L-dwarf atmospheres is rather simplified. Moreover, our computations were based on an isotropic model for the additional opacity, with the parameters a_0 and N independent of height in the atmosphere. However, even this model satisfactorily describes the optical spectral energy distributions of L dwarfs over a wide range of effective temperatures (see also [19]). Note that, in this case, we are dealing with the spectral energy distributions of L dwarfs, and not just with individual line profiles, which, in general, are determined by the ratio F_ν^l/F_ν^c, where F_ν^l and F_ν^c are the line and continuum fluxes, respectively. We showed above that it is virtually impossible to isolate "pure" (i.e., determined relative to the continuum)

absorption line profiles for L dwarfs. Moreover, it is the opacity due to absorption in the lines of the K I and Na I resonance doublets that determines the appearance and shape of L-dwarf spectra over a broad wavelength range.

ACKNOWLEDGMENTS

I am grateful to R. Rebolo and M.R. Zapatero Ozorio (La Laguna, Spain) for providing the observational data and for fruitful collaboration, and to T. Tsuji (Tokyo, Japan) for providing his grid of L-dwarf model atmospheres. I greatly appreciate the comments of the anonymous referee, which contributed to improving the style of the paper. This work was partially supported by a Small Research Grant from the American Astronomical Society.

REFERENCES

1. Ya. V. Pavlenko, Astrophys. Space Sci. **253**, 43 (1997).
2. J. D. Kirkpatrick, T. J. Henry, and D. W. McCarthy, Jr., Astrophys. J., Suppl. Ser. **77**, 417 (1991).
3. F. Allard and P. H. Hauschildt, Astrophys. J. **445**, 433 (1995).
4. R. Rebolo, E. L. Martín, G. Basri, *et al.*, Astrophys. J. Lett. **469**, L53 (1996).
5. G. Basri and E. L. Martín, Astron. J. **118**, 2460 (1999).
6. A. Burrows and J. Liebert, Preprint No. 1088 (Steward Observatory, 1992).
7. R. Rebolo, E. L. Martín, and A. Magazzu, Astrophys. J. Lett. **389**, L83 (1992).
8. I. N. Reid, D. Kirkpatrick, C. A. Beichman, *et al.*, Astron. Astrophys., Suppl. Ser. **192**, 5517 (1998).
9. Ya. V. Pavlenko, Odessa Astron. Publ. **10**, 76 (1997).
10. Ya. V. Pavlenko, Astron. Zh. **75**, 888 (1998) [Astron. Rep. **42**, 787 (1998)].
11. C. G. Tinney, X. Delfosse, T. Forveille, and F. Allard, Astron. Astrophys. **338**, 1066 (1998).
12. J. D. Kirkpatrick, F. Allard, T. Bida, *et al.*, Astrophys. J. **519**, 834 (1999).
13. E. L. Martín, G. Basri, X. Delfosse, and T. Forveille, Astron. Astrophys. **327**, L29 (1997).
14. T. Nakajima, B. R. Oppenheimer, S. R. Kulkarni, *et al.*, Nature **378**, 463 (1995).
15. M. A. Strauss, X. Fan, J. E. Gunn, *et al.*, Astrophys. J. Lett. **522**, L61 (1999).
16. Z. I. Tsvetanov, D. A. Golimowski, Wei Zheng, *et al.*, Astrophys. J. Lett. **531**, L61 (2000); astro-ph/0001062.
17. A. J. Burgasser, J. D. Kirkpatrick, M. E. Brown, *et al.*, Astrophys. J. Lett. **522**, L65 (1999).
18. A. J. Burgasser, J. D. Kirkpatrick, R. M. Cutri, *et al.*, Astrophys. J. Lett. **531**, L57 (2000); astro-ph/0001194.
19. Ya. Pavlenko, M. R. Zapatero Osorio, and R. Rebolo, Astron. Astrophys. **355**, 245 (2000).
20. *Henry Draper Catalogue. Annals of the Harvard College Observatory* (1918-1924), Vols. 91–99.
21. Ya. V. Pavlenko, Astron. Zh. **11**, 847 (1999) [Astron. Rep. **43**, 748 (1999)].
22. T. Tsuji, in *Proceedings of the European Conference "Low Mass Stars and Brown Dwarfs is Stellar Clusters and Associations," Los-Cancajos, 1998* (in press).
23. É. A. Gurtovenko and R. I. Kostyk, *The Fraunhofer Spectrum and System of Solar Oscillator Strengths* [in Russian] (Naukova Dumka, Kiev, 1989).
24. L. V. Gurvits, I. V. Veĭts, and V. A. Medvedev, *Thermodynamic Properties of Individual Substances* [in Russian] (Nauka, Moscow, 1982).
25. T. Tsuji, K. Ohnaka, and W. Aoki, Astron. Astrophys. **305**, L1 (1996).
26. H. R. A. Jones and T. Tsuji, Astrophys. J. Lett. **480**, L39 (1997).
27. A. A. Radtsig and B. M. Smirnov, *Reference Data on Atoms, Molecules, and Ions* (Energoatomizdat, Moscow, 1986; Springer-Verlag, Berlin, 1985).
28. R. L. Kurucz, Astrophys. J., Suppl. Ser. **40**, 1 (1979).
29. Ya. V. Pavlenko and A. V. Shavrina, Kinematika Fiz. Nebesnykh Tel **2**, 63 (1986).
30. A. Unsold, *Physik der Sternatmospheren* (Springer-Verlag, Berlin, 1955).
31. C. W. Allen, *Astrophysical Quantities* (Athlone Press, London, 1973; Mir, Moscow, 1977).
32. K. R. Lang, *Astrophysical Formulae: a Compendium for the Physicist and Astrophysicist* (Springer-Verlag, Berlin, 1974; Mir, Moscow, 1978).
33. Y. V. Pavlenko, R. Rebolo, E. L. Martín, and R. J. García López, Astron. Astrophys. **303**, 807 (1995).
34. H. Holweger and E. A. Muller, Sol. Phys. **39**, 19 (1974).
35. V. Andretta, M. T. Gómez, and G. Severino, Sol. Phys. **131**, 1 (1991).
36. D. E. Blackwell, P. A. Ibbeston, A. D. Pettford, and R. B. Willis, Mon. Not. R. Astron. Soc. **177**, 219 (1976).
37. R. L. Kurucz, I. Furenlid, J. Brault, and L. Testerman, *Solar Flux Atlas from 296 to 1300 nm. National Solar Observatory Atlas* (Harvard Univ., Cambridge, 1984).
38. Y. Takeda, K. Kato, Y. Watanabe, and K. Sakadane, Publ. Astron. Soc. Jpn. **46**, 511 (1976).
39. E. L. Martín, X. Delfosse, G. Basri, *et al.*, Astron. J. **118**, 2466 (1999).

Translated by A. Dambis

Astronomy Reports, Vol. 45, No. 2, 2001, pp. 157–161. Translated from Astronomicheskiĭ Zhurnal, Vol. 78, No. 2, 2001, pp. 187–192.

Acceleration of Charged Particles in Collapsing Magnetic Traps During Solar Flares

S. A. Bogachev and B. V. Somov

Sternberg Astronomical Institute, Universitetskiĭ pr. 13, Moscow, 119899 Russia

Moscow State University, Moscow, 119899 Russia

Received February 15, 2000

Abstract—This paper examines the mechanisms for the acceleration of electrons, protons, and ions during solar flares. The acceleration is assumed to occur in two steps. The particles are first pre-accelerated by the electric field of a high-temperature current sheet undergoing magnetic reconnection. A collapsing magnetic trap in the solar corona provides further acceleration. It is shown that the Fermi mechanism accelerates trapped protons and ions even more efficiently than it does electrons. The particles escaping from the trap have energies reaching several GeV. The energy distribution of the accelerated ions is essentially independent of their mass and degree of ionization.

1. INTRODUCTION

Solar flares are well-known sources of high-energy protons, ions, and electrons. In spite of significant achievements in experimental and theoretical investigations of the relevant phenomena, the mechanisms accelerating these energetic particles remain open to question [1–3]. Observational studies of the Sun have revealed some properties of the acceleration. In particular, some data suggest that the acceleration could occur in two steps; that is, that there are, in fact, two mechanisms operating sequentially. In addition, during some flares, protons, ions, and electrons are accelerated with equal efficiencies. In other words, the acceleration of a particle is independent (or almost independent) of its mass. So far, there has been no explanation for this fact [4, 5].

Coronal current sheets undergoing magnetic reconnection are thought to provide the first step of the acceleration [6, 7], while Fermi acceleration in a collapsing magnetic trap could realize the second step (see Figs. 2 and 3 in [6]). Unfortunately, this model dealt only with electrons. Here, we demonstrate that the acceleration of protons and ions is even more efficient in this model. In addition, the original model assumed that all accelerated electrons go into the chromosphere and generate hard X-rays via deceleration. We demonstrate that about half the accelerated protons and ions that escape from the trap do not leave the chromosphere. The other half leaves the corona and gives rise to a flux of energetic particles escaping into interplanetary space. In this case, the energy distribution of the escaping ions is virtually independent of their mass.

2. ELECTRON ACCELERATION IN A TRAP

Trapped particles move along magnetic field lines, periodically reflecting from magnetic mirrors. When they collide with a magnetic mirror, particles can either escape from the trap or be reflected with an increase $\delta V = 2V_m$ in their velocity, where V_m is the velocity of the mirror. Thus, a series of successive reflections will significantly increase the velocity and energy of the trapped particles. This process is obviously consistent with Fermi acceleration [8]. The increase in the particle velocity upon reflection from a mirror is independent of the mass, and is determined by the mirror's velocity alone. This is of fundamental importance for the acceleration of ions.

We will suppose that Fermi acceleration is the main (possibly sole) mechanism changing the velocity and distribution of particles in a trap. This means that we neglect a number of effects [9, 10]. In particular, we assume that the plasma is collisionless inside the trap. In addition, we neglect turbulent movements associated with the shock front. Since Fermi acceleration only changes the longitudinal component of the momentum, we assume that the transverse component is conserved during the acceleration; that is,

$$p_\perp = p_{\perp 0} = \text{const}. \tag{1}$$

Let the length of the trap be L_0 and the particle momentum be p_0 at the initial time $t = 0$. Further, we shall use the dimensionless parameter

$$l = L/L_0, \tag{2}$$

which is the relative length of the trap at the current time

$$l(t) = 1 - \frac{t}{t_0}, \tag{3}$$

where t_1 is the lifetime of the trap. At the initial time ($t = 0$), $l = 1$, and at the time of collapse ($t = t_1$), $l = 0$.

1063-7729/01/4502-0157$21.00

The characteristic temperature of the plasma flowing out from a high-temperature, turbulent current sheet is about 100 MK [11], which corresponds to a kinetic energy of $\mathscr{E} \sim 10$ keV. At this temperature, the thermal velocities [$V = \sqrt{2kT/m}$] of electrons and protons reach $\sim 5 \times 10^9$ and 10^8 cm/s, respectively. Thus, the initial electron velocity considerably exceeds the mirror velocity, $V_m \sim 10^8$ cm/s. Therefore, the relative increase in the electron velocity during a single collision with the mirror is small ($2V_m/V_e \sim 0.01$), and only multiple reflections ($N \geq 100$) can provide an appreciable increase in the electron energy. For this reason, we can consider the discrete process of electron acceleration in the corona to be effectively continuous and adiabatic. In this case (see, for example, [12]), the longitudinal adiabatic invariant is conserved:

$$p_\parallel(t)L(t) = \text{const}, \tag{4}$$

where $p_\parallel$ is the longitudinal component of the electron momentum and L is the current length of the trap. The longitudinal momentum increases:

$$p_{\parallel e}(t) = \frac{p_{\parallel e0}}{l(t)}. \tag{5}$$

At a plasma temperature of $\sim 10^8$ K, even weak acceleration makes the electron motion relativistic. For this reason, the kinetic energy of the trapped electrons is determined by the formula

$$\mathscr{E}_{\parallel e}(l) = \left(\frac{2m_e\mathscr{E}_{\parallel e0}c^2}{l^2} + m_e^2c^4\right)^{1/2} - m_ec^2. \tag{6}$$

3. ACCELERATION OF PROTONS AND IONS

In contrast to the electrons, which suffer about a hundred reflections over the lifetime of the trap, the thermal velocities of protons and ions are comparable to the mirror velocity. Thus, their acceleration is fundamentally discrete and cannot be described in terms of an adiabatic invariant. For this discrete process, the increase in the velocities of heavy particles obey the law

$$V_{\parallel i}(l) = V_{\parallel i0} + 2V_m\mathcal{N}\left(\frac{V_{\parallel i0}(1-l) + V_ml}{2V_ml}\right). \tag{7}$$

Here and below, $\mathcal{N}(x)$ denotes the integer part of x.

In contrast to electrons, the motion of protons and ions at coronal temperatures remains non-relativistic even in the final stage of acceleration. Consequently, their momentum and energy are:

$$\begin{aligned} p_{\parallel i}(l) &= m_iV_{\parallel i}(l) \\ &= p_{\parallel i0} + 2m_iV_m\mathcal{N}\left(\frac{p_{\parallel i0}(1-l) + m_iV_ml}{2m_iV_ml}\right), \end{aligned} \tag{8}$$

$$\begin{aligned} \mathscr{E}_{\parallel i}(l) &= \frac{m_i}{2}V_{\parallel i}(l)^2 \\ &= \frac{m_i}{2}\left[\sqrt{\frac{2\mathscr{E}_{\parallel i0}}{m_i}} + 2V_m\mathcal{N}\left(\frac{(1-l)\sqrt{2\mathscr{E}_{\parallel i0}/m_i} + V_ml}{2V_ml}\right)\right]^2. \end{aligned} \tag{9}$$

Note that, in the general case, the velocity of interaction between a particle and mirror is the sum of their relative motions. We can neglect this when deriving the equations for electron acceleration and assume that the velocity of interaction is equal to the particle velocity, since it significantly exceeds the mirror velocity. To apply this model to the motion of protons and ions, we must take into account both velocities.

4. ESCAPE OF PARTICLES FROM THE TRAP

The equations presented above assume unlimited growth in the particle momentum and energy, which does not occur in reality. There is a limiting longitudinal momentum for each particle. Upon reaching it, a particle cannot be stopped by the mirror and escapes into the chromosphere along magnetic field lines.

To determine the moment of escape, we assume that the transverse adiabatic invariant is conserved over the whole trap (including the mirrors)

$$\frac{p_\perp^2}{B} = \text{const}. \tag{10}$$

When a particle penetrates into a region of a stronger field (i.e., during a collision with a mirror), the longitudinal momentum decreases until the particle stops. If a particle's velocity becomes high enough during the course of its acceleration, the field in the mirror may be insufficient to stop its motion. In this case, the particle penetrates through the magnetic obstacle and escapes from the coronal trap into the chromosphere. Let us assume the magnetic field inside the trap is constant and equal to B_1. When the trap penetrates through a shock front, the field increases to B_2. We shall describe the jump of the field in the magnetic mirror thus created using the dimensionless parameter

$$R = \sqrt{\frac{B_2}{B_1} - 1}. \tag{11}$$

The maximum R value for an adiabatic shock is $\sqrt{3}$. However, for the corona, we must take into account the rapid cooling of plasma behind the shock. This inevitably gives rise to a growth in the jump in B and an increase in R up to ten, as was shown in [13]. Using Eqs. (10) and (11), we can express the escape condition in the form

$$p_\parallel \geq Rp_\perp. \tag{12}$$

The electrons and ions escaping from the trap move toward the chromosphere along magnetic field lines. The probability of collisions with background particles rapidly increases as the transition layer is approached.

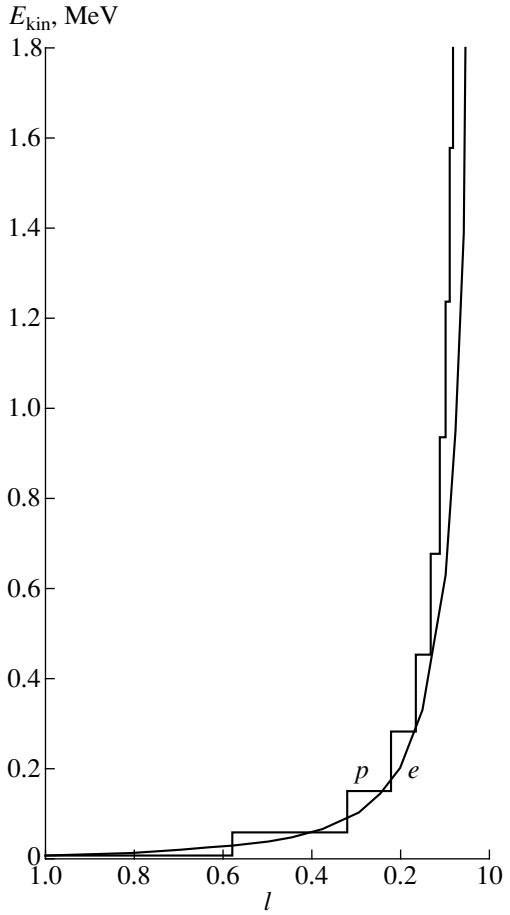

Fig. 1. Increase in the energies of protons (p) and electrons (e) trapped with initial energies 10 keV.

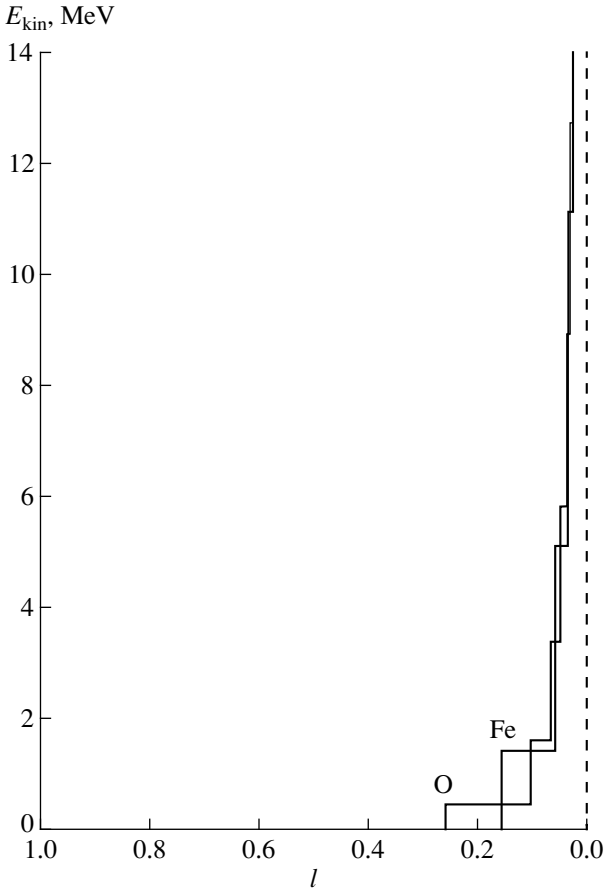

Fig. 2. Acceleration of iron (Fe) and oxygen (O) ions in a collapsing magnetic trap.

Since the longitudinal particle momentum is virtually completely transformed into transverse momentum as a particle moves through the magnetic mirror, the longitudinal velocity of particles reaching the transition layer is relatively low. Due to collisions, these particles can reverse their motion and come back to the corona. Since the upper coronal layers are virtually collisionless, particles reflected from the transition layer freely escape into interplanetary space. The probabilities of reflections toward the corona and chromosphere are the same. Therefore, only half the accelerated particles are absorbed by the chromosphere. The rest escape from the corona along open magnetic field lines. Neglecting the time required for the motion from the mirror to the transition layer, the particles simultaneously escape from the trap and from the corona.

5. THE FLUX OF ENERGETIC PARTICLES

At the moment of escape, the energy of a particle with initial momentum $(p_{\|0}, p_{\perp 0})$ is

$$\mathscr{E}(p_{\perp 0}) = ((R^2+1)p_{\perp 0}^2c^2 + m^2c^4)^{1/2} - mc^2. \quad (13)$$

Since the escape energy depends only on the transverse momentum, it is convenient to use the distribution of this component:

$$f_0(p_{\perp 0}) = 2\int_0^{+\infty} f_0(p_{\|0}, p_{\perp 0})dp_{\|0}. \quad (14)$$

Here, $f_0(p_{\|0}, p_{\perp 0})$ is the initial momentum distribution of the trapped particles.

Initially, there are dN particles in each interval $[p_{\perp 0}, p_{\perp 0} + dp_{\perp 0}]$, determined by the relation

$$\frac{dN}{dp_{\perp 0}} = f_0(p_{\perp 0})p_{\perp 0}. \quad (15)$$

All these particles escape from the trap with the same energy. The energy distribution of the particle flux takes the form

$$\frac{dN}{dE} = \frac{dN}{dp_{\perp 0}}\frac{dp_{\perp 0}}{dE}, \quad (16)$$

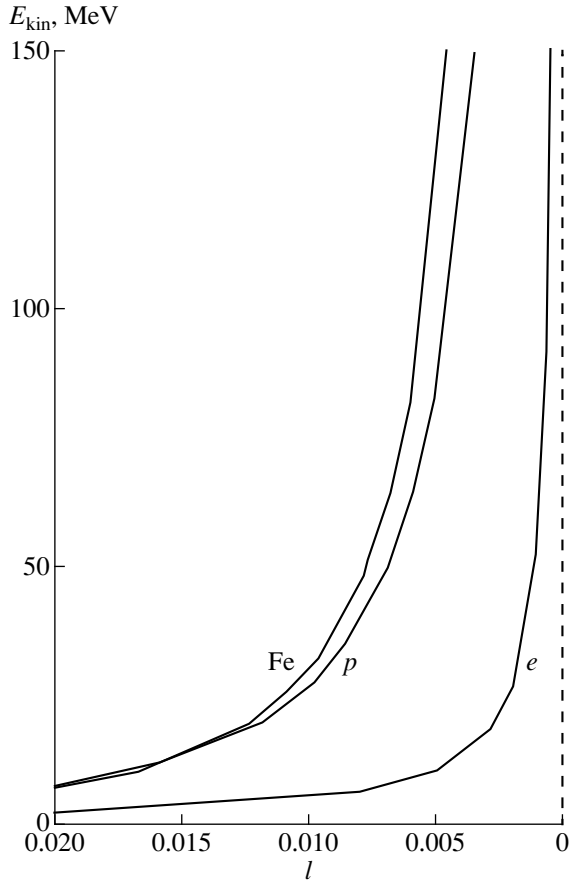

Fig. 3. Acceleration of protons (p), electrons (e), and iron ions (Fe) in a collapsing magnetic trap in the final stage of collapse.

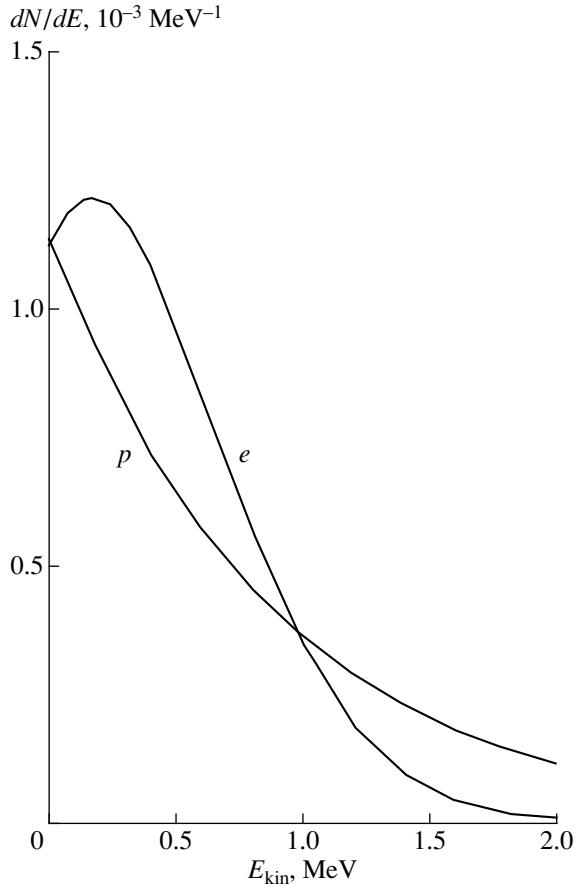

Fig. 4. Energy distribution of escaping protons and ions (p) and electrons (e) below 2 MeV.

where

$$\frac{dp_{\perp 0}}{d\mathscr{E}} = \frac{1}{c\sqrt{R^2+1}}\frac{\mathscr{E}+mc^2}{\sqrt{\mathscr{E}^2+2\mathscr{E}mc^2}}. \quad (17)$$

This expression fully describes the escape of particles that results from the collapse of the trap.

Another possibility for particle escape arises when the length of the trap becomes smaller than the gyroradius of an accelerated particle. In this case, the particle cannot be considered to be trapped; its acceleration ceases and the particle escapes from the trap with the energy it has accumulated up to that moment. Thus, some fraction of the particles cannot reach their maximum energy and escape from the trap before arriving at the critical pitch angle. This increases the number of particles with moderate energies at the expense of decreasing the flux of the most energetic particles.

In a real trap, both escape mechanisms can operate. The balance between them depends on the initial energy distribution of the trapped particles and the characteristics of the trap, in particular, the mirror ratio R.

6. DISCUSSION

The action of Fermi acceleration in a collapsing trap significantly increases the particle energies, with heavier particles acquiring energy faster than lighter ones. The difference between protons and electrons is most prominent (Fig. 1). For instance, when $l = 0.1$, the energy of trapped protons is almost twice that of trapped electrons. For various ions (for example, Fe and O in Fig. 2), there is virtually no difference at this l. As noted above, the thermal velocities of protons and ions at coronal temperatures are comparable to the rate of decrease of the length of the trap. Due to this, the acceleration of heavy particles is discrete, as is shown in Figs. 1 and 2. In the final stages of acceleration ($l \approx$ 0.02–0.00), the ion velocity becomes so high that the discreteness virtually disappears. One appreciable difference between the acceleration of protons and ions arises at this same stage (Fig. 3). Despite the fact that the trap has decreased to 2% of its original length when $l \approx 0.02$, it still contains almost 20% of the particles [14]. Therefore, the difference between the acceleration of protons and ions is important and cannot be neglected.

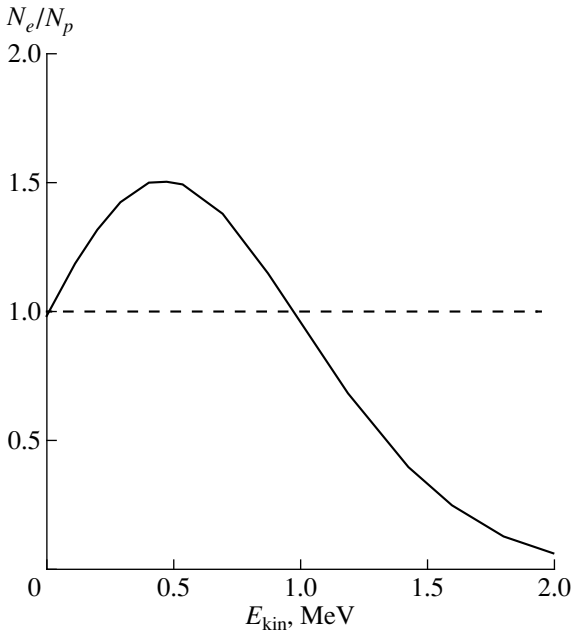

Fig. 5. Ratio of the numbers of escaping electrons and protons for energies below 2 MeV.

The particles escaping from the trap give rise to a high-energy flux into interplanetary space. The considerable difference between the acceleration of protons and electrons is manifest in the fluxes formed by these particles (Fig. 4). If the number of protons is equal to that of electrons in each energy range in the initially trapped plasma, the flux of particles escaping from the trap exhibits an appreciable redistribution in energy. Namely, electrons dominate below 1 MeV, while protons dominate at energies above 1 MeV (Fig. 5).

Finally, we argue that particle acceleration in collapsing magnetic traps during solar flares is efficient for both electrons and heavier particles (protons and ions). Apparently, the collapsing coronal-trap mechanism can explain both the origin of hard X-rays in the corona and the chromosphere and the formation of fluxes of high-energy particles flowing into interplanetary space.

ACKNOWLEDGMENTS

This work was supported by the Russian Foundation for Basic Research (project code 99-02-16344).

REFERENCES

1. H. Hudson and J. Ryan, Ann. Rev. Astron. Astrophys. **33**, 239 (1995).
2. E. L. Chupp, in *High Energy Solar Physics*, Ed. by R. Ramaty, N. Mandzhavidze, and X.-M. Hua (American Inst. of Physics, New York, 1996), p. 3.
3. K.-L. Klein, E. L. Chupp, G. Trottet, *et al.*, Astron. Astrophys. **348**, 271 (1999).
4. G. M. Mason, C. M. S. Cohen, A. C. Cummings, *et al.*, Geophys. Res. Lett. **26** (2), 141 (1999).
5. E. Möbius, private communication.
6. B. V. Somov and T. Kosugi, Astrophys. J. **485**, 859 (1997).
7. T. Kosugi and B. Somov, in *Observational Plasma Astrophysics: Five Years of Yohkoh and Beyond*, Ed. by T. Watanabe, T. Kosugi, and A. C. Sterling (Kluwer, Dordrecht, 1998), p. 297.
8. E. Fermi, Astrophys. J. **119**, 1 (1954).
9. L. Fletcher, in *Proceedings of the 9th European Meeting on Solar Physics "Magnetic Fields and Solar Processes," 1999*, ESA SP-448 (in press).
10. B. V. Somov, Yu. E. Litvinenko, T. Kosugi, *et al.*, in *Proceedings of the 9th European Meeting on Solar Physics "Magnetic Fields and Solar Processes," 1999*, ESA SP-448 (in press).
11. B. V. Somov, *Physical Processes in Solar Flares* (Kluwer, Dordrecht, 1992).
12. B. V. Somov, *Fundamentals of Cosmic Electrodynamics* (Kluwer, Dordrecht, 1994).
13. S. A. Bogachev and B. V. Somov, Vestn. Mosk. Univ., Ser. 3: Fiz., Astron., No. 4, 46 (1999).
14. S. A. Bogachev and B. V. Somov, Izv. Akad. Nauk, Ser. Fiz. **63**, 1555 (1999).

Translated by V. Badin

Astronomy Reports, Vol. 45, No. 2, 2001, pp. 79–85. Translated from Astronomicheskiĭ Zhurnal, Vol. 78, No. 2, 2001, pp. 99–105.

Radio and Optical Spectra of Objects from Two Complete Samples of Radio Sources

V. Chavushyan[1], R. Mujica[1], A. G. Gorshkov[2], V. K. Konnikova[2], M. G. Mingaliev[3], and J. R. Valdéz[1]

[1]*National Institute of Astrophysics, Optics, and Electronics, Puebla, México*
[2]*Sternberg Astronomical Institute, Universitetskiĭ pr. 13, Moscow, 119899 Russia*
[3]*Special Astrophysical Observatory, Russian Academy of Sciences, Nizhniĭ Arkhyz, 357142 Russia*

Received March 10, 2000

Abstract—We present optical identifications and radio spectra for ten radio sources from two flux-density-complete samples. Radio variability characteristics are presented for four objects. The observations were obtained on the RATAN-600 radio telescope at 0.97–21.7 GHz and the 2.1 m telescope of the Haro Observatory in Cananea, Mexico at 4200–9000 Å. Among the ten objects studied, three are quasars, four are BL Lac objects, two are radio galaxies, and one is a Sy 1 galaxy. Two of the sources identified with BL Lac objects, 0509 + 0541 and 0527 + 0331, show rapid variability on time scales of 7–50 days. © *2001 MAIK "Nauka/Interperiodica".*

1. INTRODUCTION

This paper presents the optical identifications and radio spectra of ten sources from two flux-density-limited complete samples of radio sources, together with variability parameters for four of the sources. The first sample includes all Zelenchuk survey sources with fluxes $S > 200$ mJy at 3.9 GHz, covering 24 h in right ascension, at declinations from 4° to 6° (B1950) and with Galactic latitudes $|b| > 10°$ [1]. The second sample was derived from the MGB 4.85 GHz survey, and contains sources with flux densities $S > 100$ mJy at declinations between 74° and 74°44′ (J2000).

One reason to study these samples is to try to detect cosmological evolution in the properties of quasars. Currently, it is only for samples with high limiting fluxes, $S > 1$ Jy [2], for which the redshifts of most objects are available. However, such samples contain few distant quasars (the mean redshift in the samples of [2] is $z = 0.7$), making it impossible to investigate evolutionary effects. Our samples have a sufficiently low flux limit to include a significant number of distant quasars. Half of the quasars identified thus far have redshifts $z > 1.4$. In addition, we observe the complete radio luminosity function of quasars up to $z \approx 1$, making studies of these samples promising for investigations of cosmological relations.

This paper continues our optical identifications for radio sources from the complete samples, initiated in 1998 [3].

2. OPTICAL OBSERVATIONS

We obtained the spectra of the program objects in March–August, 1999 using the 2.1 m telescope of the Guillermo Haro Observatory of the National Institute of Astrophysics, Optics, and Electronics in Cananea, Mexico. The observations used an LFOSC spectrophotometer equipped with a 600×400-pixel CCD [4]. The detector's readout noise was ~8 e^-. The wavelength range of the spectrophotometer was from 4200 to 9000 Å, with an 8.2 Å per pixel reciprocal dispersion. The effective instrumental resolution was about 16 Å.

The data reduction was done in the IRAF package and included flat fielding, wavelength linearization, cosmic-ray removal, and flux calibration. The magnitudes for seven objects were taken from the Automated Plate Scanner Catalog of the Palomar Observatory Sky Survey (POSS) [5].

3. RADIO OBSERVATIONS

The radio observations were obtained on the southern sector of the RATAN-600 radio telescope with a plane reflector at 3.9 and 7.5 GHz in 1980–1991, and on the northern and southern sectors at 0.97, 2.3, 3.9, 7.7, 11.1, and 21.7 GHz in 1996–1999. The detector parameters and antenna-beam patterns for the northern and southern sectors of RATAN-600 are presented in [6–8]. The sources were observed for 15 to 100 days in each run. The source flux densities were determined by averaging the data from each run. The error in the flux density was determined, as usual, from the scatter of the fluxes measured daily in each observing run. The resulting error includes all relevant errors: noise, calibration error, referencing error of the calibration signal, antenna pointing error, etc. The reduction techniques are described in [9]. The flux density scales for different years were reduced to the scale adopted in [8].

4. RADIO AND OPTICAL COORDINATES

Table 1 contains the radio and optical coordinates of the program objects. The source names correspond to hours and minutes of right ascension and degrees and

Table 1. Radio and optical coordinates of the program objects

Object name	Radio coordinates, J2000		Optical coordinates, J2000		Reference
0509 + 0541	$05^h09^m25^s.97$	+05°41′35.″34	$05^h09^m25^s.99$	+05°41′35.″4	JVAS2
0527 + 0331	05 27 32.70	+03 31 31.50	05 27 32.70	+03 31 31.4	JVAS2
0905 + 0537	09 05 07.47	+05 37 16.76	09 05 07.46	+05 37 16.6	NVSS
1027 + 7440	10 27 39.10	+74 40 04.7	10 27 39.20	+74 40 04.4	NVSS
1243 + 7442	12 43 45.03	+74 42 37.13	12 43 44.90	+74 42 38.0	JVAS1
1411 + 7424	14 11 34.74	+74 24 29.1	14 11 34.75	+74 24 29.1	NVSS
1424 + 0434	14 24 09.50	+04 34 52.06	14 24 09.58	+04 34 51.3	JVAS2
1426 + 0426	14 26 28.92	+05 26 58.12	14 26 28.99	+04 26 58.2	NVSS
1511 + 0518	15 11 41.27	+05 18 09.26	15 11 41.28	+05 18 09.1	JVAS2
1923 + 7404	19 23 23.04	+74 04 04.9	19 23 23.48	+74 04 05.1	NVSS

minutes of declination for the equinox J2000. The most accurate coordinates for the studied objects can be found in the Jodrell Bank VLA Astrometric Survey catalogs JVAS2 [10] (8.4 GHz, rms coordinate error 0.014″) and JVAS1 [11] (rms coordinate error 0.012″), and in the NRAO VLA Sky Survey [12] (1.4 GHz, average rms coordinate errors about 0.11″ and 0.56″ in right ascension and declination, respectively). The optical coordinates were derived from the Digitized Palomar Sky Survey.

5. RESULTS

Figures 1 and 2 present the radio and optical spectra of the objects. Below, we quote the old name of the source, corresponding to B1950 coordinates, in parentheses.

0509 + 0541 (0506 + 056)

We observed this source with the RATAN-600 telescope in eight runs at 3.9 and 7.5 GHz in 1980–1991. The highest flux density, $S_{(3.9)} = 894 \pm 29$ mJy and $S_{(7.5)} = 895 \pm 65$ mJy, was recorded in October 1984, and the lowest flux densities, in August 1991, were $S_{(3.9)} = 450 \pm 25$ mJy and $S_{(7.5)} = 420 \pm 22$ mJy (rms errors are quoted here). The weighted average flux densities, $\langle S \rangle$, during our observations were 536 and 531 mJy, respectively, at 3.9 and 7.5 GHz. The variability index for 1984–1991, $V = dS/\langle S \rangle$, derived taking into account individual errors as described in [1, 13], was 0.5 at both frequencies.

Starting in 1996, we observed the source at six frequencies. In 1999, we included it in our program to search for flux density variability on short time scales, and it was observed daily for 100 days starting on May 22, 1999. Figure 1 shows the radio spectra of the source for August 1997 and July 1999. The substantial variability at low frequencies (0.97 and 2.3 GHz) is striking. This source has a small extended component, while its compact component makes the main contribution to its radiation. In the August 1997 spectrum, the peak flux density is at about 12 GHz. The source was in a more active state in 1999; its peak flux density shifted toward higher frequencies and the spectrum could be approximated with a logarithmic parabola, $\log S = 2.727 + 0.173 \log \nu - 0.044 \log^2 \nu$, where the flux density is in mJy and the frequency in GHz. During this interval, the source showed variability at 3.9 and 2.3 GHz on time scales less than ten days, as well as cyclic variability with a 52 day quasi-period at the same frequencies (and possibly also at 7.7 GHz). The cyclic variability at the different frequencies is correlated.

The source was not resolved with the VLA B [14]. In [14], it was identified with a star-like object with magnitudes 16^m and 15.5^m on the POSS *O* and *E* prints. In 1992, at our request, the object's spectrum was taken with the 6-m telescope of the Special Astrophysical Observatory [15], and it was tentatively identified as a BL Lac object. The optical spectrum in Fig. 1 obtained on March 15, 1999 with an exposure time of 40 min shows a featureless continuum, supporting this identification.

0527 + 0331 (0524 + 034)

This is a unique source, with the largest amplitude for long-term flux-density variability among all known radio sources. Its flux density at 7.7 GHz increased more than 20-fold from 1988 till 1998. The pattern of its long-term variability is described in [16]; the variability index for 1984–1991 was $V = dS/\langle S \rangle = 1.9$. In addition, appreciable variability on time scales less than ten days was detected in observations from January 3 to February 25, 1998 [17]. During those observations, the

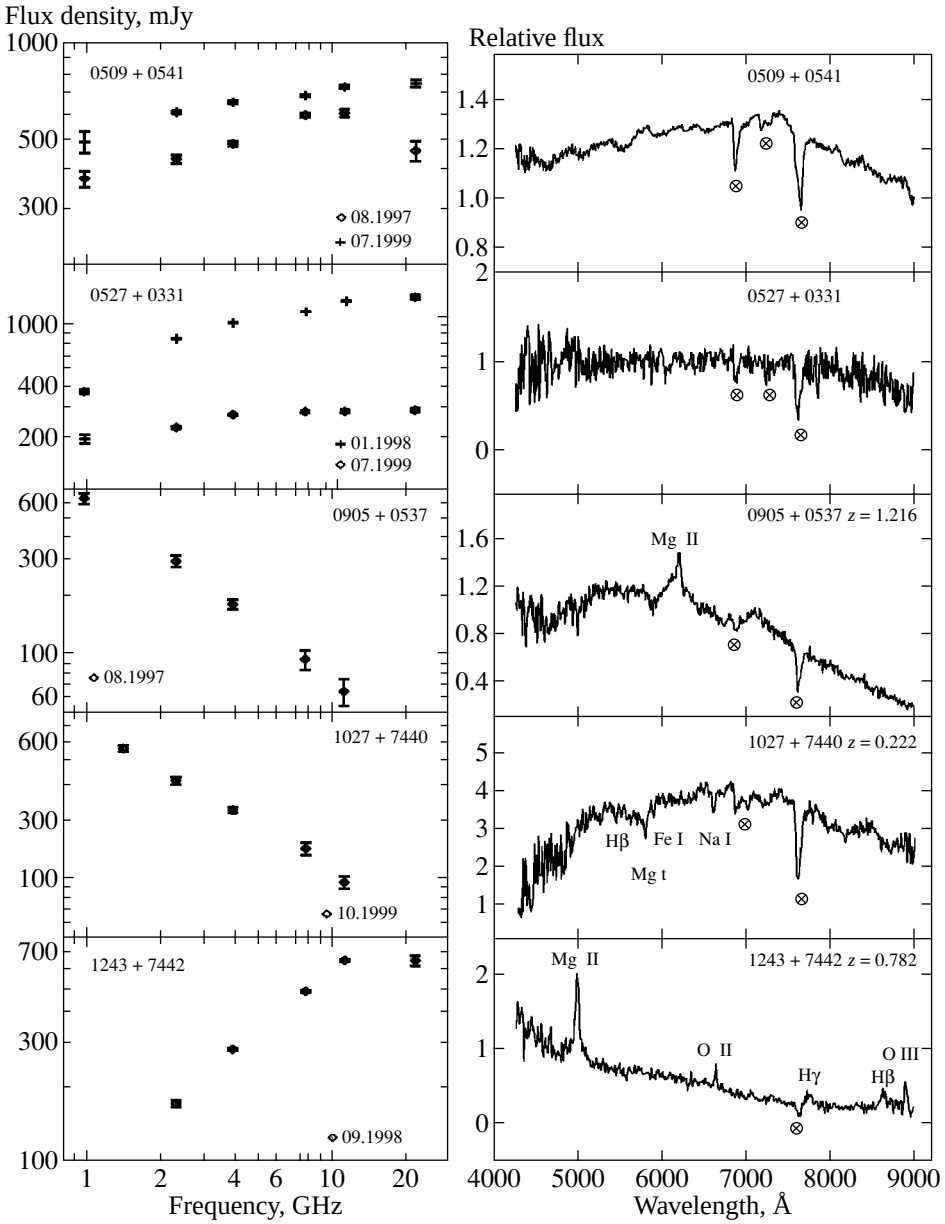

Fig. 1. Radio and optical spectra of 0509 + 0541, 0527 + 0331, 0905 + 0537, 1027 + 7440, and 1243 + 7442.

source's activity state was nearly at maximum; its mean spectrum for that period is shown by the crosses in Fig. 1. The flux density increased towards higher frequencies.

Starting on May 22, 1999, we observed the source daily over 100 days; the mean spectrum for this time interval is indicated by the diamonds in Fig. 1. The source's flux at all frequencies dropped almost fivefold, but the relative amplitude of the rapid variability and the time scales remained unchanged.

The source was identified with a 20^m object on the POSS *O* plate. An optical spectrum taken on October 13, 1999 with a 60-min exposure shows a featureless continuum, suggesting that it is a BL Lac object.

0905 + 0537 (0902 + 058)

This source has a constant flux density, and a power-law spectrum from 0.97 to 11.1 GHz: $S = 627\nu^{-0.920}$ mJy. It was identified with a star-like object with magnitudes 18.1^m and 16.9^m on the POSS *O* and *E* prints. An optical spectrum with a 60-min exposure obtained on March 15, 1999 showed a single strong emission line at 6200 Å, which was interpreted as the Mg II 2798 Å line at a red-

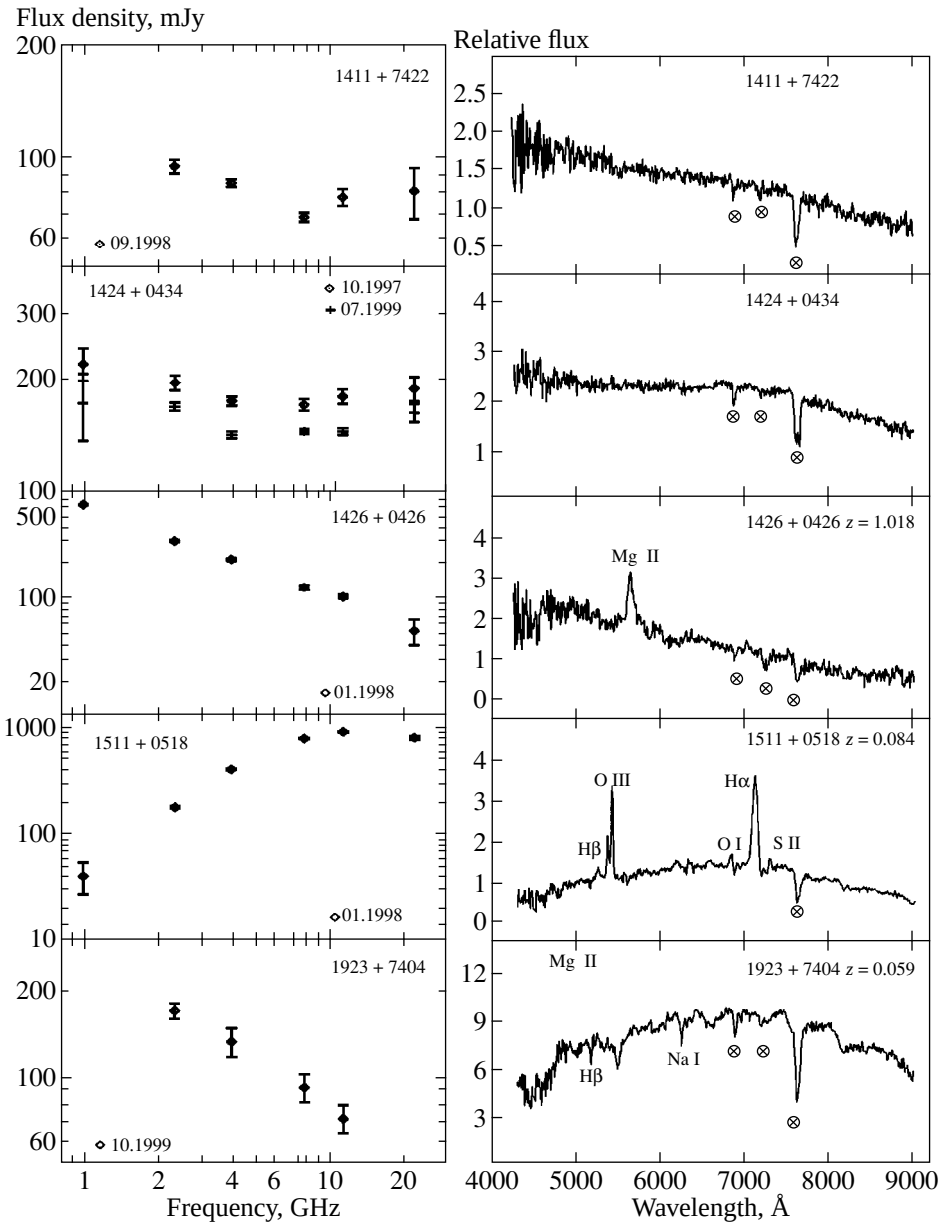

Fig. 2. Radio and optical spectra of 1411 + 7422, 1424 + 0434, 1426 + 0426, 1511 + 0518, and 1923 + 7404.

shift of $z = 1.216$. Thus, the object can be identified as a quasar.

1027 + 7440

This source has a power-law spectrum from 0.97 to 11.1 GHz, $S = 597\nu^{-0.728}$ mJy. The corresponding optical object has magnitudes 17.8^m and 14.1^m on the POSS *O* and *E* prints. An optical spectrum taken on June 3, 1999 with an exposure time of 35 min revealed four absorption lines corresponding to Hβ 4861 Å, Mg I 5175 Å, Fe I 5270 Å, and Na I 5986 Å at a redshift of $z = 0.122$. This spectrum suggests this source should be classified as a radio galaxy.

1243 + 7442

The radio spectrum of this source was observed in September, 1998. It can be approximated by a logarithmic parabola at 2–21 GHz, $\log S = 1.649 + 1.729\ \log\nu - 0.608\log^2\nu$. The peak flux density is at about 15 GHz.

The radio source was identified with a star-like object with magnitudes 19.3^m and 18.6^m on the POSS *O* and *E* prints. An optical spectrum taken on June 4, 1999 with a 60-min exposure shows emission lines at 4986, 6641, 7734, 8662, and 8923 Å, which correspond to the Mg II 2798 Å, [O II] 3727 Å, Hγ 4340 Å, Hβ 4861 Å, and [O III] 5007 Å lines at a redshift of $z = 0.782$. We therefore classify the object as a quasar.

1411 + 7421

Our radio spectrum obtained in September 1998 has a flux-density minimum at about 4 GHz, and can be approximated with a logarithmic parabola from 2.3 to 21.7 GHz, $\log S = 2.188 - 0.651\log\nu + 0.321\log^2\nu$. Two components are present in the spectrum: an extended one with a power-law spectrum and a compact one with a spectrum that grows toward higher frequencies.

The optical spectrum of 1411 + 7421 was taken on June 3, 1999, with an exposure time of 40 minutes. The POSS *O* and *E* magnitudes of the object are 17.2^m and 16.6^m. Since we detected no lines in the spectrum, we classify this source as a BL Lac object.

1424 + 0434 (1421 + 048)

This source has been observed at 3.9 and 7.5 GHz since 1980. During this time, its flux slowly decreased at both frequencies (at 3.9 GHz, from 330 mJy in 1980 to 143 mJy in 1999). The flux variability index for 1984–1991, $V = dS/\langle S\rangle$, is 0.25 at both frequencies.

Since 1996, we have observed the source at six frequencies. Figure 2 presents its spectra for November 1997 and July 1999. Both spectra show a minimum at 5–6 GHz, and the flux decrease occurred without significant changes in the appearance of the spectrum. The July 1999 spectrum corresponds to a logarithmic parabola $\log S = 2.341 - 0.437\log\nu + 0.259\log^2\nu$. Our daily observations covering 100 days starting on May 22, 1999 did not reveal any significant flux density variability on time scales less than several weeks.

The radio source was identified with a star-like object with magnitudes 20.1^m and 18.6^m on the POSS *O* and *E* prints. The object's optical spectrum obtained on June 4, 1999 with an the exposure time of 40 min did not reveal any detectable lines, leading us to classify the source as a BL Lac object.

1426 + 0426 (1423 + 046)

This source has a constant flux density and a power-law spectrum from 0.365 to 21.7 GHz, $S = 610\nu^{-0.767}$ mJy. VLA observations at 4.85 GHz show the radio source to be triple [14], and it is identified with a star-like optical object coinciding with the radio center. The object's magnitudes on the POSS *O* and *E* prints are 19.1^m and 18.1^m. A single emission line is present in a spectrum taken on June 5, 1999 with a 40-min exposure, corresponding to the Mg II 2789 Å line at a redshift of $z = 1.018$. We accordingly classify the object as a quasar.

1511 + 0518 (1509 + 054)

Figure 2 shows a spectrum from 0.97 to 21.7 GHz taken in January 1998. It is well approximated with a logarithmic parabola, $\log S = 1.410 + 2.756\log\nu - 1.222\log^2\nu$, with a peak flux density at about 13 GHz. Unusual features of the spectrum include the absence of an extended component and the large spectral index at frequencies where the spectrum is growing (at 0.97–3.9 GHz, $\alpha = 1.58$, $S \propto \nu^\alpha$). We observed the source at 3.9 and 7.5 GHz in 1984–1990, during which time we detected no statistically significant variability at these frequencies. Our subsequent observations at six frequencies show modest flux variability at frequencies above 7.7 GHz; the variability index for 1.5 years (1997–1998) at 11.1 GHz is $V = 0.1$. A 60-day search for rapid variability in 1998 did not show any appreciable changes of the source's radio flux on time scales less than several weeks.

The corresponding optical object has magnitudes 17.7^m and 15.3^m on the POSS *O* and *E* prints. The optical spectrum in Fig. 2 was taken on August 7, 1999 with a 20-min exposure. The observed system of lines corresponds to Hβ 4861 Å, forbidden nebular [O III] 4959 and 5007 Å, forbidden [O I] 6300 Å, the Hα 6563 Å emission lines at a redshift of $z = 0.084$. In addition, the forbidden [S II] 6717/6731 Å doublet is present, but the spectral resolution was insufficient to separate its components. The width of the hydrogen lines is FWHM ≈ 3000 km/s; while that of the forbidden lines is FWHM ≈ 1000 km/s. We classify the object as a Seyfert galaxy of type SyI at a redshift of $z = 0.084$.

1923 + 7404

This object has a power-law spectrum from 2.3 to 11.1 GHz, with spectral index $\alpha = -0.58$. The flux density at 3.9 GHz is 133 ± 10 mJy.

In the optical spectrum of 1923 + 7404 obtained on June 4, 1999 with an exposure time of 30 min, three absorption lines are apparent: Hβ 4861 Å, Mg I 5175 Å, and Na I 5896 Å, at a redshift of $z = 0.059$. We therefore classify the object as a radio galaxy; it is identified with a 16^m object on the POSS *O* print.

6. CONCLUSIONS

Of the ten objects studied, three proved to be quasars, four BL Lac objects, two radio galaxies, and one a Seyfert galaxy. Two of the BL Lac objects, 0509 + 0541 and 0527 + 0331, show rapid variability on time scales of 7–50 days.

Table 2 summarizes some of the results of our optical and radio observations. Its columns contain (1) the source names, (2) the lines present in the optical spectra, (3) the rest and observed wavelengths of the lines, (4) the redshifts, (5) the object classifications, (6) the POSS *O* magnitudes, (7) the radio flux densities at 3.9 and 11.1 GHz, and (8) the spectral index α between these frequencies.

Table 2. Summary of optical and radio observations

Object name	Spectral Lines	Wavelength, Å	z	Classification from the spectrum	m_O	Flux density at 3.9 and 11.1 GHz in 1998, mJy	α
1	2	3	4	5	6	7	8
0509 + 0541	None			BL Lac	16.0	657 ± 7	0.11
						734 ± 9	
0527 + 0331	None			BL Lac	20.0	886 ± 7	0.31
						1228 ± 15	
0905 + 0537	Mg II	2798/6200	1.216	QSO	18.1	180 ± 10	–0.97
						65 ± 10	
1027 + 7440	Hβ	4861/5454	0.122	Gal	17.8	225 ± 7	–0.81
	Mg I	5175/5806				96 ± 7	
	Fe I	5270/5913					
	Na I	5896/6615					
1243 + 7442	Mg II	2798/4986	0.782	QSO	19.3	284 ± 3	0.80
	[O II]	3727/6641				654 ± 6	
	Hγ	4340/7734					
	Hβ	4861/8662					
	[O III]	5007/8923					
1411 + 7424	None			BL Lac	17.2	85 ± 2	–0.08
						78 ± 4	
1424 + 0434	None			BL Lac	20.1	176 ± 5	0.03
						181 ± 8	
1426 + 0426	Mg II	2798/5646	1.018	QSO	19.1	215 ± 6	–0.70
						103 ± 4	
1511 + 0518	Hβ	4861/5269	0.084	Sy1	17.7	407 ± 5	0.77
	[O III]	4959/5376				906 ± 13	
	[O III]	5007/5428					
	[O I]	6300/6829					
	Hα	6563/7114					
	[S II]	6724/7289					
1923 + 7404	Hβ	4861/5148	0.059	Gal	16.0	133 ± 15	–0.58
	Mg I	5175/5480				72 ± 8	
	Na I	5896/6244					

ACKNOWLEDGMENTS

The authors are very grateful to the administration of the G. Haro Observatory (Mexico) for their support of and attention to this study. This work was supported by the Russian Foundation for Basic Research (project code 98-02-16428), the "Universities of Russia" program (grant 5561), the State Scientific and Technology Program "Astronomy" (project 1.2.5.1), and, in part, CONACYT (grants 28499-E and J32178-E).

REFERENCES

1. A. G. Gorshkov and V. K. Konnikova, Astron. Zh. **72**, 291 (1995) [Astron. Rep. **39**, 257 (1995)].

2. T. Herbig and A. C. S. Readhead, Astrophys. J., Suppl. Ser. **81**, 83 (1992).
3. V. Chavushyan, R. Mujica, A. G. Gorshkov, *et al.*, Pis'ma Astron. Zh. **26**, 1 (2000) [Astron. Lett. **26**, 339 (2000)].
4. F. J. Zickgraf, I. Thiering, J. Krautter, *et al.*, Astron. Astrophys., Suppl. Ser. **123**, 103 (1997).
5. R. L. Pennington, R. M. Humphreys, S. C. Odewahn, *et al.*, Publ. Astron. Soc. Pac. **105**, 521 (1993).
6. V. R. Amirkhanyan, A. G. Gorshkov, and V. K. Konnikova, Astron. Zh. **69**, 225 (1992) [Sov. Astron. **36**, 115 (1992)].
7. A. B. Berlin, A. A. Maksyasheva, N. A. Nizhel'skiĭ, *et al.*, in *Proceedings of the XXVII Radio Astronomy Conference, St. Petersburg, 1997*, Vol. 3, p. 115.
8. A. M. Botashev, A. G. Gorshkov, V. K. Konnikova, and M. G. Mingaliev, Astron. Zh. **76**, 7 (1999) [Astron. Rep. **43**, 631 (1999)].
9. A. G. Gorshkov and O. I. Khromov, Astrofiz. Issled. (Izv. SAO) **14**, 15 (1981).
10. A. R. Patnaik, I. W. A. Browne, P. N. Wilkinson, *et al.*, Mon. Not. R. Astron. Soc. **254**, 655 (1992).
11. I. W. A. Browne, P. N. Wilkinson, A. R. Patnaik, and J. M. Wrobel, Mon. Not. R. Astron. Soc. **293**, 257 (1998).
12. J. J. Condon, W. D. Cotton, E. W. Greisen, *et al.*, Astron. J. **115**, 1693 (1998).
13. G. A. Seielstad, T. J. Pearson, and A. C. S. Readhead, Publ. Astron. Soc. Pac. **95**, 842 (1983).
14. C. R. Lawrence, C. L. Bennett, J. N. Hewitt, *et al.*, Astrophys. J., Suppl. Ser. **61**, 105 (1986).
15. V. R. Amirkhanyan, V. V. Vlasyuk, and O. I. Spiridonova, Astron. Zh. **70**, 923 (1993) [Astron. Rep. **37**, 466 (1993)].
16. A. G. Gorshkov and V. K. Konnikova, Astron. Zh. **74**, 374 (1997) [Astron. Rep. **41**, 325 (1997)].
17. A. G. Gorshkov, V. K. Konnikova, and M. G. Mingaliev, Astron. Zh. **77**, 188 (2000) [Astron. Rep. **44**, 161 (2000)].

Translated by N. Samus'

Astronomy Reports, Vol. 45, No. 2, 2001, pp. 86–94. Translated from Astronomicheskiĭ Zhurnal, Vol. 78, No. 2, 2001, pp. 106–115.

The Structure of the Radio Galaxy 3C388 at Decameter Wavelengths

A. V. Megn[1], S. Ya. Braude[1], S. L. Rashkovskiĭ[1], N. K. Sharykin[1], V. A. Shepelev[1], G. A. Inyutin[1], R. V. Vashchishin[1], A. I. Brazhenko[2], and V. G. Bulatsen[2]

[1]*Radio Astronomy Institute, National Academy of Sciences of Ukraine, Kharkov, 310002 Ukraine*

[2]*Gravimetric Observatory of the Geophysics Institute, National Academy of Sciences of Ukraine, Poltava, Ukraine*

Received December 6, 1999

Abstract—Observations of the structure of the radio galaxy 3C338 at decameter wavelengths obtained using the URAN-1 and URAN-2 radio interferometers are presented. The structure of this object at these wavelengths differs appreciably from images obtained at higher frequencies. The most probable simple models for the radio brightness distributions at 25 and 20 MHz are determined: two extended components with sizes from 40″ to 50″ whose centers are separated by 90″–100″ in position angle about 100°, and a single compact component 9″ × 4″ in size, whose flux density does not exceed 10% of the total flux density of the radio galaxy. © *2001 MAIK "Nauka/Interperiodica".*

1. INTRODUCTION

The structure of the radio galaxy 3C338 has been studied at a wide range of frequencies from 86 to 8085 MHz using radio interferometers and aperture-synthesis systems [1–14]. The first radio interferometric observations on comparatively short baselines D ($D/\lambda < 1000$–2000, where λ is the observing wavelength) at 958 [1, 2] and 1425 MHz [3] suggested that the radio source consisted of a single extended component about 70″ in size.[1] Measurements carried out on longer baselines ($D/\lambda > 3000$) showed the presence of at least one additional compact feature providing a modest fraction of the total radio emission.

Based on 2695 MHz observations on several NRAO interferometers with baselines D/λ from 10800 to 24000, Bash [4, 5] considered two possible two-component "core–halo" models for the radio brightness distribution of 3C338. In one of these, the radio emission came from a 16″ halo, which was responsible for 92% of the total flux, and a core less than 1.″5 in size, which provided the remaining 8% of the emission. The second model, which accounted for roughly 25% of the total emission, consisted of a halo and core with angular sizes 12.6″ and <1.″5 and fluxes $0.16S_0$ and $0.09S_0$, respectively, where S_0 is the total flux of the radio galaxy.

A similar core–halo model for this source was obtained at 408 MHz by Wilkinson [6] using an interferometer with baseline D = 24 km. The size of the halo was estimated to be 15″ × 15″, and the unresolved core had dimensions less than 1.″2 × 1.″2. The flux of the halo exceeded that of the core by a factor of 20.5, and the model accounted for 47% of the total flux of 3C338.

A different model for the radio brightness distribution of this source was obtained using the Cambridge one-mile interferometer at 1407 MHz [7] and the Westerbork array at 1415 MHz [8]. These observations had nearly the same angular resolution of about 24″, and show this radio galaxy to be made up of two extended components with dimensions 25″ × 15″ in right ascension and declination, respectively. The centers of these components are separated by 41″ in a position angle of about 82°.

Interferometric observations of 3C338 with higher angular resolution reveal a more complex structure in the radio brightness distribution, consisting of three or more components. For example, an image of 3C338 with resolution 7″ obtained using the three-element NRAO interferometer at 2695 MHz [9] has a third, more compact component with angular dimensions not exceeding 2″–3″, in addition to the two more extended components referred to above, which account for 85% of the total emission of the radio galaxy. This compact component, which is nearly coincident with the position of the optical galaxy, is located between the extended components, about +20″ in right ascension and +10″ in declination from the center of the western component. The image in [9] contains 98% of the total emission. Similar images of 3C338 were obtained using the VLA at 1465 MHz (angular resolution 4″) [10] and the Westerbork array at 4995 MHz (angular resolution 7″) [11].

The relative intensity of the compact component is very frequency dependent; it contributes 27% of the total flux at 4995 MHz, 15% at 2695 MHz, and about 5.5% at 1465 MHz. In contrast to the extended compo-

[1] Here and below, angular sizes are given at the half-maximum intensity level of Gaussian radio brightness distributions.

1063-7729/01/4502-0086$21.00 © 2001 MAIK "Nauka/Interperiodica"

nents, which have spectral indices $\alpha \approx 1.47$ ($S \sim \nu^{-\alpha}$, where S is the spectral flux and ν is the frequency)—i.e., similar to the integrated spectral index of the radio galaxy—the compact component has a nearly flat spectrum, with $\alpha_c \approx 0.36$ from 1465 MHz [10] to 8085 MHz [9].

1435-MHz VLA observations with resolution $1\farcs6 \times 1\farcs6$ [12] indicated a four-component structure. The two extended components had dimensions 23″ and 13″, and the other two components were compact, with dimensions $0\farcs5 \times 0\farcs4$ and $3'' \times 1\farcs3$ in right ascension and declination. The fluxes of the western and eastern extended components were $0.37S_0$ and $0.45S_0$, while the fluxes of the compact components were $0.03S_0$ and $\sim 0.15\ S_0$ for the larger and smaller of the two, respectively. The distance between the centers of the compact features does not exceed $0\farcs5$ in right ascension and $0\farcs5$ in declination.

Thus, the radio brightness distribution of 3C338 at centimeter wavelengths is quite complex, and it is of interest to obtain observations at very low frequencies—for example, at decameter wavelengths where radio interferometric observations of this object have never been conducted.

2. INSTRUMENTS USED, MEASUREMENT METHODS, AND DATA REDUCTION

The first decameter observations of 3C338 were carried out on the URAN-1 and URAN-2 radio telescopes, with baselines $D = 42.3$ and $D = 152.3$ km oriented nearly east–west [15, 16]. Fringes were formed by multiplying the signals from the north–south antenna of the UTR-2 radio telescope [17] with the signals from the URAN-1 and URAN-2 antennas [15]. Retransmission of the UTR-2 signals to URAN-1 enabled this interferometer to operate in real time; the URAN-2 interferometer operated in a VLBI regime.

The north–south UTR-2 antenna received signals of a single linear polarization, while URAN-1 and URAN-2 received two orthogonal linear polarizations simultaneously. This made it possible to take into account the Faraday rotation of the plane of polarization of the signals as they pass through the Earth's ionosphere, which is very large at decameter wavelengths.

All antennas of the radio interferometers are multirow, horizontal, equidistant antenna grids with electrical beam steering in both angular coordinates so that the observations could be conducted when the source was at a range of hour angles. The spatial frequencies for the radio brightness distribution of 3C338 in the U–V plane produced by the URAN-1 and URAN-2 interferometers are given by the relations

$$U_1 = \frac{42276.7}{\lambda}\cos(T_0 - 2\fdg2), \quad (1)$$

$$V_1 = \frac{26981.5}{\lambda}\sin(T_0 - 2\fdg2) - \frac{1080.5}{\lambda}, \quad (2)$$

for URAN-1 and

$$U_2 = \frac{152292.6}{\lambda}\cos(T_0 + 0\fdg38), \quad (3)$$

$$V_2 = \frac{97194.9}{\lambda}\sin(T_0 + 0\fdg38) + \frac{662.1}{\lambda}, \quad (4)$$

for URAN-2. Here, T_0 is the hour angle relative to the time of culmination in degrees and λ is the wavelength in meters.

We observed 3C338 simultaneously at 25 and 20 MHz during nighttime sessions from January through March in 1996 and 1999. Since it was not possible for us to measure the visibility-function phases, we measured only the modulus of the visibility function γ at various hour angles T_0 in an hour-angle interval $\pm 3\fh5$ about culmination using the method of [18].

When reducing the recorded signals, we determined the mean modulus of the visibility function γ for a single 20-minute interval. The observing sessions were carried out over several days, and the data for each (ith) hour angle for all the days were averaged, and the mean-weighted value $\hat{\gamma}_{\mathrm{obs}_i}$ and its error σ_{γ_i} were calculated.

The most suitable method for analyzing these data is fitting models to the brightness distribution using components with Gaussian brightness distributions. Having specified the parameters for a chosen model, we can then calculate $\gamma_{\mathrm{calc}}(T_0)$ and compare this with the observed dependence $\hat{\gamma}_{\mathrm{obs}}(T_0)$. The quantity $\gamma_{\mathrm{calc}}(T_0)$ is given by the expression

$$\gamma_{\mathrm{calc}}(T_0) = \sqrt{\left(\frac{S_1}{S_0}\gamma_1 + \sum_{i=2}^{n}\frac{S_i}{S_0}\gamma_i\cos(\varphi_i)\right)^2 + \left(\sum_{i=2}^{n}\frac{S_i}{S_0}\gamma_i\sin(\varphi_i)\right)^2}, \quad (5)$$

where

$$\varphi_i = \frac{2\pi D}{\lambda}[\Delta\alpha_i\cos(T_0) + \Delta\delta_i\sin(\delta_0)\sin(T_0)] \quad (6)$$

and

$$\gamma_i = \exp\{-[1.88U(T_0)\Delta\theta_{\alpha_i}]^2\} \times \exp\{-[1.88V(T_0)\Delta\theta_{\delta_i}]^2\}. \quad (7)$$

Here, n is the number of model components; δ_0 is the source's declination; $\Delta\alpha_i = \alpha_i - \alpha_1$; $\Delta\delta_i = \delta_i - \delta_1$; α_i, δ_i, $\Delta\theta_{\alpha_i}$, $\Delta\theta_{\delta_i}$, and S_i are the right ascension, declination, angular size, and flux of the ith model component; $S_0 = \Sigma S_i$; and $U(T_0)$ and $V(T_0)$ are the spatial frequencies of the interferometer, given by (1)–(4).

We varied the model parameters in order to obtain the closest agreement possible between the calculated and observed visibility data. We used a standard χ^2 cri-

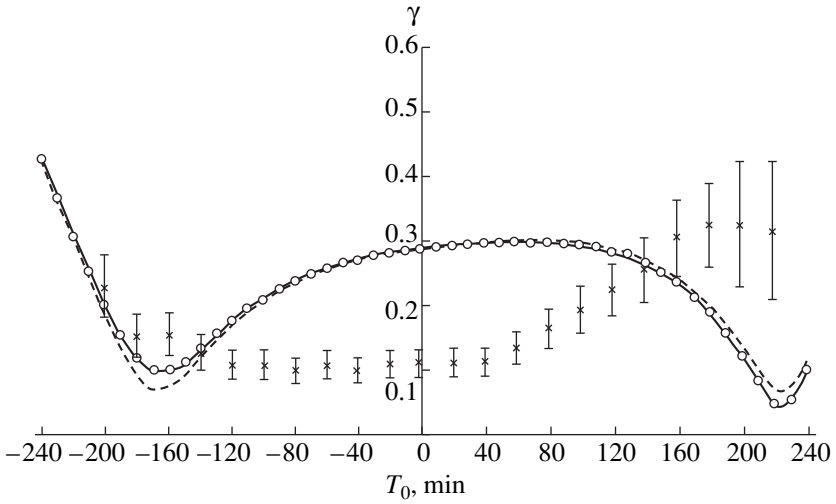

Fig. 1. Visibility function γ for 3C338 at various hour angles T_0 at 25 MHz measured using the URAN-1 interferometer. The crosses show the mean-weighted observational data with their errors $\pm\sigma_\gamma$. The curves and circles show calculated dependences $\gamma_{calc}(T_0)$ for an interferometer with the properties of URAN-1 at 1435 MHz. The solid $\gamma_{calc}(T_0)$ curve is based on a digitized map of the source with resolution 5″.4 obtained using the VLA at 1435 MHz. The dashed $\gamma_{calc}(T_0)$ curve corresponds to the two-component model providing the best agreement with curve (*1*). The circles show the $\gamma_{calc}(T_0)$ curve for the three-component model providing the best agreement with curve (*1*).

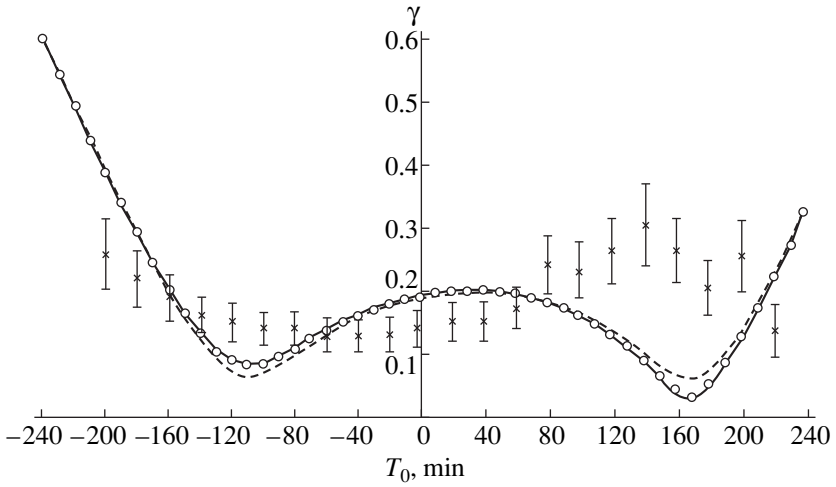

Fig. 2. Same as Fig. 1 for 20 MHz.

terion as a measurement of the closeness of the calculated model data and the observed data [19]:

$$\chi^2 = \sum_{i=1}^{N} \frac{(\hat{\gamma}_{obs_i} - \gamma_{calc_i})^2}{\sigma^2_{\gamma_i}}, \qquad (8)$$

where N is the number of independent measurements of the visibility-function modulus. We used models with various numbers of components. The number of independent parameters in the various models ranged from 2 to 11.

3. RESULTS

The results of our observations on URAN-1 are illustrated in Figs. 1 and 2, which present the rms weighted visibility moduli $\hat{\gamma}_{obs}$ for 3C338 for various hour angles T_0 at 25 MHz (Fig. 1) and 20 MHz (Fig. 2). The vertical lines indicate the rms deviations, taking into account both random and systematic errors relative to the mean-weighted values.

To compare the results obtained at higher frequencies with our own measurements, we include in these figures the dependence $\gamma(T_0)$ calculated for the URAN-1's

resolution at 25 and 20 MHz based on the digitized map of 3C338 obtained in the VLA FIRST survey at 1435 MHz, with resolution 5″.4, assuming that the brightness distribution at 25 and 20 MHz is the same as that at 1435 MHz (solid curves). Essentially, the hour-angle dependences shown by the solid curves would be observed at 1435 MHz on east–west baselines with lengths 737 and 590 m; i.e., with the same angular resolution at 1435 MHz as URAN-1 has at 25 and 20 MHz.

The dependences shown by the solid curves can be approximated well by an idealized model consisting of two extended components. The dependences $\gamma_{calc}(T_0)$ for the two-component model best approximating the digitized map of 3C338 are shown in Figs. 1 and 2 by the dashed curves. The parameters of this model for the radio structure at 1435 MHz are given in Table 1, where $\Delta\alpha$ and $\Delta\delta$ are the separations between the eastern and western components in right ascension and declination in arcseconds, $S_i/\sum S_i$ is the relative flux of a given component, and $\Delta\theta_{\alpha_i}$ and $\Delta\theta_{\delta_i}$ are the angular sizes of a component in α and δ in arcseconds.

Figures 1 and 2 show that, at both frequencies, the calculated dependences $\gamma(T_0)$ for the best two-component model are in good agreement with the solid curves, except at hour angles corresponding to the minimum of γ. It follows that the best two-component model for the resolution of the URAN-1 interferometer describes the radio brightness distribution of 3C338 at long centimeter wavelengths rather well, except near minima of γ, where there is a mutual cancellation of the interferometer signals from the two extended components. This indicates that at least one comparatively weak component must be included in the source model.

The results of calculating $\gamma_{calc}(T_0)$ for the three-component model for 3C338 yielding the best agreement with the solid curves is shown by the circles in Figs. 1 and 2. The calculated dependence $\gamma_{calc}(T_0)$ for this model, whose parameters are given in Table 2, virtually exactly coincides with the solid curves for all T_0 in a $\pm 4^h$ interval about culmination. This three-component model consists of two strong extended components and a relatively weak compact component between them, located near the position of the optical galaxy. This model is in good qualitative agreement with the map of 3C338 presented in [10]. The use of more complex models for data from an interferometer such as URAN-1 is not appropriate since the $\gamma(T_0)$ dependences for various optimal models with more than three components are very similar to each other.[2]

Note, however, as we can see from Figs. 1 and 2, that the dependences $\gamma_{calc}(T_0)$ calculated for the 1435-MHz map and all the associated models are in poor agreement with the decameter-wavelength data (especially at 25 MHz) over a wide range of hour angles. This unambiguously demonstrates that 3C338 has an appreciably different structure at low frequencies. We therefore set out to derive a model for the radio brightness distribution corresponding to the observed dependence $\gamma_{obs}(T_0)$ obtained for the URAN-1 interferometer that was also consistent with our physical understanding of the frequency dependence of the structure detected in the higher frequency map.

With this goal in mind, we searched for models that could provide a good agreement with our observational data and were able to find such models. Figures 3 and 4 compare the URAN-1 results with calculated dependences $\gamma_{calc}(T_0)$ for the best one-, two-, and three-component models for the structure of 3C338 at 25 MHz (Fig. 3) and 20 MHz (Fig. 4).

For the best one-component model (solid curves), with dimensions $\Delta\theta_\alpha = 46''$ and $\Delta\theta_\delta = 52''$ at 25 MHz and $\Delta\theta_\alpha = 53''$ and $\Delta\theta_\delta = 72''$ at 20 MHz, the values of χ^2 were 25.7 and 21.9, respectively.[3] The probability for exceeding these values of χ^2 is $W_{n=19}(\chi^2 > 25.7) = 0.15$ at 25 MHz and $W_{n=19}(\chi^2 > 21.9) = 0.3$ at 20 MHz. Here, $n = N - 1 - p$ is the number of degrees of freedom for the given model, N is the number of independent mean-weighted measured values of $\hat{\gamma}$ at various hour angles, and p is the number of model parameters. It is clear that the best one-component model for the source brightness distribution is not in good agreement with the results of our measurements.

A considerably better agreement can be obtained using the best two-component model, shown by the dashed curves in Figs. 3 and 4. In this case, there is a rather good agreement between the observed and calculated visibility data at both frequencies. The parameters for the corresponding two-component models are presented in Tables 3 (25 MHz) and 4 (20 MHz). At 25 MHz, $\chi^2 = 3.64$, and the probability of exceeding this value is $W_{n=14}(\chi^2 > 3.64) > 0.995$; at 20 MHz, $\chi^2 = 3.58$, and $W_{n=14}(\chi^2 > 3.58) > 0.995$.[4] At both frequencies, the probability for exceeding the χ^2 values we have obtained is very high, testifying to the adequacy of the two-component models in describing our data.

Based on these results, we can draw certain clear-cut conclusions. First, the models derived for the 25- and 20-MHz data differ somewhat. For example, the separations between the component centers were 92″ in position angle 102°.5 at 25 MHz and 106″.3 in position

[2] The consideration of models with more than three components is useful in the analysis of data for larger values of U_{max} and V_{max}, for example, when determining the dependence $\gamma(D/\lambda)$ for $D/\lambda > 5000$.

[3] For comparison, the values of χ^2 for the dependences shown by the solid lines in Figs. 1 and 2 were 564.3 at 25 MHz and 94.3 at 20 MHz.

[4] In this case, the number of degrees of freedom for $N = 22$ is 14, since the two-component model is determined with $p = 7$ parameters.

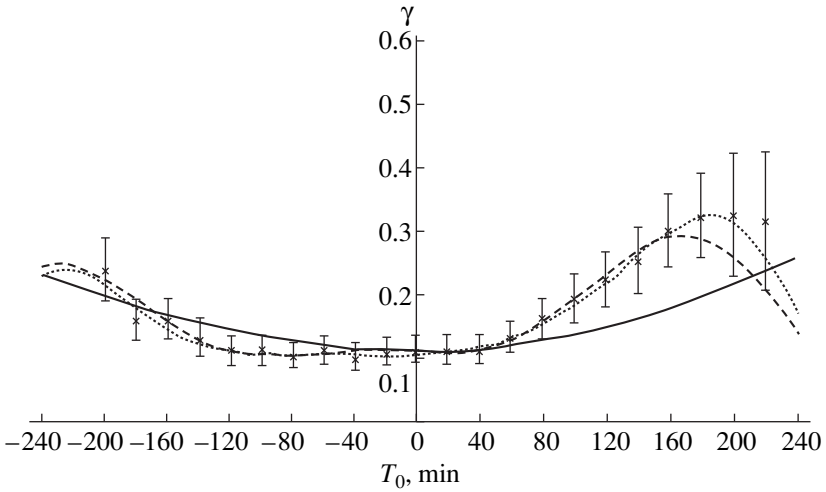

Fig. 3. Visibility function $\gamma(T_0)$ for 3C338 at various hour angles T_0 at 25 MHz measured using the URAN-1 interferometer. Shown are the mean-weighted observational data with their errors $\pm\sigma_\gamma$ (crosses) and calculated dependences of γ on hour angle T_0 for URAN-1 for the one-component (solid curve), two-component (dashed curve), and three-component (dotted curve) models for 3C338 providing the minimum χ^2, i.e., the best agreement with the observational data.

angle 106.°4 at 20 MHz. The angular dimensions of the components were 10″–15″ larger at 20 MHz than the corresponding sizes at 25 MHz. At the same time, the flux ratio for the components is essentially the same at the two frequencies.

Second, comparing the models for the radio brightness distribution of 3C338 at 25 and 20 MHz with the two-component model derived for the map at 1435 MHz (Table 1), we note very appreciable differences. The separation of the component centers more than doubles at the low frequencies (from 45″ to 92″ and 106.″3), and the corresponding position angle changes from 78.°5 to 102.°5 – 106.°3. As a consequence, while the model in Table 1, derived from the 1465 MHz map of 3C338 in [10], determines the regions of maximum radio brightness roughly in the central regions of the extended components at that frequency, the regions of maximum brightness for the decameter-wavelength models are located in the easternmost and westernmost sections of the higher-frequency map. Thus, based on the two-component model brightness distributions we have derived, the radio image of 3C338 at decameter wavelengths differs appreciably from that at long centimeter wavelengths. The radio source is larger at decameter wavelengths, and the maximum radio brightness is observed in regions that are further from the center.

Table 1. Parameters of the best two-component model for 3C338 at 1435 MHz

Feature	$\Delta\alpha_i$	$\Delta\delta_i$	$S_i/\Sigma S_i$	$\Delta\theta_{\alpha_i}$	$\Delta\theta_{\delta_i}$
1 (western)	0″	0″	0.49	26″	13″
2 (eastern)	44	9	0.51	34	20

Table 2. Parameters of the best three-component model for 3C338 at 1435 MHz

Feature	$\Delta\alpha_i$	$\Delta\delta_i$	$S_i/\Sigma S_i$	$\Delta\theta_{\alpha_i}$	$\Delta\theta_{\delta_i}$
1 (western)	–28″	–10″	0.44	20″	15″
2 (central)	0	0	0.13	6.0	6.0
3 (eastern)	22	–1	0.43	30	26

We obtained similar results when we considered the best three-component models for the brightness distribution of 3C338 at 25 and 20 MHz, consisting of two extended components and a single compact component. The calculated dependences $\gamma_{calc}(T_0)$ for these models, whose parameters are given in Table 5, are shown by the dotted curves in Figs. 3 and 4. These curves show that, like those for the two-component models, the calculated dependences $\gamma_{calc}(T_0)$ are in good agreement with the observational data. In this case, at 25 MHz, $\chi^2 = 1.59$, and the probability of exceeding this value is $W_{n=12}$ ($\chi^2 > 1.59$) > 0.995. At 20 MHz, $\chi^2 = 3.67$, and $W_{n=12}$ ($\chi^2 > 3.67$) > 0.989. In Table 5, the coordinates of the extended components are given relative to the first (compact) component, whose size was 6″; all components were taken to be uniform.

These results indicate that the best three-component models at 25 and 20 MHz also differ somewhat. In addition, the difference in the separations of the extended components at the two frequencies is nearly the same as that

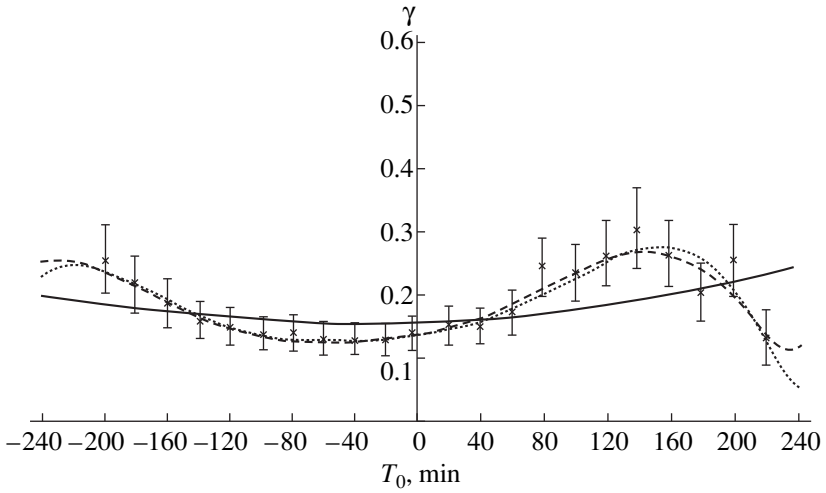

Fig. 4. Same as Fig. 1 for 20 MHz.

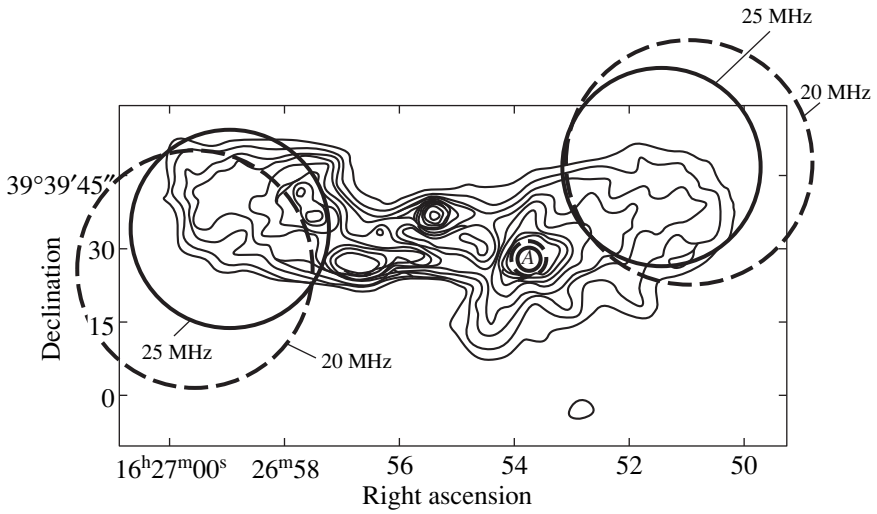

Fig. 5. Most probable three-component model for 3C338 at 25 MHz (solid curves) and 20 MHz (dashed curves) superposed on the 1465-MHz map of the radio galaxy obtained in [10].

for the two-component models.[5] For example, the separations of the centers of the extended components are 89″ in position angle 98° at 25 MHz and 102″ in position angle 102° at 20 MHz. The flux of the compact component is no more than 10% of the total flux of the radio galaxy. This explains why the relative positions and sizes of the extended components in the best two- and three-component models are so similar.

The sizes of the two extended components in the three-component models were nearly the same at the two frequencies, and were both 10″ larger at 20 MHz than at 25 MHz. The separation between their centers at 20 MHz is also larger than at 25 MHz, but lies in the same position angle. The most appreciable difference between the three- and two-component models is the flux ratio for the extended components, which is the same at the two frequencies in the three-component models, with the flux of the eastern component slightly higher than that of the western component.

When comparing these models with higher frequency radio maps of 3C338, such as the 1465 MHz image presented in [10], it is natural to identify the compact low-frequency component with the core or one of the other local emission maxima in this map. Our attempts to superpose the low- and high-frequency results in various ways indicate that the optimum superposition is obtained when

[5] Note that, in the case of the three-component models, we can determine a model for the brightness distribution in which the coordinates of the centers of the components and the distribution of their fluxes are virtually the same at the two frequencies; in this case, the χ^2 at 20 MHz roughly doubles.

Table 3. Parameters of the best two-component model for 3C338 at 25 MHz

Feature	$\Delta\alpha_i$	$\Delta\delta_i$	$S_i/\Sigma S_i$	$\Delta\theta_{\alpha_i}$	$\Delta\theta_{\alpha_i}$
1 (western)	0″	0″	0.27	34″	54″
2 (eastern)	90	–20	0.73	36	56

Table 4. Parameters of the best two-component model for 3C338 at 20 MHz

Feature	$\Delta\alpha_i$	$\Delta\delta_i$	$S_i/\Sigma S_i$	$\Delta\theta_{\alpha_i}$	$\Delta\theta_{\alpha_i}$
1 (western)	0″	0″	0.31	51″	62″
2 (eastern)	102	–30	0.69	45	68

Table 5. Parameters of the best three-component model for 3C338 at 25 and 20 MHz

ν, MHz	$\Delta\alpha_1$	$\Delta\alpha_2$	$\Delta\alpha_3$	$\Delta\delta_1$	$\Delta\delta_2$	$\Delta\delta_3$	$S_1/\Sigma S_i$	$S_2/\Sigma S_i$	$S_3/\Sigma S_i$	$\Delta\theta_1$	$\Delta\theta_2$	$\Delta\theta_3$
25	0″	–27″	61″	0″	19″	6″	0.098	0.42	0.482	6″	40″	40″
20	0	–32	68	0	20	–2	0.097	0.42	0.483	6	50	48

the position of the compact low-frequency component coincides with the local maximum in the western extended component at the higher frequency. To illustrate this, we present in Fig. 5 a superposition of the dimensions and positions of all three 25- and 20-MHz model components on the 1465-MHz map of 3C338 from [10].

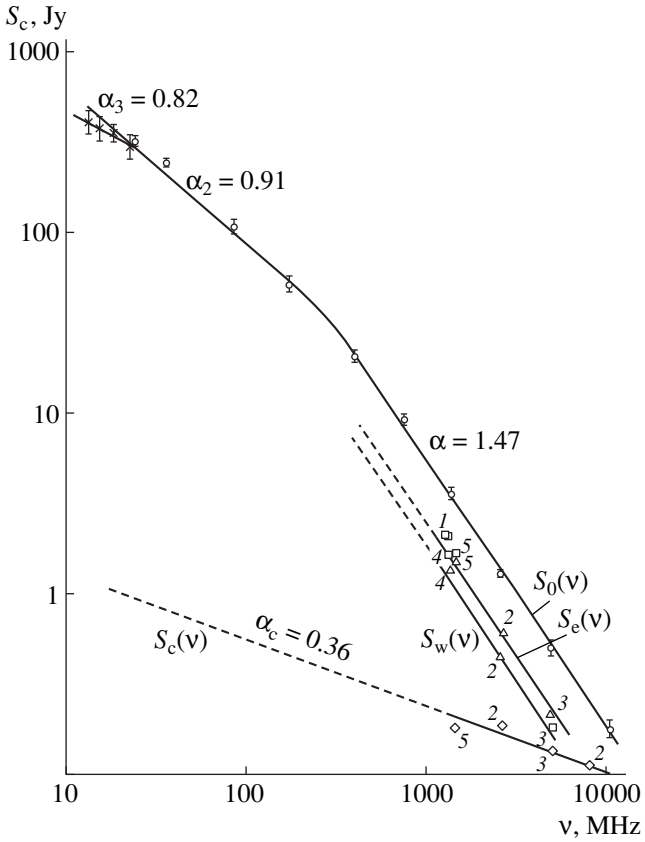

Fig. 6. Dependence of the spectral flux of 3C338 on frequency. $S_0(\nu)$ is the total spectral flux of the radio galaxy, $S_e(\nu)$ the spectral flux of the eastern component (squares), $S_w(\nu)$ the spectral flux of the western component (triangles), and $S_c(\nu)$ the spectral flux of the core (diamonds). The numbers denote references: *1*—[7], *2*—[9], *3*—[11], *4*—[12], and *5*—[10].

The fact that the position of the compact low-frequency component A does not coincide with the core of the radio galaxy is explained by the spectral measurements presented in Fig. 6. This figure shows the frequency dependence of the total intensity of 3C 338 $S_0(\nu)$ from 14.6 to 10000 MHz. The intensities of various features in three-component models for frequencies from 1407 to 8085 MHz are shown by various symbols; plotted are $S_c(\nu)$ for the core (diamonds), $S_w(\nu)$ for the western component (triangles), and $S_e(\nu)$ for the eastern component (squares). The solid curves show these dependences at frequencies at which measurements have been made, and the dashed curves show the spectra expected if power-law relations are maintained at other frequencies. This figure shows that the integrated spectrum of 3C338 has the form $S_0 \sim \nu^{-\alpha}$ from 10000 to 290 MHz, with $\alpha_1 \approx 1.47$. The spectrum $S_0(\nu)$ is also a power law from 290 to 30 MHz, but with $\alpha_2 \approx 0.91$; at frequencies below 30 MHz, the spectral index becomes $\alpha_3 \approx 0.82$. The breaks in the integrated spectrum $S_0(\nu)$ near 290 and 30 MHz suggest variations in the structure of the radio galaxy with frequency. This may be associated with a decrease in the intensity of compact features (local emission maxima) due to absorption in the ionized medium surrounding the radio source, or with other physical processes.

The spectra of all the components of the radio source are also power-law. The spectral indices of the extended components are close to $\alpha_1 = 1.47$, while that of the core α_c is appreciably flatter ($\alpha_c \approx 0.36$). As a result, although the emission of the core exceeds that of the extended components at 8085 MHz, it has a substantially lower intensity than these components at decameter wavelengths, reaching 1 Jy at 20 MHz. Of course, since the sensitivity of the URAN-1 interferometer is about 20 Jy, the radio emission of the core of 3C338 could not be detected by this instrument.

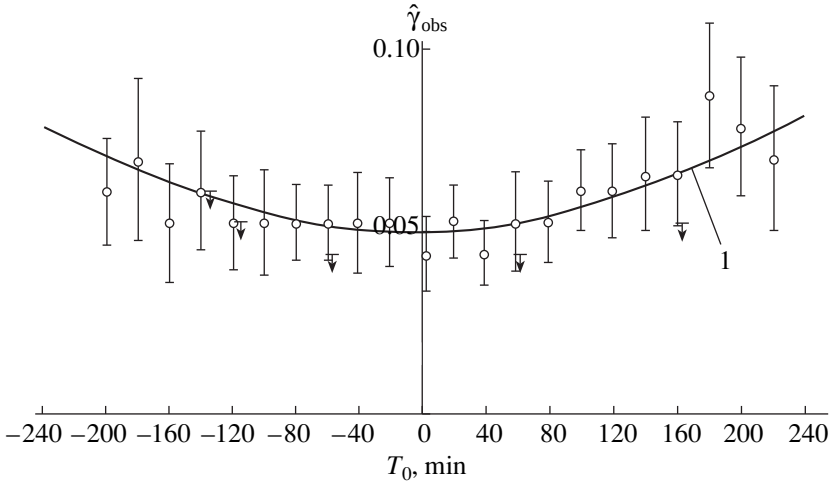

Fig. 7. Visibility function γ for the compact component of 3C338 at various hour angles T_0 at 20 and 25 MHz measured using the URAN-2 interferometer. The circles show the mean-weighted observational data at 20 MHz with their errors $\pm\sigma_\gamma$. The segments with arrows show upper limits to $\hat{\gamma}_i$ at 25 MHz. The solid line is the calculated dependence $\gamma(T_0)$ for a one-component model with $\Delta\theta_\alpha = 9''$, $\Delta\theta_\delta = 4''$, and $S_{com}/S_0 = 0.099$.

4. CONCLUSIONS

Thus, our observations and analysis of data obtained on the URAN-1 interferometer demonstrate that, from the point of view of a χ^2 criterion, two- and three-component models for the radio brightness distribution of the radio galaxy 3C338 fit the data equally well. The difference between these models is small, since the intensity of the third (compact) component in the three-component model is fairly small. The final decision about which of these two models should be preferred can be made on the basis of observations of 3C338 on longer baselines than those of URAN-1. Such observations were carried out in the winter of 1999 on the URAN-2 interferometer, whose baseline is about a factor of 3.5 longer than that of URAN-1. In these observations, the extended components in the models presented in Tables 3–5 should be completely resolved out, since, even if we consider their minimum angular size of 30″, the modulus of the visibility function γ_{ext} should be less than 6×10^{-6} at 25 MHz and 5×10^{-4} at 20 MHz. The corresponding correlated fluxes $S_{corr} = \gamma_{ext} S_{ext}$ (where S_{ext} is the total flux of the extended component) are less than 0.02 Jy at 25 MHz and 0.2 Jy at 20 MHz, whereas the sensitivity of URAN-2 is 12 Jy at both frequencies. Therefore, we expect to detect with URAN-2 only the correlated signal from compact feature with sizes no more than several arcseconds and fluxes no less than 5% of the total flux of the radio galaxy.

In our observations of 3C338 using the URAN-2 interferometer, we detected correlated signals at 20 MHz. However, they had a low ratio of the useful signal S_s to the noise S_n ($S_s/S_n \approx 1$–2). At 25 MHz, the observations were even less certain, and only in certain individual cases at some hour angles could we detect a correlated signal in the noise. This frequency dependence for the signal level is natural, since our observations of the compact component on the URAN-2 interferometer were carried out essentially at the sensitivity limit of the instrument. At the lower frequency, the flux of the object rose and the resolution of the interferometer simultaneously decreased, so that the modulus of the visibility function increased. For example, if the size of the compact component is the same at 25 and 20 MHz, and its spectral index is $\alpha = 0.82$, there should be a nearly twofold decrease in the signal level at 25 MHz compared to 20 MHz.

Figure 7 presents our mean-weighted values of $\hat{\gamma}_{obs}(T_0)$ obtained on URAN-2 at 20 MHz as circles with bars corresponding to the rms errors, taking into account both random and systematic errors. The horizontal segments with arrows indicate upper limits to $\gamma_{obs}(T_0)$ at 25 MHz. The large rms errors σ_{γ_i} are due to the low signal-to-noise ratio for these observations.

Figure 7 shows that, over a wide range of hour angles ($-120^m \ldots +80^m$), $\hat{\gamma}_{obs}(T_0)$ varies only weakly and lies in the range 0.045 – 0.05, which determines the minimum relative intensity of the compact component S_{com}/S_0. At 25 MHz, this quantity is less than 0.045. Figure 7 also shows the calculated dependence $\gamma_{calc}(T_0)$ for the one-component Gaussian model (solid curve) that is in best agreement with the data according to a χ^2 criterion. The dimensions of this component in right ascension $\Delta\theta_\alpha$ and declination $\Delta\theta_\delta$ were $9'' \times 4''$, and its flux was ≈9.9% of the total flux of the radio galaxy. In this case, $\chi^2 = 3.88$, and the probability of this value being exceeded is $W_{n=18}(\chi^2 > 3.88) > 0.995$. Given the qualitative character of our estimation of the parame-

ters of the compact component as a function of hour angle $\gamma(T_0)$ for the three-component model of 3C338 for the URAN-1 observations (Table 5), the refined parameters for this component derived from the URAN-2 observations (its relative flux S_{com}/S_0 and rms dimensions $\sqrt{\Delta\theta_\alpha \Delta\theta_\delta}$) are in good agreement with our preliminary URAN-1 estimates.

Thus, we have established that the brightness distribution of the radio galaxy at decameter wavelengths is described well by a three-component model. This decameter model differs appreciably from the radio image of 3C338 at long centimeter wavelengths, and this is likely also true at meter wavelengths. The radio source, which consists of two extended strong components and one weaker compact component, is roughly a factor of two larger at decameter wavelengths than at long centimeter wavelengths; the brightest regions at decameter wavelengths are located at the eastern and western edges of the image of the source at long centimeter wavelengths. This may be due to the fact that the decameter emission is generated by "radiatively cooled" relativistic electrons, which are located farther from the core of the radio galaxy.

We did not detect any strong, compact features in 3C338, and these may be absorbed at low frequencies. Therefore, the difference in the structures measured at low and higher frequencies may be associated with absorption at low frequencies, in ionized plasma surrounding the radio source, in the source itself, or in the path followed by the radio waves.

ACKNOWLEDGMENTS

This work was supported by INTAS grant 97-1964.

REFERENCES

1. A. T. Moffet, Astrophys. J., Suppl. Ser. **7** (67), 93 (1962).
2. P. Maltby and A. T. Moffet, Astrophys. J., Suppl. Ser. **7** (67), 141 (1962).
3. E. B. Fomalont, Publ. Owens Valley Radio Obs. **1** (3), 1 (1967).
4. F. N. Bash, Astrophys. J. **152** (2), 375 (1968).
5. F. N. Bash, Astrophys. J., Suppl. Ser. **16** (149), 373 (1968).
6. P. N. Wilkinson, Mon. Not. R. Astron. Soc. **160**, 305 (1972).
7. G. H. Macdonald, S. Kenderdine, and Ann. C. Neville, Mon. Not. R. Astron. Soc. **138**, 259 (1968).
8. J. A. Högbom and I. Carlsson, Astron. Astrophys. **34** (3), 341 (1974).
9. L. Rudnick and F. N. Owen, Astron. J. **82** (1), 1 (1977).
10. P. Parma, H. R. de Ruiter, C. Fanti, *et al.*, Astron. Astrophys., Suppl. Ser. **64** (1), 135 (1986).
11. C. Fanti, R. Fanti, I. M. Gioia, *et al.*, Astron. Astrophys., Suppl. Ser. **29** (3), 279 (1977).
12. C. Fanti, R. Fanti, H. R. de Ruiter, *et al.*, Astron. Astrophys., Suppl. Ser. **65** (1), 145 (1986).
13. Yu. V. Volodin, A. G. Gubanov, and R. D. Dagkesamanskiĭ, Preprint No. 184 (Institute of Physics, Academy of Science of USSR, Moscow, 1985), p. 44.
14. L. R. Allen, B. Anderson, R. G. Conway, *et al.*, Mon. Not. R. Astron. Soc. **124** (6), 477 (1962).
15. A. V. Men', S. Ya. Braude, S. L. Rashkovskiĭ, *et al.*, Radiofiz. Radioastron. **2** (4), 385 (1997).
16. A. V. Megn, S. Ya. Braude, S. L. Rashkovsky, *et al.*, Turk. J. Phys. **18** (9), 813 (1994).
17. A. V. Men', L. G. Sodin, N. K. Sharykin, *et al.*, in *Antennas*, Ed. by A. A. Pistol'kors (Svyaz', Moscow, 1978), No. 26, pp. 15.
18. V. P. Bovkun and A. V. Men', Izv. Vyssh. Uchebn. Zaved., Radiofiz. **26** (11), 1357 (1983).
19. D. Himmelblau, *Process Analysis by Statistical Methods* (McGraw-Hill, New York, 1970; Mir, Moscow, 1973).

Translated by D. Gabuzda

Astronomy Reports, Vol. 45, No. 2, 2001, pp. 95–99. Translated from Astronomicheskiĭ Zhurnal, Vol. 78, No. 2, 2001, pp. 116–121.

The Fast Dynamo in Interstellar Turbulence

V. G. Lamburt and D. D. Sokoloff

Moscow State University, Moscow, 119899 Russia

Received March 30, 2000

Abstract—The α effect and coefficient of eddy diffusivity are calculated for the magnetic field in a random flow with recovery. Such a flow loses its memory abruptly at random times that form a Poisson flow of events. Interstellar turbulence sustained by supernova outbursts is one physical realization of such a flow. The growth rates and configurations of large-scale galactic magnetic fields for this situation are close to those predicted by simple galactic dynamo models. At the same time, the model of a flow with recovery makes it possible to trace the role of the effective "forgetting" of correlations. The presence of this forgetting distinguishes interstellar turbulence from other types of random flows. *© 2001 MAIK "Nauka/Interperiodica".*

1. INTRODUCTION

In recent years, views of mechanisms for the formation of the large-scale magnetic fields of spiral galaxies have converged appreciably (see, e.g., [1–5]). Initial concepts in the theory of galactic dynamos (see, e.g., [6]) have become more detailed and have demonstrated their stability and ability to describe observational data. At the same time, some fundamental issues in the theory of galactic dynamos raised in the early 1980s (see, e.g., [7]) have not been satisfactorily resolved.

The problem of a fast dynamo in a steady flow is one such issue. Its essence is as follows [7, 8]. The equations for galactic (as well as stellar and, to some extent, planetary) dynamos underlying galactic-dynamo models can be obtained by averaging the microscopic induction equation over the turbulent pulsations of the velocity field. This procedure naturally involves some assumptions about the properties of interstellar turbulence, which are not entirely realistic. The traditional experience of mathematical physics recommends the substantiation of these constructions through the analysis of some problem in which the velocity field is sufficiently simplified such that it admits an exact solution that reproduces the properties of the solutions to the averaged equations. Early in the 1980s, it was recognized that exact dynamo solutions for the induction equation behave differently from solutions of the mean-field equations for the case of galactic dynamos. It is not possible to achieve an efficiency of dynamo generation in these exactly solvable problems as high as that for mean-field dynamo. In the simplest case, the growth rate of the magnetic field is very low, hopelessly insufficient for the generation of the magnetic fields of galaxies within the lifetime of the Universe. This problem thus came to be known as the fast dynamo problem.

There is currently little doubt that the fast growth of galactic magnetic fields is associated with the effective loss of memory due to interstellar turbulence. However, this belief has thus far remained conventional, since it has not been possible to fill the gap between turbulent-dynamo models that predict a fast growth of the magnetic field and models for dynamos in steady flows, where the growth of the magnetic field involves various complications.

We have been able to fill this gap via a comparatively routine extension of the class of turbulent-field models that can yield mean-field dynamo equations. It is important that the model we discuss here (a random field with recovery) is not only motivated by mathematical considerations, but also reproduces the specific properties of the interstellar medium much better than do standard turbulence models.

Here, we present the results of our studies of a dynamo in a random flow with recovery in the context of our current understanding of interstellar turbulence and the fast dynamo problem.

2. THE VELOCITY FIELD AND GOVERNING EQUATIONS

The simplest models for a turbulent medium that admits derivation of the mean-field equations are the short-correlation model, in which the memory time is considered to be infinitely short [9], and the renewal model, in which the random flow loses its memory at some predetermined, equally spaced renewal times [10, 11]. From the standpoint of the general theory of turbulence, these models are highly specialized; nevertheless, they are widely used in the transport theory of turbulent media (see, e.g., [12]). Both models are quite natural in the context of interstellar turbulence sustained by supernova outbursts; it can be assumed that a supernova explosion erases the memories of the velocity-field evolution virtually instantaneously, and the time τ between two successive supernova outbursts is not directly related to the turnover time $\bar{t}$ for an eddy in the turbulent flow. Moreover, $\tau < \bar{t}$ near the galactic equator, so that the short-correlation model can serve as a

1063-7729/01/4502-0095$21.00

reasonable approximation [6]. Both models suggest the possibility of the fast generation of the galactic magnetic field for appropriate values of the parameters describing the turbulence. However, these models have not yet been applied to studies of the relationship between turbulent and laminar generation mechanisms.

Note that the existence of prescribed renewal moments breaks down the uniformity of time, so that there is no correlation function dependent on the time difference in the renewal model. This uniformity can be recovered if the times of memory loss are assumed to be random Poissonian, rather than prescribed, events. Such a model with recovery for the transport of a passive scalar (dust) in the interplanetary medium was considered in [13]. The calculations in [13] to make the transition from a description of the mean-field transport in renewal models to the analogous description in recovery models can be done quite similarly for the transport of a vector (magnetic field). The meaning of those calculations is that, using functional integrals, an exact solution is written for the initial-value problem for the magnetic-field evolution, and this solution is subsequently averaged over an ensemble of velocity-field realizations. The form of this solution admits the use of the assumption of correlation loss at discrete moments in time to split correlations between the magnetic and velocity field, making it possible to obtain a closed equation for the mean magnetic field. We omit these routine calculations and write the resulting transport equation for the mean (large-scale) magnetic field $\mathbf{B}(t, \mathbf{x}) = \langle \mathbf{H}(t, \mathbf{x}) \rangle$:

$$B_n(t, \mathbf{x}) = \int_0^t \iint P_{nm}(\sigma, \mathbf{x}, \mathbf{y}) B_m(t-\sigma, \mathbf{y}) \lambda e^{-\lambda\sigma} d\sigma d^3\mathbf{y} + e^{-\lambda t} \int P_{nm}(t, \mathbf{x}, \mathbf{y}) B_{0m}(\mathbf{y}) d^3\mathbf{y}, \quad (1)$$

where $\langle \ldots \rangle$ denotes averaging over the ensemble of velocity-field realizations, B_0 is the mean magnetic field at the initial time, λ is the parameter of the Poisson process ($\tau = \lambda^{-1}$ being the mean time between recovery times), and P_{nm} is the kernel of the integral transport equation for the mean field in the renewal model. An explicit (although very complex) functional-integral expression for the kernel P_{nm} in terms of the velocity field is given in [10]. In deriving Eq. (1), we assumed that a magnetic field is introduced into the flow at $t = 0$.

Let us compare Eq. (1) with the analogous equations obtained for other exactly solvable models for the velocity field. In a short-correlation approximation, the equation for the mean concentration turns out to be differential [9], while, for a velocity field with renewal, this equation is integral in space [10]. Equation (1) is integral in both space and time. However, analysis shows that the properties of integral equations of type (1) are very similar to those of the traditional equations for the mean magnetic field (see [10, 13] and the next section).

Note that the resulting equation is time dependent, due to the presence of the last term. This time dependence is associated with the transient process described by the term containing $e^{-\lambda t}$. A different formulation of the problem can also be considered, with a magnetic field introduced into a random flow in the remote past and the distribution of the mean magnetic field known for some other fixed time $t = 0$. In this case, time uniformity is recovered in Eq. (1) and we arrive at the equation

$$B_n(t, \mathbf{x}) = \int_0^\infty \iint P_{nm}(\sigma, \mathbf{x}, \mathbf{y}) B_m(t-\sigma, \mathbf{y}) \lambda e^{-\lambda\sigma} d\sigma d^3\mathbf{y}, \quad (2)$$

$$B_n(0, \mathbf{x}) = B_{n0}(\mathbf{x}),$$

which should be used wherever we can abstract ourselves from the details of the transient process. This equation is valid for any real t, while Eq. (1) is valid only for nonnegative values of t.

Let us assume the velocity field to be statistically uniform, so that $P_{nm}(\sigma, \mathbf{x}, \mathbf{y}) = P_{nm}(\sigma, \mathbf{x} - \mathbf{y})$, and the Fourier transform of Eq. (2) is algebraic in the spatial variables:

$$B_n(t, \mathbf{k}) = \int_0^\infty P_{nm}(\sigma, \mathbf{k}) B_m(t-\sigma, \mathbf{k}) \lambda e^{-\lambda\sigma} d\sigma. \quad (3)$$

3. SHORT RECOVERY TIME

The kernel P_{ij} in Eq. (1) can be explicitly calculated if we assume that the mean time between the recoveries is short. For definiteness, we present here the result for a statistically uniform, isotropic flow without reflection symmetry. We assume that $\lambda \gg 1$ and $\lambda t \gg 1$. Then, according to [14],

$$P_{nm}(\sigma, \mathbf{k}) = 1 + i\alpha(\sigma) k_l \epsilon_{nml} - \mathbf{k}^2 \beta(\sigma)\sigma + O(\sigma^{5/2}), \quad (4)$$

where $\beta(\sigma) = (\nu_m + \frac{2}{3}\langle v^2 \rangle \sigma)$, $\alpha(\sigma) = \frac{2}{3}\langle \mathbf{v}\,\mathrm{curl}\,\mathbf{v} \rangle \sigma$, with ν_m being the molecular magnetic diffusivity, which we will neglect. For the sake of brevity, we omit the standard terms related to differential rotation in expansion (4) and below in Eq. (5). Expanding Eq. (3) in the small quantity λ and returning to the coordinate representation yields

$$\frac{\partial \mathbf{B}}{\partial t} = \mathrm{curl}(2\alpha^* \mathbf{B}) + (\nu_m + 2\beta^*)\Delta \mathbf{B}, \quad (5)$$

where α^* and β^* are expressions for the helicity and eddy diffusivity in mixing-length theory. In other words, taking into account recovery doubles the helicity and eddy-dif-

fusivity coefficients ($\alpha = 2\alpha^*$, $\beta = 2\beta^*$). The renormalization of these coefficients is associated with the fact that, given a mean time between recovery times, the interval between *individual* recoveries can be arbitrarily long (for more detail, see [13], where this phenomenon is discussed using passive-scalar transport as an example).

To estimate the role of this renormalization in the generation of a magnetic field in a body with dimensions L, we must calculate the dimensionless quantity $R_\alpha = \alpha L/\beta$. It is obvious that R_α does not change in the presence of this renormalization, so it is unimportant for the α^2 dynamo. The situation for an $\alpha\omega$ dynamo is a little more complicated, since the term responsible for differential rotation must be taken into account in (5). It is clear that this term does not change in any way if we consider recovery, however, its role is determined by competition with eddy diffusion, i.e., by the dimensionless number $R_\omega = \Omega' L^2/\beta$, where Ω' is the angular-velocity gradient. The renormalization of the eddy diffusivity halves R_ω; i.e., the relative role of differential rotation in the generation of the mean magnetic field is decreased. Clearly, this must be borne in mind when constructing models for the generation of magnetic fields in particular galaxies; however, we cannot claim to be able to calculate the helicity and eddy-diffusivity coefficients from first principles as accurately as within a factor of two. Recall that standard estimates for R_α and R_ω in the theory of galactic dynamos (see, e.g., [6]) are based not only on first principles but also on the experience of seeking reasonable estimates for the parameters of galactic dynamos, compatible with the observed patterns of magnetic fields in galaxies.

4. LONG RECOVERY TIME

Note that, in deriving Eq. (5), we expanded Eq. (3) in the small quantity $\tau = \lambda^{-1}$, and only afterward discussed the properties of the resulting differential equation for the mean magnetic field. In other words, we implicitly assumed the magnetic-field growth time to be shorter than τ, so that the growing eigenfunction is not able to form in a single recovery cycle. There is no doubt that this condition is satisfied in practice. However, the fast dynamo problem considers arbitrary, possibly rather large, values of τ. In this section, we will trace how the growth rate of the mean magnetic field varies with increasing τ.

To study this relationship, let us reformulate the fast dynamo problem in terms of $P_{nm}(\sigma, k)$. From the standpoint of traditional mathematical physics, it would be desirable to construct examples of the velocity field in which, for a given k, the operator P_{nm} has a positive eigenvalue γ_0 that does not decrease for $\nu_m \longrightarrow 0$ and $\sigma \longrightarrow \infty$. There is no doubt that the solution to Eq. (1) will grow in this case at rate γ_0, even if $\lambda = 0$. However, in practice, this behavior of operator P_{nm} can easily be achieved only in the bounded interval $0 < \sigma < t^*$. The growth exponent γ_0 for larger σ normally decreases with decreasing ν_m, or even with increasing σ [14]; thus, for $\lambda = 0$ and $t \gg t^*$, the dynamo turns out to be slow, or even to completely cease to operate.[1] As a rule, time t^* is nevertheless fairly long; for instance, it can exceed the turnover time τ^* of a turbulent eddy by a factor containing the logarithm of the magnetic Reynolds number.

To assess the role of λ in the given situation, we can assume that the magnetic field always has the form of an eigenvector of operator P_{ij}, although its eigenvalue is positive and equal to γ_0 only when $\sigma < t^*$, after which it vanishes. In the galactic-dynamo problem, we expect a monotonic growth of the magnetic field; thus, we will assume that eigenvalue γ_0 is real and positive. In this case, Eq. (1) reduces to

$$B(t) = \lambda \int_0^{t^*} e^{(\gamma_0 - \lambda)\sigma} B(t-\sigma)\, d\sigma, \tag{6}$$

where $B(t)$ is taken to mean the projection of the mean magnetic field onto the fundamental eigenvector of operator P_{ij}. For Eq. (6), the dispersion relation determining the growth rate γ of the magnetic field can easily be obtained:

$$1 = \frac{\lambda}{\gamma_0 - \gamma - \lambda}\left(e^{(\gamma_0 - \gamma - \lambda)t^*} - 1\right). \tag{7}$$

This can be rewritten in the from

$$f_{t^*}(\gamma_0 - \gamma) = f_{t^*}(\lambda), \tag{8}$$

where $f_{t^*}(u) = ue^{-ut^*}$. Note that the trivial solution $\gamma_0 - \gamma = \lambda$ cannot be chosen for Eq. (8), since the denominator in the right-hand side of Eq. (7) vanishes in this case. An exception is the case where this root is multiple, which takes place when $\lambda = 1/t^*$. If $\lambda \gg 1/t^*$, the root of Eq. (8) in which we are interested has the form

$$\gamma = \gamma_0 - \lambda e^{-\lambda t^*}. \tag{9}$$

If, however, $\lambda \ll 1/t^*$, the desired solution has the form

$$\gamma = \gamma_0 - \frac{1}{t^*}\ln\frac{1}{\lambda t^*}. \tag{10}$$

Both asymptotics intersect not far from the point $\lambda t^* = 0.7058$.

We can see from Eq. (9) that, if λ is large (i.e., the memory is lost frequently), the magnetic field grows at a rate that nearly coincides with γ_0. As λ is decreased,

[1] We cannot rule out the possibility that the desired behavior of P_{ij} is possible in certain very special steady flows. It was possible to construct and completely analyze an example of this behavior for a flow model in a certain Riemann space [15].

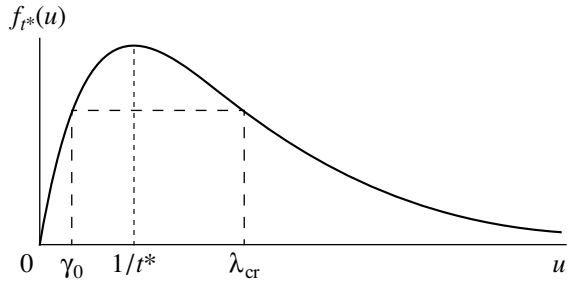

Fig. 1. Determination of the critical value of the Poisson parameter λ.

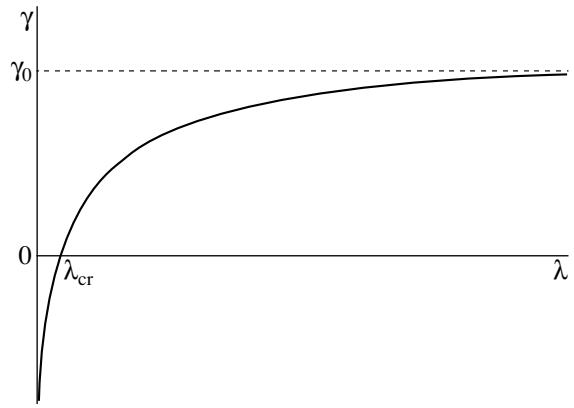

Fig. 2. Dependence of the magnetic-field growth rate γ on the Poisson parameter λ.

the growth rate of the magnetic field decreases and, at some $\lambda = \lambda_{cr}$, vanishes. We can easily verify that λ_{cr} is determined by the relationship

$$f_{t^*}(\gamma_0) = f_{t^*}(\lambda_{cr}). \quad (11)$$

Let us assume that the initial growth rate of the magnetic field is not high; i.e., $\gamma_0 < 1/t^*$ (see Fig. 1). In this case, we find from (11) that

$$\lambda_{cr} = \frac{1}{t^*}\ln\left(\frac{1}{\gamma_0 t^*}\right). \quad (12)$$

If, however, $\gamma_0 > 1/t^*$, the mean recovery time necessary for the growth of the mean magnetic field proves to be even a little longer than the growth time of the magnetic field in a steady flow; i.e., $\lambda_{cr}^{-1} > t^*$. Since time λ_{cr}^{-1} is close to t^*, whereas the latter substantially exceeds the turnover time $\tau^* \approx \lambda^{-1}$ of a turbulent eddy, the criterion $\lambda > \lambda_{cr}$ is quite likely to be satisfied for the interstellar medium.

For $\lambda \longrightarrow 0$, as we can see for the eigenvalue from Eq. (10), $\gamma \longrightarrow -\infty$; the dependence of the growth rate γ on the Poisson parameter λ is shown in Fig. 2.

5. DISCUSSION

Thus, in the framework of exactly solvable transport models for random media, we have traced for the first time the transition from a dynamo in a medium with a finite memory time (in our case, the recovery time) to a dynamo in a steady flow. We have verified that the properties of this transition agree with the natural expectations of astrophysicists. Even relatively rare recoveries associated with supernova explosions in the interstellar medium can ensure the operation of a fast dynamo during the kinematic stage of the development of this instability.

We assumed that the eigenvalue of kernel P_{nm} vanishes when $\sigma > t^*$. In fact, when $\sigma > t^*$, the fast growth of the magnetic field can change into slow growth. For this reason, λ_{cr} provides a lower limit for the Poisson parameter at which a fast dynamo exists. If recoveries occur more rarely than every λ_{cr}^{-1}, the behavior of the magnetic field depends on the detailed behavior of the operator P_{nm} for long times. To elucidate this behavior, we must completely resolve the problem of a fast dynamo in a steady flow.

It is now useful to revisit the question of a fast dynamo in a flow with renewal [10]. In this case, the presence of a fast dynamo depends on the existence of a positive eigenvalue of $P_{nm}(\sigma, k)$ as the magnetic diffusivity approaches zero. Since we have no effective technique to calculate this eigenvalue, and the renewal time appears only in the form of the properties of this operator, we cannot propose a constructive analysis for the behavior of the magnetic field in the limit of long renewal times. In the analysis presented above, it is important that λ appears explicitly in Eq. (1). At the same time, there is no reason to doubt that, in fact, the behavior of the magnetic field in flows with renewal resembles its behavior in flows with recovery.

The above model for memory loss in a flow simulates the properties of an interstellar medium in which turbulent flows are sustained by supernova outbursts. The random-flow model is also applicable to the geodynamo [16], since we can hypothesize that memory could be lost from time to time in the random flows of the conducting fluid of the outer core due to the tearing off of fragments of mantle material (so-called superplumes) and their descent into the core.

Our analysis of the dispersion relation (7) assumed that eigenvalue γ_0 was real. If γ_0 is complex, as is sometimes true during the propagation of the dynamo waves responsible for the solar and stellar activity cycles, our analysis relates the real parts of the growth rates γ_0 and γ, while their imaginary parts, which determine the lengths of the activity cycles, coincide. Note, however, that memory loss in flows in the convective envelopes of the Sun and stars is unlikely to be abrupt, and our model for memory loss is not applicable to the solar and stellar dynamos. At the same time, the phenomenology of the solar and stellar cycles does not indicate any

catastrophic deviations from normal dynamo mechanisms. It is likely that memory loss in turbulence associated with the decay of vortices in the turbulence cascade also ensures the operation of a fast dynamo, although our mathematical techniques do not enable us to study this question.

Note that memory loss due to interstellar turbulence associated with supernova explosions occurs at different times in different regions of the Galaxy. Such flows can be considered flows with local recovery. In this case, spatial regions in which recovery has not taken place for a very long time due to random circumstances are of special interest. If the lifetime of such a region of stagnation is $\hat{t} \gg t^*$, mechanisms for the generation of a magnetic field could be substantially weaker there, and even the decay of the magnetic field is possible. If such a correlation should actually be revealed by observations, this will imply that abrupt loss of memory is indeed important for the operation of fast dynamos, and the theory of stellar cycles requires some revision.

ACKNOWLEDGMENTS

This work was supported by the Russian Foundation for Basic Research (project code 00-05-64062). We are grateful to V.N. Tutubalin, N. Kleeorin, and I. Rogachevskiĭ for helpful discussions, and to the referee for constructive comments.

REFERENCES

1. R. Beck, A. Brandenburg, D. Moss, *et al.*, Ann. Rev. Astron. Astrophys. **34**, 155 (1996).
2. R. Kulsrud, Ann. Rev. Astron. Astrophys. **37**, 37 (1999).
3. D. Moss, A. Shukurov, and D. Sokoloff, Astron. Astrophys. **343**, 120 (1999).
4. G. B. Field, E. G. Blackman, and H. Chou, Astrophys. J. **513**, 638 (1999).
5. D. Elstner, M. Ostrowski, and R. Schlikeiser, in *Plasma Turbulence and Energetic Particles in Astrophysics*, Ed. by M. Ostrowski and R. Schlikeiser (Krakow, 1999), p. 74.
6. A. A. Ruzmaĭkin, D. D. Sokolov, and A. M. Shukurov, *Magnetic Fields of Galaxies* (Nauka, Moscow, 1988).
7. Ya. B. Zeldovich, A. A. Ruzmaikin, and D. D. Sokoloff, *Magnetic Fields in Astrophysics* (Gordon and Breach, New York, 1983).
8. S. Childress and A. D. Gilbert, *Stretch, Twist and Fold: The Fast Dynamo* (Springer-Verlag, Berlin, 1995).
9. S. A. Molchanov, A. A. Ruzmaĭkin, and D. D. Sokolov, Magn. Gidrodin., No. 4, 67 (1983).
10. P. Dittrich, S. A. Molchanov, D. D. Sokoloff, and A. A. Ruzmaikin, Astron. Nachr. **305** (3), 119 (1984).
11. T. Elperin, N. Kleeorin, I. Rogachevskii, and D. Sokoloff, Phys. Rev. E **61**, 2617 (2000).
12. T. Elperin, N. Kleeorin, and I. Rogachevskii, Phys. Rev. Lett. **76**, 224 (1996).
13. V. G. Lamburt, D. D. Sokolov, and V. N. Tutubalin, Astron. Zh. **77**, 743 (2000) [Astron. Rep. **44**, 659 (2000)].
14. S. A. Molchanov, A. A. Ruzmaĭkin, and D. D. Sokolov, Usp. Fiz. Nauk **145**, 593 (1985) [Sov. Phys. Usp. **28**, 307 (1985)].
15. V. I. Arnol'd, Ya. B. Zel'dovich, A. A. Ruzmaĭkin, and D. D. Sokolov, Zh. Éksp. Teor. Fiz. **81**, 2052 (1981) [Sov. Phys. JETP **54**, 1083 (1981)].
16. V. G. Lamburt, D. D. Sokolov, and V. N. Tutubalin, in *Paleomagnetism and Magnetism of Rocks; Theory, Practice, Experiment* (Ob. Inst. Fiz. Zemli Ross. Akad. Nauk, Moscow, 1999), p. 34.

Translated by A. Getling